Spectroscopic studies of new generation of optical and magneto-optical materials

Eva Jesenská

I would like to thank to Professor Takayuki Ishibashi and Professor Martin Veis for all the tremendous support, help and guidance during my doctoral studies. I would also like to thank to all the members of both laboratories, in Japan as well as in Czech Republic, for the great times together, amazing team work, collaboration and friendship. Last, but not the least, I would like to thank to my family, especially to my mother, sister and fiancé for all the love and support.

Title: Spectroscopic studies of new generation of optical and magneto-optical materials

Author: Eva Jesenská
Department / Institute: Nagaoka University of Technology
Institute of Physics of Charles University

Supervisors of the doctoral thesis:
Dr. Takayuki Ishibashi, Ph.D., Department of Materials Science and Technology, Nagaoka University of Technology
RNDr. Martin Veis, Ph.D., Division of Magneto-optics, Institute of Physics of Charles University

Abstract:

In recent years, novel optical and magneto-optical devices have been proposed. This ranges from integrated photonic devices such as 3D holographic displays to magnetic recording, non-reciprocal photonic devices such as optical isolators and circulators or high-energy X-ray/gamma ray detectors. These devices, however, require suitable materials with tunable optical and magneto-optical properties. Presented thesis aims to systematically study such materials, namely CdZnTe, $Gd_xFe_{(100-x)}$ magnetic garnets ($Y_{3-x}Bi_xFe_5O_{12}$, $Nd_2BiFe_{(5-x)}Ga_xO_{12}$, $Nd_{0.5}Bi_{2.5}Fe_{(5-x)}Ga_xO_{12}$) and $Ce_{(0.95-x)}Hf_xCo_{0.05}O_{(2-\delta)}$. Systematic study is carried out by the combination of experimental methods of spectroscopic ellipsometry, magneto-optical Kerr effect spectroscopy and Faraday effect spectroscopy. Experimental results are confronted to theoretical calculations based on Yeh 4x4 matrix formalism. As a result, full permittivity tensor spectra of presented materials are derived and analyzed in terms of microscopic theory. This allows understanding and optimization of physical properties of studied materials which is important when increasing the application potential and suitability for variety of devices.

Keywords: Spectroscopy, Ellipsometry, Kerr effect, Faraday effect, Permittivity tensor

Contents

Introduction

Recent decades have been characteristic by a massive technology development that completely transformed our society. Technology has become smaller, faster and more effective than ever. However, there is still a room for improvement, which has been demonstrated by multiple novel devices proposed by scientific community. In this category, one can find a huge variety ranging from 3D holographic displays to magnetic recording, integrated non-reciprocal photonic devices such as optical isolators and circulators, high-energy X-ray/gamma ray detectors and many more. This kind of novel technology, however, usually operates in nanoscale which complicates the situation. The reason is that nanoscale materials are not only difficult to prepare but their physical properties may also significantly differ from physical properties of their bulk forms. Therefore, the knowledge from the bulk material research can be used only to some extent. What is more, physical properties of materials in nanoscale are significantly influenced by surrounding materials (for example in a multilayer). This goes hand in hand with the compatibility requirement with the current technology (usually Si compatibility) which is obviously also very important. In addition, the huge variety of proposed highly specialized devices requires materials with tunable optical, magnetic and magneto-optical (MO) properties. This type of tuning is usually performed by doping, composition or/and application of strain. These mechanisms must therefore be also understood and properly researched.

In order to process all of these inputs properly, one has to come up with a parameter which characterizes optical and MO properties of studied materials completely. Moreover, this parameter must fully represent studied materials (together with the dimensions information) in any optical or MO calculation. This includes calculations of optical and MO response of complicated multilayered structures/nanostructures. Possibility to incorporate effect of the material on such a structure is very important since structure represents proposed device. Therefore, the main advantage of such an approach would be possibility to design complicated optical and MO devices in the theoretical level before manufacturing any sample. As one can imagine, this can save a big amount of time, finances and effort. The only parameter which meets all of these requirements is the permittivity tensor. Knowledge of the permittivity tensor spectra allows deep understanding of the optical and MO properties of the material. Furthermore, when combined with Yeh 4x4 matrix formalism, it allows calculations of interaction between electromagnetic radiation and multilayered structure.

For all of these reasons combined, we devoted present work to the full permittivity tensor determination and analysis. This was done for four groups of promising novel materials: CdZnTe, $Gd_xFe_{(100-x)}$, magnetic garnets ($Y_{3-x}Bi_xFe_5O_{12}$, $Nd_2BiFe_{(5-x)}Ga_xO_{12}$, $Nd_{0.5}Bi_{2.5}Fe_{(5-x)}Ga_xO_{12}$) and $Ce_{(0.95-x)}Hf_xCo_{0.05}O_{(2-\delta)}$. Furthermore, in order to tune their physical properties properly, we investigated the effect of the composition change for last three groups of materials.

Thesis is organized as follows:

Chapter 1 focuses on the understanding of the full permittivity tensor and its relation to the optical and MO properties of material. This includes energy absorption mechanisms as well as microscopic theory.

Chapter 2 discusses some basic facts about the polarization state of optical waves and shows how MO parameters measured in experiment are related to the Jones matrix of the sample.

Chapter 3 explains the wave equation in special geometries. Moreover, it explains general Yeh 4x4 matrix formalism for description of the optical and MO interactions in multilayers, necessary for theoretical calculations.

Chapter 4 is devoted to the experimental techniques used for measurements of optical and MO spectra.

Chapter 5 presents techniques used for the samples preparation.

Chapter 6 discusses obtained experimental and theoretical results. Based on the type of studied material, it is structured into four sections: CdZnTe, $Gd_xFe_{(100-x)}$, magnetic garnets and $Ce_{(0.95-x)}Hf_xCo_{0.05}O_{(2-\delta)}$.

Finally, we devoted **Chapter 7** to the main conclusions.

1. PERMITTIVITY

Permittivity is a measure of proportionality that exists between electric displacement D and electric field E when forming an electric field in a medium. In simple terms, permittivity quantifies how an electromagnetic field affects, and is affected by a medium.

$$D = \varepsilon E \tag{1.1}$$

1.1. Complex permittivity function

If the medium is isotropic, the permittivity is a complex number. The reason behind this complexity is that response of the material to the external field depends on the field frequency ω. This means that response is not instantaneous but casual. Therefore we can represent this response as a phase difference. Complex numbers allow specification of phase and also magnitude. Therefore, the permittivity becomes complex function defined by

$$D_0 e^{-i\omega t} = \varepsilon_1(\omega) E_0 e^{-i\omega t}. \tag{1.2}$$

Here E_0 and D_0 stand for amplitude of electric displacement and amplitude of electric field respectively; $\varepsilon_1(\omega)$ is the complex permittivity function defined as

$$\varepsilon_1(\omega) = \varepsilon_{1r}(\omega) - i\varepsilon_{1i}(\omega). \tag{1.3}$$

Here, ε_{1r} refers to the real part that is related to the fraction of the energy dispersed by a medium. Consistently, ε_{1i} refers to the imaginary part that is related to the absorption loss (if it is positive) or gain (if it is negative). To summarize, the complex permittivity function represents optical properties of a material in terms of how material responses to the applied field. However, optical properties of the material can be also represented in terms of how the electromagnetic wave propagates in a material. For this purpose, we use the representation of refractive index n and absorption coefficient k. Refractive index is inversely proportional to the length of wave propagation in the material (length after which the phase of the wave changes by 2π). Similarly, absorption coefficient is inversely proportional to the distance in which the amplitude of the propagating wave decays to 1/e of its original value. These constants are related by the equation

$$\varepsilon_{1r} - i\varepsilon_{1i} = (n - ik)^2. \tag{1.4}$$

The real and imaginary parts of the complex permittivity are not independent quantities, nor are the refractive index and absorption coefficient. These are connected by the Kramers-Kronig relations. These relations results from the requirement that material cannot respond to the applied field prior to its application.

$$n(\omega) = 1 + P\int_{-\infty}^{\infty} \frac{d\omega'}{\pi} \frac{k(\omega')}{\omega' - \omega}, \tag{1.5}$$

$$\varepsilon_{1r}(\omega) = 1 + P\int_{-\infty}^{\infty} \frac{d\omega'}{\pi} \frac{\varepsilon(\omega')\omega'}{\omega'^2 - \omega^2}. \tag{1.6}$$

We can derive complex permittivity and therefore all the optical functions of a material from spectroscopic ellipsometry (SE) measurements and analysis which will be discussed in more detail later in this work.

1.1.1. Energy absorption mechanisms

Types and strengths of optical absorption processes that occur in the material determine its optical properties and therefore its complex permittivity function completely. Material absorbs energy from a light beam by multiple mechanisms. The most important mechanisms are:

a) **Interband absorption:** refers to the case when an electron in a bound state in the material absorbs a single photon from the light beam and jumps to a higher energy level in the material.

b) **Intraband absorption:** refers to the case when an electron absorbs a photon from the light beam and jumps to a different energy state within the same band. This process usually requires photon emission or absorption. The only exception is when initial and final electron states occur at the same values of the crystal momentum.

c) **Free carrier absorption:** is a special case of the intraband absorption for conducting materials, which contain a gas of not bound, free carriers, which exhibit distinctive optical absorption.

1.1.2. Theoretical modeling of the complex permittivity function

As mentioned already, the shape and amplitude of the complex permittivity function of the material depends fully on types and strengths of optical absorption processes. To model these processes theoretically, scientists developed multiple theoretical models (usually referred as oscillators or terms), each of which is a function of light beam photon energy *E* (eV). In this subsection, we discuss theoretical models used to model the complex permittivity function in this work.

a) Lorentz model

This model is based on classical theory, which describes an interaction of an optical wave with harmonically bound classical electron having a finite relaxation time. Classic version of Lorentz model is

$$\varepsilon_{1\_Lorentz} = \frac{AmpBrE_0}{E_0^2 - E^2 - i \cdot EBr}\,. \tag{1.7}$$

Parameters E_0, *Amp*, *Br* denote the center energy, amplitude and the broadening parameter respectively [1, 2]. The shape that this model creates in the complex permittivity spectra can be seen in Figure 1.1.

b) Gaussian model

Gaussian model produces Gaussian line shape in ε_{1i} with Kramers-Kronig consistent line shape for ε_{1r} [2, 3].

$$\varepsilon_{1\_Gaussian} = Amp\left\{\begin{matrix}\left(\Gamma\left(\dfrac{E-E_0}{\sigma}\right)+\Gamma\left(\dfrac{E+E_0}{\sigma}\right)\right)+ \\ i\cdot\left(\exp\left[-\left(\dfrac{E-E_0}{\sigma}\right)^2\right]+\exp\left[-\left(\dfrac{E+E_0}{\sigma}\right)^2\right]\right)\end{matrix}\right\}, \tag{1.8}$$

$$\sigma = \frac{Br}{2\sqrt{\ln(2)}}\,. \tag{1.9}$$

Parameters E_0, *Amp*, *Br* and σ denote the center energy, amplitude, broadening and the conductance respectively. The function Γ is a convergence series that produces a Kramers-Kronig consistent line shape for ε_{1r} [2, 3]. As one can see from Figure 1.1, Gaussian model is very useful due to its ability to rapidly approach zero beyond the FWHM position.

c) Tauc-Lorentz

This model reproduces the complex permittivity function of many amorphous materials particularly well. Tauc-Lorentz model (Figure 1.1) produces shape in ε_{1i} defined by equation

$$\varepsilon_{1i\_Tauc-Lorentz} = \left[\frac{AmpE_0Br(E-E_g)}{(E^2-E_0^2)^2+Br^2E^2} \cdot \frac{1}{E} \right] \qquad E > E_g \tag{1.10}$$

$$\varepsilon_{1i\_Tauc-Lorentz} = 0 \qquad E \le E_g. \tag{1.11}$$

Parameters E_0, Amp, Br, E_g denote the center energy, amplitude, broadening and bandgap energy respectively. Function ε_{1r} is produced using Kramers-Kronig relations [2, 4].

d) Drude model

This model is a special case of Lorentz model where the center energy E_0 equals zero. This model was developed to describe the free carrier effect on the complex permittivity function behavior. The model assumes that the microscopic behavior of free carriers in a solid may be treated with a gas of constantly moving carriers bouncing and re-bouncing off heavier static positive ions.

$$\varepsilon_{1\_Drude} = \frac{-\hbar^2q^2N\mu}{\varepsilon_0(\mu m^* m_eE^2+iq\hbar E)} \tag{1.12}$$

Parameters N, μ, m^* denote the carrier concentration, carrier mobility and carrier effective mass respectively. The physical constants are $\hbar$ (Planck constant/2π), q (electron charge), ε_0 (the vacuum dielectric constant) and m_e (the electron mass) [2, 5]. The shape this model creates in the complex permittivity spectra can be seen in Figure 1.1.

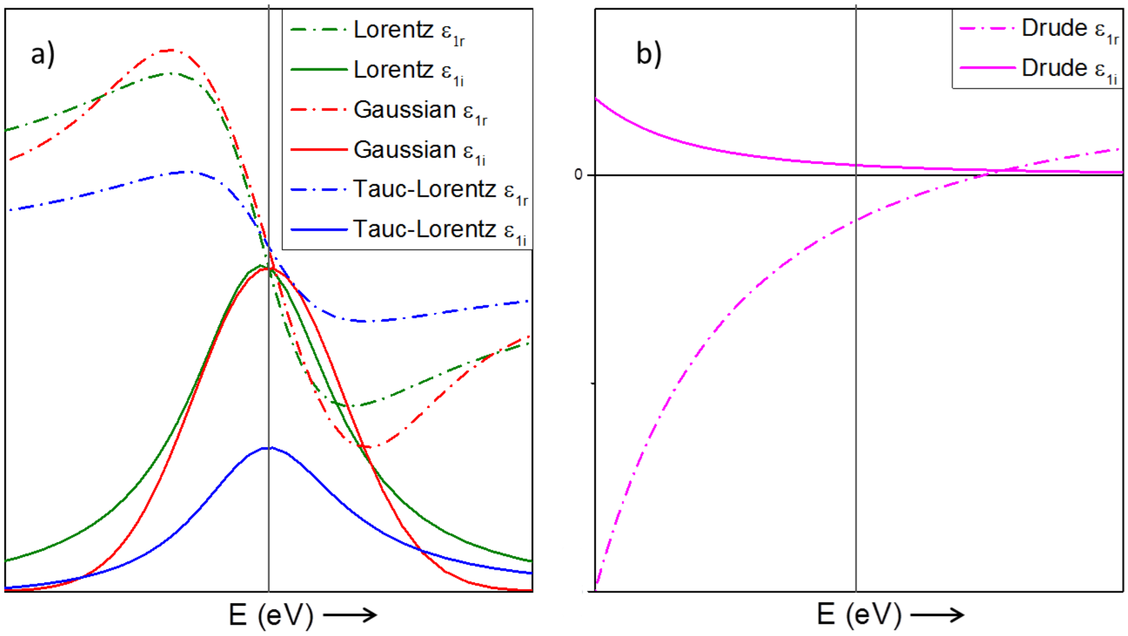

Figure 1.1: The calculated spectra of ε_{1r} and ε_{1i} for a) Lorentz, Gaussian and Tauc-Lorentz oscillators; b) Drude term.

e) Herzinger-Johs model

This model combines highly functional shape with Kramers-Kronig consistent properties and it is useful especially when reproducing complicated complex permittivity function shapes of crystalline materials. The importance of this model is shape of the complex permittivity function it generates; however, its internal parameters have no direct physical meaning. This model consists of four polynomials spline functions f_1, f_2, f_3 and f_4 connected smoothly end-to-end. Functions f_1 and f_3 are equal zero at the endpoints. Variable fit parameters are E_0, *Amp*, *Br*, *WL*, *WR*, *AL* and *AR* that correspond to the center energy, amplitude, broadening, width of left side absorption region, width of right side absorption region, control point for left side and control point for right side respectively. The shape this model creates in ε_{1i} spectra can be seen in Figure 1.2 [2, 6].

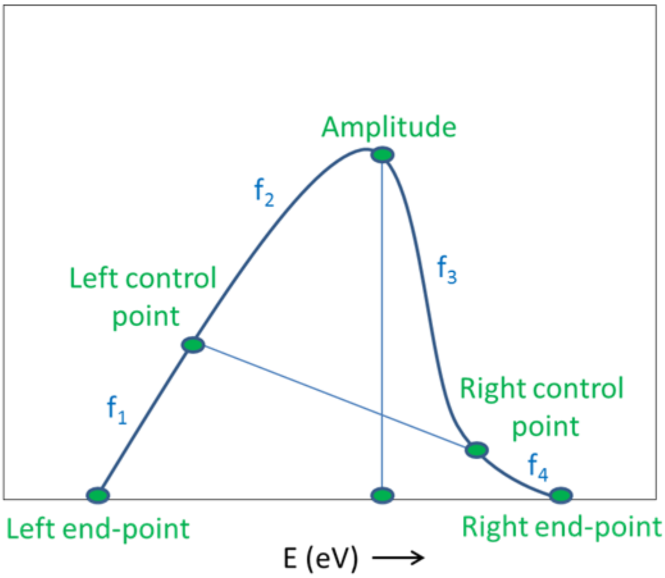

Figure 1.2: The calculated spectra of ε_{1i} for Herzinger-Johs model displaying polynomial spline functions f_1, f_2, f_3 and f_4, as well as end-points and control points.

1.2. Permittivity tensor

When we insert the isotropic material into the magnetic field, the field breaks the symmetry of the system. Therefore we must treat the isotropic material in the magnetic field as anisotropic (all the materials investigated in this work exhibit anisotropy due to a magnetic ordering). Anisotropic system is generally characterized by a different direction of its electric field E and the electric induction D intensity vectors (1.1). Permittivity ε in this system thus has a tensor character and we can express it as

$$\varepsilon = \begin{bmatrix} \varepsilon_{xx} & \varepsilon_{xy} & \varepsilon_{xz} \\ \varepsilon_{yx} & \varepsilon_{yy} & \varepsilon_{yz} \\ \varepsilon_{zx} & \varepsilon_{zy} & \varepsilon_{zz} \end{bmatrix}. \qquad (1.13)$$

Since the field acts as a small perturbation of the isotropic material, we can express the permittivity tensor in the Cartesian representation as follows

$$\varepsilon_{ij} = \varepsilon_{ij}^{0} + K_{ijk} M_k + G_{ijkl} M_k M_l. \qquad (1.14)$$

Here, ε_{ij}^{0} are components of the unperturbed permittivity, M_k are components of the magnetization vector; K_{ijk} and G_{ijkl} are the elements of the linear and quadratic MO tensors responsible for linear and quadratic MO effects. In this work, we restrict ourselves to linear MO effects only. If we have magnetization parallel to the z-axis of the Cartesian coordinate system (the magnetic film-ambient interface is normal to the z-axis, light is propagating along the z-axis) we receive relations

$$\varepsilon_1 = \varepsilon_{xx} = \varepsilon_{yy} = \varepsilon_{zz}, \tag{1.15}$$

$$i\varepsilon_2 = -\varepsilon_{xy} = \varepsilon_{zx} \tag{1.16}$$

Permittivity tensor thus simplifies to the form

$$\begin{pmatrix} \varepsilon_1 & -i\cdot\varepsilon_2 & 0 \\ i\cdot\varepsilon_2 & \varepsilon_1 & 0 \\ 0 & 0 & \varepsilon_1 \end{pmatrix}. \tag{1.17}$$

All elements of the tensor have real and imaginary parts:

$$\varepsilon_1 = \varepsilon_{1r} - i\cdot\varepsilon_{1i}, \tag{1.18}$$

$$\varepsilon_2 = \varepsilon_{2r} - i\cdot\varepsilon_{2i}. \tag{1.19}$$

Off-diagonals ε_2 are proportional to the magnetization in the sample. Therefore, if there is no magnetic field present, permittivity tensor reduces itself to a unit matrix of ε_1.

1.2.1. Microscopic theory

Microscopic theory relates full permittivity tensor spectra to energy level splitting and transition probabilities. As mentioned earlier, when there is a magnetic field applied, off-diagonals of the permittivity tensor ε_2 have finite values. From microscopic point of view, there are three distinct mechanisms producing these finite values:

1) An unequal population of states related to the ***spin polarization of the ground state*** displays the opposite contributions to ε_2.

2) Variations in the energy differences between two states caused by:
   - ***Zeeman splitting*** of the energy levels when the external field acts on the orbital electronic motion
   - ***Spin-orbit splitting***

3) Perturbations caused by ***spin orbit coupling*** effect on wave functions of occupied or unoccupied states or on the kinetic momentum operator.

To summarize, finite values of the ε_2 mean that there are new types of optical transitions in the material, MO transitions, which exist only when the magnetic field is applied. In this work, we will consider two types of these transitions; Dia and Para transitions.

a) Dia transitions: refer to spin and electric-dipole allowed transitions between an orbital singlet ground state and an excited state split by the combined effect of exchange field and spin-orbit coupling [7, 8]. These transitions can be described by an oscillator term, in which ε_2 behaves as:

$$\varepsilon_2 = \frac{\omega_p^2 f \Delta L}{2\omega_0} \frac{(\omega_0 - \omega)^2 - \Gamma_0^2 + 2i\Gamma_0(\omega_0 - \omega)}{\left[(\omega_0 - \omega)^2 + \Gamma_0^2\right]^2} \tag{1.20}$$

Here Δ, ω_0, Γ_0 and f are the separation between the levels caused by spin-orbit coupling, center frequency, half width at half-height of the transition and the oscillator strength respectively. L is the Lorentz-Lorentz local field correction defined as $[(n^2+2)/3]^2$, where n is the refraction index. Dia transition behavior in ε_2 close to the center frequency ω_0 is schematically shown in Figure 1.3(a). One can observe a bell shaped behavior for the real part ε_{2r} and dispersive behavior for the imaginary part ε_{2i}. At center frequency $\omega=\omega_0$, $\varepsilon_{2i}=0$; ε_{2r} has a maximum value

$$(\varepsilon_{2r})_{\max} = \frac{\omega_p^2 f \Delta L}{2\omega_0 \Gamma_0^2} \tag{1.21}$$

and ε_1 shows a resonant behavior with maximum value of ε_{1i}

$$(\varepsilon_{1i})_{\max} = \frac{\omega_p^2 f L}{2\omega_0 \Gamma_0}. \tag{1.22}$$

b) Para transitions

In the case of Para transitions neither the ground state nor the final state are split. However, the oscillator strengths for right circularly polarized light f_+ and left circularly polarized light f_- are different [7, 8]. These transitions can be described by an oscillator term, which in ε_2 behaves as:

$$\varepsilon_2 = \frac{\omega_p^2 f df L}{2} \frac{\omega(\omega_0^2 - \omega^2 - \Gamma_0^2) - i\Gamma_0(\omega_0^2 + \omega^2 + \Gamma_0^2)}{\omega_0\left[(\omega_0^2 + \omega^2 + \Gamma_0^2)^2 + 4\omega^2\Gamma_0^2\right]^2}. \tag{1.23}$$

Here df is the fractional dichroism defined as

$$df = \frac{f_- - f_+}{f_- + f_+}. \tag{1.24}$$

Para transition behavior in ε_2 close to the center frequency ω_0 is schematically shown in Figure 1.3(b). In this case, one can observe dispersive behavior for ε_{2r} and dissipative behavior for ε_{2i}. At $\omega=\omega_0$, $\varepsilon_{2r}=0$; ε_{2i} has a maximum value

$$(\varepsilon_{2i})_{\max} = \frac{\omega_p^2 f df L}{\omega_0} = df\,(\varepsilon_{1i})_{\max}. \tag{1.25}$$

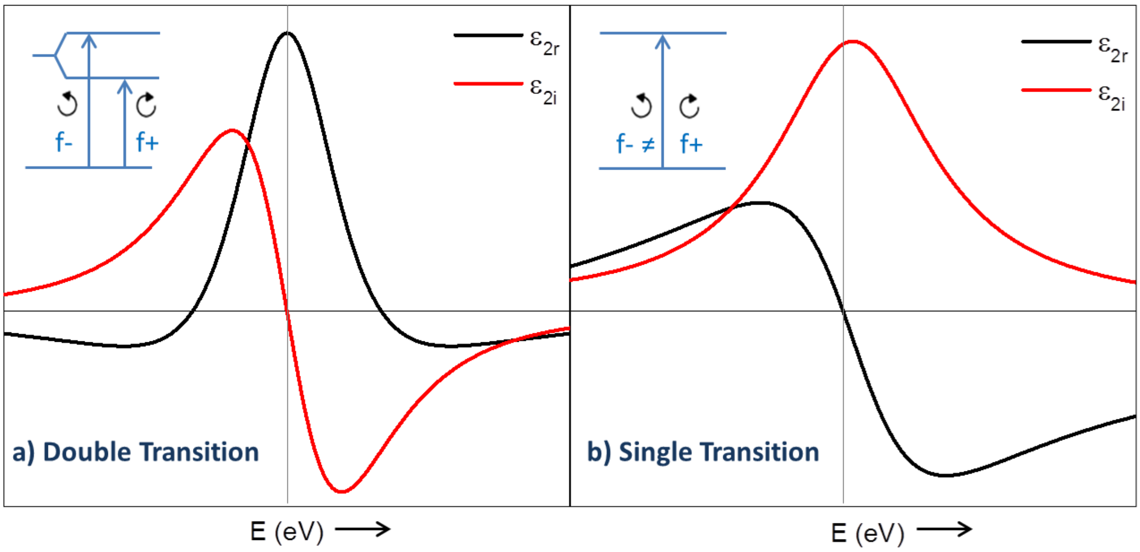

Figure 1.3: The calculated spectra of e_{2r} and e_{2i} for a) Dia transition and b) Para transition.

2. LIGHT POLARIZATION, OPTICAL AND MAGNETOOPTICAL EFFECTS

This chapter is a brief introduction to the light polarization and Jones vector formalism, which is a powerful tool when calculating polarization properties of light. Furthermore, we discussed in here SE and MO effects which are all based on the change in the polarization state of light upon reflection or transmission.

2.1. Light polarization

Light is understood as a general transverse electromagnetic radiation. Polarization of an electro-magnetic light wave is given by the time-dependent evolution of the electric field vector *E*. There are many ways to describe the polarization state of fully polarized electromagnetic waves. Since the electromagnetic light wave is generally elliptically polarized, we most often operate with the parameters of the polarization ellipse (Figure 2.1): azimuth θ, ellipticity e; and Jones vector formalism [9, 10].

- Azimuth, ($-\pi/2 \leq \theta < \pi/2$) is an oriented angle between the x-axis of the Cartesian coordinate system and the semi-major axis of the polarization ellipse. In this work, we choose the positive sign of the azimuth for the counterclockwise orientation.

- Ellipticity e, ($-1 \leq e \leq 1$) is a proportion of minor a and b axes of the polarization ellipse. At the same time, we introduce variable ellipticity (ellipticity angle) ϵ. In this work, we choose the positive sign of the ellipticity for the clockwise orientation.

$$e = \pm \frac{a}{b} = \tan \epsilon \tag{2.1}$$

The polarization state of light waves can be completely determined by using parameters of the polarization ellipse.

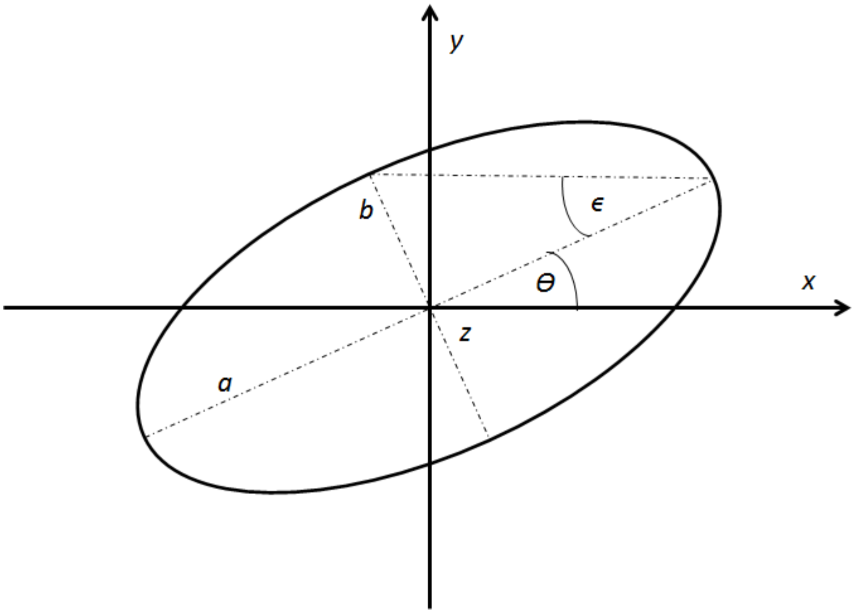

Figure 2.1: The polarization ellipse and basic MO parameters.

2.2. Jones vector formalism

Jones vector formalism describes the polarization state of light by two-dimensional complex vector whose coordinates are given by the choice of the polarization base. If we choose the polarization base as two orthogonal polarization amplitudes a_1 and a_2, with a phase difference δ, and if we define an angle as $\tan\alpha = a_2/a_1$, then we can express normalized Jones vector in a form

$$J = \begin{bmatrix} \cos\alpha \\ \sin\alpha e^{i\delta} \end{bmatrix}. \tag{2.2}$$

In the Cartesian-base of linear polarizations are Jones vectors for:

- linear polarization along the x and y axis [10]

$$E_x = \begin{bmatrix} 1 \\ 0 \end{bmatrix}, E_y = \begin{bmatrix} 0 \\ 1 \end{bmatrix}, \tag{2.3}$$

- general elliptical polarization [10]

$$J_{xy} = \begin{bmatrix} \cos\theta\cos\epsilon - i\sin\theta\sin\epsilon \\ \sin\theta\cos\epsilon + i\cos\theta\sin\epsilon \end{bmatrix}. \tag{2.4}$$

General complex Jones vector describes the polarization ellipse well, but it contains information of the initial phase and amplitude, which is redundant for the description of the polarization state of light. For this reason, we introduce a complex number, complex polarization parameter χ, defined as proportion of the first and second component of the Jones vector. Complex parameter of polarization for the polarization ellipse expressed by the Jones vector (2.4) thus has following form [9]

$$\chi_{xy} = \frac{E_y}{E_x} = \frac{\sin\theta\cos\epsilon + i\cos\theta\sin\epsilon}{\cos\theta\cos\epsilon - i\sin\theta\sin\epsilon} = \frac{\tan\theta + i\tan\epsilon}{1 - i\tan\theta\tan\epsilon}. \tag{2.5}$$

For small angles θ and ϵ it is possible, after approximations $\tan\theta=\theta$ *and* $\tan\epsilon=\epsilon$ (restricted to members of the first order), rewrite this expression as

$$\chi_{xy} \approx \theta + i\epsilon. \tag{2.6}$$

Jones formalism in Cartesian representation enables simplified and effective description of the polarized light properties after reflection or transmission on the sample. In here we choose the base of Cartesian system defined by *s* (*E* in the plane of incidence) and *p* (*E* perpendicular to the plane of incidence) polarizations. In this base, it is possible to express the effect of sample on the polarization state of incident light beam upon reflection by a reflection matrix S_R. Similarly, one can express the effect of sample on the polarization state of incident light beam upon transmission by a transmission matrix S_T [9].

$$S_R = \begin{bmatrix} r_{ss} & r_{sp} \\ r_{ps} & r_{pp} \end{bmatrix}, \tag{2.7}$$

$$S_T = \begin{bmatrix} t_{ss} & t_{sp} \\ t_{ps} & t_{pp} \end{bmatrix}. \tag{2.8}$$

In the first approximation, diagonal elements of the S_R and S_T matrices correspond to the Fresnel coefficients. Off-diagonal elements (in the first approximation linear in magnetization) describe the interaction between s and p waves that is occurring in anisotropic media.

Let us describe the incident wave by Jones vector Jin; reflected wave by Jones vector and transmitted wave by Jones vector . Using reflection and transmission matrices, one can define relations between those as follows [9]

$$J_{out}^{R} = S_R \cdot J_{in}, \qquad J_{out}^{T} = S_T \cdot J_{in}. \tag{2.9}$$

2.3. Spectroscopic Ellipsometry

Spectroscopic ellipsometry is a very sensitive measurement technique that uses polarized light to characterize thin films, surfaces and material microstructure [11]. Ellipsometry is useful technique which allows to determine material properties such as: film thickness, refractive index, complex permittivity function, conductance, absorption, surface roughness, interfacial regions, sample composition, film composition, crystallinity, optical anisotropy, uniformity, alloy ratio and depth profile of material properties. This technique measures the change in the polarization state of the reflected or transmitted light and compares it to a model (Figure 2.2).

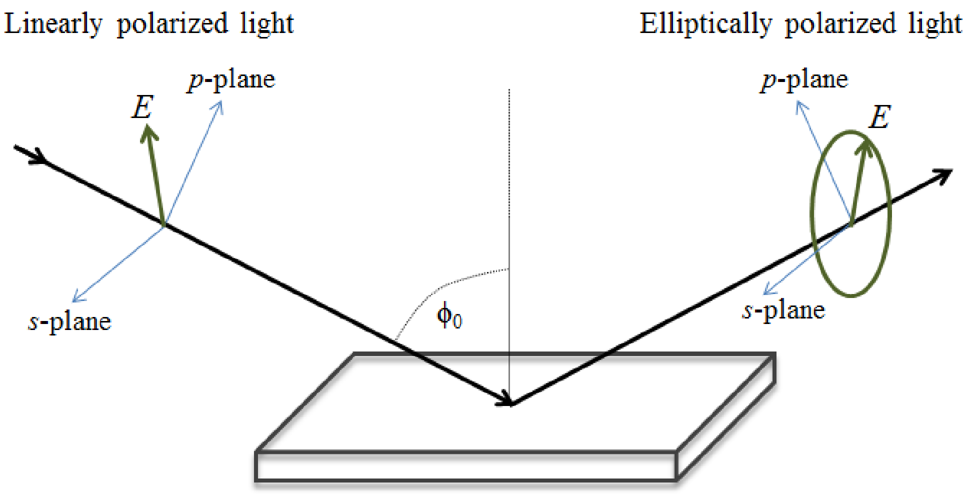

Figure 2.2: Geometry of an ellipsometric experiment

It is possible to derive the diagonal elements of the permittivity tensor from SE data analysis. We can express the change in the polarization state of the reflected beam by the SE parameters amplitude ratio ψ and phase difference Δ, which are defined as

$$\tan\psi \cdot e^{i\Delta} = \rho = \frac{r_{pp}}{r_{ss}} \tag{2.10}$$

In this equation, tanψ is the magnitude of the reflectivity ratio, Δ is the phase change between *s* and *p* polarized light. The r_{pp} and r_{ss} are the amplitude reflection coefficients for s and p polarization measured from the alternating current signal [2]. The important part of SE analysis is the proper parametrization of the dispersion of unknown optical functions. For purposes of parameterization are oscillators/terms defined in the subchapter 1.1.2 fitted to the resulted optical functions spectra.

2.4. Magnetooptical effects

In this work, we use MOKE and MO Faraday effect to study the physical properties of magnetic materials and magnetic layered structures. These phenomena are characteristic by changes in the polarization state of the reflected or transmitted light caused by magnetic ordering [9]. In the MOKE experiment, we study these changes upon light reflection. However, in the Faraday effect experiment we study these changes upon light transmission.

a) Magneto-optical Kerr effect

We can categorize MOKE (based on the mutual orientation of the incidence plane, the reflection plane of the sample and the magnetization vector *M*) into three basic configurations: polar, longitudinal and transversal (Figure 2.3).

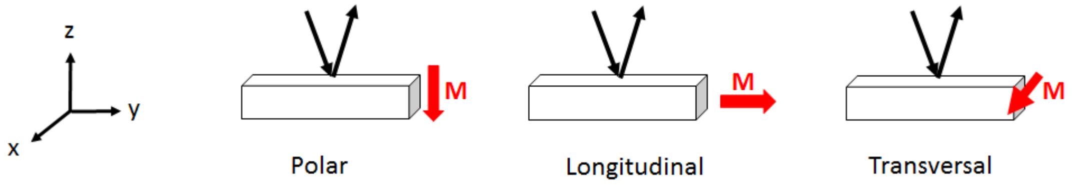

Figure 2.3: Basic configurations for measuring the MOKE.

Taking into account the geometry of these configurations, we can simplify the permittivity tensor to forms

$$\varepsilon_P = \begin{bmatrix} \varepsilon_1 & -i\varepsilon_2 & 0 \\ i\varepsilon_2 & \varepsilon_1 & 0 \\ 0 & 0 & \varepsilon_1 \end{bmatrix}, \tag{2.11}$$

$$\varepsilon_L = \begin{bmatrix} \varepsilon_1 & 0 & -i\varepsilon_2 \\ 0 & \varepsilon_1 & 0 \\ i\varepsilon_2 & 0 & \varepsilon_1 \end{bmatrix}, \tag{2.12}$$

$$\varepsilon_T = \begin{bmatrix} \varepsilon_1 & 0 & 0 \\ 0 & \varepsilon_1 & -i\varepsilon_2 \\ i\varepsilon_2 & 0 & \varepsilon_1 \end{bmatrix}. \tag{2.13}$$

where ε_P stands for permittivity tensor in the polar, ε_L in the longitudinal and ε_T in the transversal configuration. In these geometries, also reflection matrix S_R defined by equation (2.7) takes different forms

$$S_{R\_polar} = \begin{bmatrix} r_{ss} & r_{sp} \\ r_{ps} & r_{pp} \end{bmatrix}, \qquad S_{R\_long} = \begin{bmatrix} r_{ss} & -r_{ps} \\ r_{ps} & r_{pp} \end{bmatrix}, \qquad S_{R\_trans} = \begin{bmatrix} r_{ss} & 0 \\ 0 & r_{pp} \end{bmatrix}. \tag{2.14}$$

Physical meaning of S_R matrix elements then allows defining of MO parameters, Kerr rotation θ_K and Kerr ellipticity ϵ_K, for *s* and *p* polarized waves as follows [9]

$$\theta_{Ks} - i\epsilon_{Ks} \approx \Phi_{Ks} \equiv -\frac{r_{ps}}{r_{ss}}, \tag{2.15}$$

$$\theta_{Kp} - i\epsilon_{Kp} \approx \Phi_{Kp} \equiv \frac{r_{sp}}{r_{pp}}. \tag{2.16}$$

In case of normal incidence of the light beam, given sign convention provides equal values of MO parameters $\Phi_{Ks} = \Phi_{Kp}$.

b) Magneto-optical Faraday effect

We usually measure the Faraday effect in the configuration shown in the Figure 2.4.

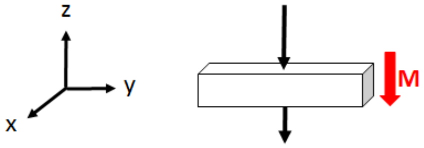

Figure 2.4: Basic configuration for measuring the Faraday effect.

Taking into account the geometry of this configuration, we can simplify the permittivity tensor to the form

$$\varepsilon_F = \begin{bmatrix} \varepsilon_1 & -i\varepsilon_2 & 0 \\ i\varepsilon_2 & \varepsilon_1 & 0 \\ 0 & 0 & \varepsilon_1 \end{bmatrix}. \tag{2.17}$$

In this geometry are the transmission matrix S_T elements defined by equation (2.8). Therefore, we can define MO parameters, Faraday rotation θ_F and Faraday ellipticity ϵ_F, for *s* and *p* polarized waves as follows [9]

$$\theta_{Fs} - i\epsilon_{Fs} \approx \Phi_{Fs} \equiv -\frac{t_{ps}}{t_{ss}}, \tag{2.18}$$

$$\theta_{Fp} - i\epsilon_{Fp} \approx \Phi_{Fp} \equiv -\frac{t_{sp}}{t_{pp}}. \tag{2.19}$$

In case of normal incidence of the light beam, given sign convention provides equal values of MO parameters $\Phi_{Fs} = \Phi_{Fp}$.

3. ELECTROMAGNETIC WAVES IN ANISOTROPIC MEDIUM

In the previous chapter, we briefly introduced the description of the polarization state of light, SE and MO effects. However, for a deeper analysis of the optical and MO response of thin films and multilayers, we need a macroscopic analysis of the optical interaction of the polarized light with a substance. We will discuss this interaction in the following paragraphs devoted to the behavior of polarized light in anisotropic media.

3.1. Wave equation in anisotropic media

We can describe the polarized monochromatic electromagnetic plane wave incident from the vacuum on the anisotropic environment without free charges by Maxwell's equations [9, 10]

$$\nabla \times E + \frac{\partial B}{\partial t} = 0, \tag{3.1}$$

$$\nabla \cdot D = 0, \tag{3.2}$$

$$\nabla \times H - \frac{\partial D}{\partial t} = 0, \tag{3.3}$$

$$\nabla \cdot B = 0, \tag{3.4}$$

where the material equations are

$$D = \varepsilon_0 \varepsilon E, \tag{3.5}$$

$$B = \mu_0 \mu H. \tag{3.6}$$

From Maxwell’s equations, we derive the wave equation in the traditional way

$$\Delta E - \frac{\varepsilon}{c^2}\frac{\partial E}{\partial t^2} - \nabla(\nabla \cdot E) = 0. \tag{3.7}$$

We are looking for its solution in the shape of a plane wave

$$E = E_0 e^{i(\omega t - k \cdot r)}. \tag{3.8}$$

If we introduce a reduced wave vector N

$$N = \frac{c}{\omega} k, \tag{3.9}$$

we may rewrite the original wave equation into a matrix form [9]

$$\begin{bmatrix} \varepsilon_{xx} - N_y^2 - N_z^2 & \varepsilon_{xy} & \varepsilon_{xz} \\ \varepsilon_{yx} & \varepsilon_{yy} - N_z^2 & \varepsilon_{yz} - N_y N_z \\ \varepsilon_{zx} & \varepsilon_{zy} - N_y N_z & \varepsilon_{zz} - N_y^2 \end{bmatrix} \begin{bmatrix} E_{0x} \\ E_{0y} \\ E_{0z} \end{bmatrix} = 0. \tag{3.10}$$

In this derivation we assumed the plane of incidence perpendicular to the x-axis ($N_x = 0$), and thus the component of the reduced wave vector N_y derived from a Snell's law in shape

$$N_y = N_0 \sin \varphi_0, \tag{3.11}$$

where N_0 is a real refractive index of the isotropic medium and φ_0 is an angle of incidence of the electromagnetic wave. For the case of zero determinant, one can find a nontrivial solution of the equation (3.10) as a characteristic equation of 4-th order for N_z

$$\begin{gathered} N_z^4 \varepsilon_{zz} + N_z^3 [N_y (\varepsilon_{yz} + \varepsilon_{zy})] - \\ -N_z^2 [\varepsilon_{yy} (\varepsilon_{zz} - N_y^2) + \varepsilon_{zz} (\varepsilon_{xx} - N_y^2) - \varepsilon_{xz} \varepsilon_{zx} - \varepsilon_{yz} \varepsilon_{zy}] - \\ -N_y N_z [(\varepsilon_{xx} - N_y^2)(\varepsilon_{yz} + \varepsilon_{zy}) - \varepsilon_{xy} \varepsilon_{zx} - \varepsilon_{yx} \varepsilon_{xz}] + \\ +\varepsilon_{yy} [(\varepsilon_{xx} - N_y^2)(\varepsilon_{zz} - N_y^2) - \varepsilon_{xz} \varepsilon_{zx}] - \\ -\varepsilon_{xy} \varepsilon_{yz} (\varepsilon_{zz} - N_y^2) - \varepsilon_{yz} \varepsilon_{zy} (\varepsilon_{xx} - N_y^2) + \varepsilon_{xy} \varepsilon_{zx} \varepsilon_{yz} + \varepsilon_{yx} \varepsilon_{xz} \varepsilon_{zy} = 0. \end{gathered} \tag{3.12}$$

The roots of the characteristic equation (3.12) correspond to four proper modes of light propagation in anisotropic media N_{zj}. Two of these modes propagate with $+k$ in the forward direction and two with $-k$ in the reverse direction. Eigenvectors of these modes for the general permittivity tensor shape are

$$e_j = \begin{bmatrix} -\varepsilon_{xy} (\varepsilon_{zz} - N_y^2) + \varepsilon_{xz} (\varepsilon_{zy} + N_y N_{zj}) \\ (\varepsilon_{zz} - N_y^2)(\varepsilon_{xx} - N_y^2 - N_{zj}^2) - \varepsilon_{xz} \varepsilon_{zx} \\ -(\varepsilon_{xx} - N_y^2 - N_{zj}^2)(\varepsilon_{zy} - N_y N_{zj}) - \varepsilon_{zx} \varepsilon_{xy} \end{bmatrix}. \tag{3.13}$$

Linear superposition of these four modes of light propagation in anisotropic media gives a general solution of the wave equation

$$E = \sum_{j=1}^{4} E_{0_j} e_j e^{i[\omega t - \frac{\omega}{c}(N_y y + N_{z_j} z)]}. \qquad (3.14)$$

One can greatly simplify this solution when working with the case of the general anisotropic medium in polar and longitudinal configuration.

- In the polar configuration is permittivity tensor given by equation (2.11). Wave equation in this case leads to a simplified characteristic equation whose solutions correspond to the four proper modes of the light propagation N_{zj} [9]

$$N_{z1} = N_{z+}, \qquad N_{z2} = -N_{z+}, \qquad N_{z3} = N_{z-}, \qquad N_{z4} = -N_{z-}, \qquad (3.15)$$

where

$$N_{z\pm} = \sqrt{(\varepsilon_1 - N_y^2)(1 \pm \frac{\varepsilon_2}{\sqrt{\varepsilon_1(\varepsilon_1 - N_y^2)}})}. \qquad (3.16)$$

- In the longitudinal configuration is permittivity tensor given by equation (2.12) and wave equation leads to the characteristic equation with solutions N_{zj} [9]

$$N_{z1} = N_{z+}, \qquad N_{z2} = -N_{z+}, \qquad N_{z3} = N_{z-}, \qquad N_{z4} = -N_{z-}, \qquad (3.17)$$

where

$$N_{z\pm} = \sqrt{\varepsilon_1 - N_y^2 - \frac{\varepsilon_2}{2\varepsilon_1}(\pm\sqrt{(4\varepsilon_1 N_y^2 + \varepsilon_2^2} - \varepsilon_2)}. \qquad (3.18)$$

3.2. Yeh 4x4 matrix formalism

Up to this point we have covered only the propagation of electromagnetic waves in anisotropic environment. However, for the evaluation of the MO experiments on multilayers, we must extend this description. The reason is that the interaction of light in a layered structure with sufficiently thin layers depends on all the layers contribution. This fact forces us to introduce a formalism that allows clear description of the interaction of electromagnetic radiation with magnetic multilayer, Yeh 4x4 matrix formalism [12].

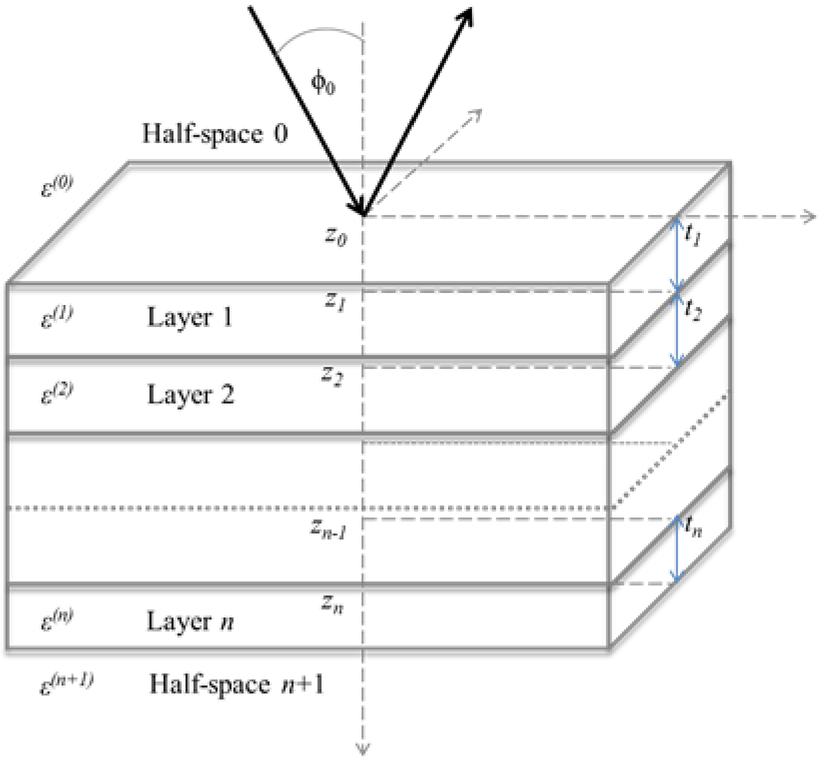

Figure 3.1: Anisotropic multilayered structure. The individual layers are characterized by electric permittivity $\varepsilon^{(n)}$ and the thickness $t^{(n)}$, $n = 1, 2. . . n$. Angle of incidence in the half-space *0* is labeled φ_0. Planar interfaces of layers are perpendicular to the *z*-axis, plane of incidence is perpendicular to the *x*-axis.

Let us consider multilayer made of *n* layers with mutually parallel interfaces perpendicular to the z-axis (Figure 3.1). Neighboring isotropic half-spaces *0* and *n + 1* will be described by scalar electric permittivity *ε(0)* and *ε(n + 1)*. Boundary conditions of continuity of vectors *E* and *B* tangential components on individual interfaces allow us to tie relations of electromagnetic fields in *n* and *n + 1* layers. It can be done in the representation of linear transformations of proper modes, which can be expressed in matrix form as

$$D^{(n-1)}E_0^{(n-1)}(z_n-1)=D^{(n)}P^{(n)}E_0^{(n)}(z_n). \tag{3.19}$$

Here P stands for a Propagation matrix

$$P_{ij}^{(n)}=\delta_{ij}\exp(i\frac{\omega}{c}\bar{N}_{zj}^{(n)}t_n), \tag{3.20}$$

where δ_{ij} is a Kronecker delta and t_n represents a thickness of the *n*-th layer. *D* represents a Dynamical matrix whose elements have form [9, 12, 13]

$$D_{1j}^{(n)} = -\varepsilon_{xy}^{(n)}(\varepsilon_{zz}^{(n)} - N_y^2) + \varepsilon_{xz}^{(n)}(\varepsilon_{zy}^{(n)} - N_y N_{zj}^{(n)}), \tag{3.21}$$

$$D_{2j}^{(n)} = N_{zj}^{(n)}[-\varepsilon_{xy}^{(n)}(\varepsilon_{zz}^{(n)} - N_y^2) + \varepsilon_{xz}^{(n)}(\varepsilon_{zy}^{(n)} - N_y N_{zj}^{(n)})], \tag{3.22}$$

$$D_{3j}^{(n)} = (\varepsilon_{zz}^{(n)} - N_y^2)(\varepsilon_{xx}^{(n)} - N_y^2 - N_{zj}^{(n)2}) - \varepsilon_{xz}^{(n)}\varepsilon_{zx}^{(n)}, \tag{3.23}$$

$$\begin{gathered} D_{4j}^{(n)} = -(\varepsilon_{xx}^{(n)} - N_y^2 - N_{zj}^{(n)^2})(N_y\varepsilon_{zy}^{(n)} + N_{zj}\varepsilon_{zz}^{(n)}) + \\ + N_{zj}^{(n)}\varepsilon_{xz}^{(n)}\varepsilon_{zx}^{(n)} + N_y\varepsilon_{zx}^{(n)}\varepsilon_{xy}^{(n)}. \end{gathered} \tag{3.24}$$

By modification of equation (3.19) it is possible to introduce the transfer matrix *T*, which ties up the field between *(n-1)* and the *n*-th layer.

$$E_0^{(n-1)}(z_{n-1}) = (D^{(n-1)})^{-1} D^{(n)} P^{(n)} E_0^{(n)}(z_n) = T^{(n-1,n)} E_0^{(n)}(z_n). \tag{3.25}$$

By application of the equation (3.25) for each interface of the multilayer, it is possible to express relationship between the incident waves passing through the first interface and the wave passing through the *n*-th interface as

$$E_0^{(0)}(z_0) = (\prod_{n=1}^{n+1} T^{(n-1,n)}) E_0^{(n+1)}(z_n) = M E_0^{(n+1)}(z_n). \tag{3.26}$$

Relation (3.26) defines a matrix of the multilayered structure *M*. This matrix can characterize any layered anisotropic structure, and it is sufficient to determine reflection coefficients of the structure. If we consider that the source of electromagnetic radiation is strictly in the upper half-space *0* (from lower half-space is not coming any radiation and so E_{02} and E_{04} are equal zero), we can express reflection coefficients by components of matrix *M* as [9, 12]

$$r_{12} = \left(\frac{E_{02}^{(0)}(z_0)}{E_{01}^{(0)}(z_0)} \right)_{E_{03}^{(0)}(z_0)=0} = \frac{M_{21}M_{33} - M_{23}M_{31}}{M_{11}M_{33} - M_{13}M_{31}}, \tag{3.27}$$

$$r_{14} = \left(\frac{E_{04}^{(0)}(z_0)}{E_{01}^{(0)}(z_0)} \right)_{E_{03}^{(0)}(z_0)=0} = \frac{M_{41}M_{33} - M_{43}M_{31}}{M_{11}M_{33} - M_{13}M_{31}}, \tag{3.28}$$

$$r_{34} = \left(\frac{E_{04}^{(0)}(z_0)}{E_{03}^{(0)}(z_0)} \right)_{E_{01}^{(0)}(z_0)=0} = \frac{M_{11}M_{43} - M_{41}M_{13}}{M_{11}M_{33} - M_{13}M_{31}}, \tag{3.29}$$

$$r_{32} = \left(\frac{E_{02}^{(0)}(z_0)}{E_{03}^{(0)}(z_0)} \right)_{E_{01}^{(0)}(z_0)=0} = \frac{M_{11}M_{23} - M_{21}M_{13}}{M_{11}M_{33} - M_{13}M_{31}}. \tag{3.30}$$

Similarly, we can express transmission coefficients as [9, 12]

$$t_{11} = \left(\frac{E_{01}^{(m+1)}(z_0)}{E_{01}^{(0)}(z_0)} \right)_{E_{03}^{(0)}(z_0)=0} = \frac{M_{33}}{M_{11}M_{33} - M_{13}M_{31}}, \tag{3.31}$$

$$t_{14} = \left(\frac{E_{03}^{(m+1)}(z_m)}{E_{01}^{(0)}(z_0)} \right)_{E_{03}^{(0)}(z_0)=0} = \frac{-M_{31}}{M_{11}M_{33} - M_{13}M_{31}}, \tag{3.32}$$

$$t_{33} = \left(\frac{E_{04}^{(m+1)}(z_m)}{E_{03}^{(0)}(z_0)} \right)_{E_{01}^{(0)}(z_0)=0} = \frac{M_{11}}{M_{11}M_{33} - M_{13}M_{31}}, \tag{3.33}$$

$$t_{31} = \left(\frac{E_{01}^{(m+1)}(z_m)}{E_{03}^{(0)}(z_0)} \right)_{E_{01}^{(0)}(z_0)=0} = \frac{-M_{13}}{M_{11}M_{33} - M_{13}M_{31}}. \tag{3.34}$$

For linearly polarized modes, it is possible to define these coefficients as the elements of Jones reflection matrices S_R and S_T

$$S_R = \begin{bmatrix} r_{ss} & r_{sp} \\ r_{ps} & r_{pp} \end{bmatrix} = \begin{bmatrix} r_{12} & r_{32} \\ -r_{14} & -r_{34} \end{bmatrix}, \tag{3.35}$$

$$S_T = \begin{bmatrix} t_{ss} & t_{sp} \\ t_{ps} & t_{pp} \end{bmatrix} = \begin{bmatrix} t_{11} & t_{31} \\ t_{13} & t_{33} \end{bmatrix}. \tag{3.36}$$

and thus determine the MO parameters θ_K, ε_K and θ_F, ε_F.

3.3. Proper modes in isotropic media

Permittivity of isotropic, in our case a non-magnetic environment, is a scalar and it is given by equation $\varepsilon_1 = N^{(n)2}$. In this case, proper modes calculation procedure above leads to a solution with e_j components equal zero. Therefore, we calculate here with constant N_y. This approach determines two possible directions of the wave vector

$$\gamma_{1,2} = \frac{\omega}{c}\left[N_y i_y \pm Q^{(n)} i_z \right], \tag{3.37}$$

where a parameter Q is calculated from

$$Q^{(n)} = \sqrt{N^{(n)^2} - N_y^2}. \tag{3.38}$$

This approach allows constructing the Dynamical matrix for isotropic environment in form [9]

$$D^{(n)} = \begin{bmatrix} 1 & 1 & 0 & 0 \\ Q^{(n)} & -Q^{(n)} & 0 & 0 \\ 0 & 0 & Q^{(n)}/N^{(n)} & Q^{(n)}/N^{(n)} \\ 0 & 0 & -N^{(n)} & N^{(n)} \end{bmatrix} \tag{3.39}$$

and its inverse

$$\left[D^{(n)}\right]^{-1} = \begin{bmatrix} Q^{(n)} & 1 & 0 & 0 \\ Q^{(n)} & -1 & 0 & 0 \\ 0 & 0 & N^{(n)} & -Q^{(n)}/N^{(n)} \\ 0 & 0 & N^{(n)} & Q^{(n)}/N^{(n)} \end{bmatrix}. \tag{3.40}$$

3.4. Effective medium approximation

Interfaces and surfaces of real nanolayers are not perfect. Imperfections often contribute to the deviation between optical and MO experimental data versus theoretical models. The effective medium approximation method (EMA) can eliminate and quantitatively estimate this effect. The principle of this method lies in the consideration of the roughness or interface as a separate layer. This layer is constructed from two materials: the material of the first layer that forms interface and the material of the second layer that forms interface. Figure 3.2 shows geometric model of this approach. In this model is the material of the first layer dissolved in the form of spherical objects in the material of the second layer.

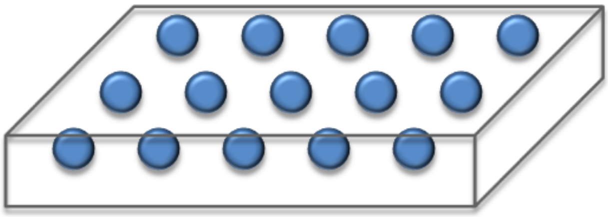

Figure 3.2: Geometric model of the effective medium approximation method

Here, we define permittivity tensor of the first layer that forms interface ε_1 by its diagonal elements ε_{11} and off-diagonal elements ε_{12} and we rewrite it to the form $\varepsilon_1 = \varepsilon_{11} - i\varepsilon_{12}$. Similarly, we can define the permittivity tensor of the second layer that forms interface $\varepsilon_2 = \varepsilon_{21} - i\varepsilon_{22}$ by diagonal elements ε_{21} and off-diagonal elements ε_{22}. Now, we can use our geometric model (Figure 3.2) and define the interface layer permittivity tensor by diagonals ε_{R1} and off-diagonals ε_{R2} using transformation relations

$$\varepsilon_{R1} = \varepsilon_{12} + f\,\frac{\varepsilon_{11} - \varepsilon_{12}}{1 + \frac{(1-f)(\varepsilon_{11} - \varepsilon_{12})}{3\varepsilon_{12}}} \tag{3.41}$$

$$\varepsilon_{R2} = f\,\frac{\varepsilon_{21}}{1 + \frac{(1-f)(\varepsilon_{11} - \varepsilon_{12})}{3\varepsilon_{12}}}. \tag{3.42}$$

Coefficient f corresponds to the volume fraction of the second material forming the interface (for example, f = 0.5 corresponds to 50% of the second material in the mixture) [14].

For the case of the surface roughness calculations, we assume the second material to be void. If we rewrite the permittivity tensor of the layer material to the form $\varepsilon_1 = \varepsilon_{11} - i\varepsilon_{12}$ then we can calculate permittivity tensor of the surface roughness layer $\varepsilon_R = \varepsilon_{R1} - i\varepsilon_{R2}$ using equation

$$0 = (1-f)\frac{\varepsilon - \varepsilon_R}{\varepsilon + 2\varepsilon_R} + \frac{1 - \varepsilon_R}{1 + 2\varepsilon_R} \tag{3.43}$$

In this formula, f denotes the volume fraction of the void in the mixture.

4. EXPERIMENTAL TECHNIQUES

In this chapter we discuss briefly experimental techniques used for acquirement of experimental data in this work. We start this section with a brief introduction to spectroscopic ellipsometer, which is used for measurements of thin film optical properties and allows determination of thin film optical functions (complex permittivity tensor). Afterwards, we continue with an introduction to measurements of weak MO effects: MOKE and Faraday effect. Spectra of MO effects contain important information about electronic structure of thin films and allow determination of the full permittivity tensor.

4.1. Spectroscopic ellipsometer

As explained previously, ellipsometric spectroscopy measures changes in the polarization state of light upon reflection or transmission on the sample. In this chapter, we discuss basic setup for this type of measurement.

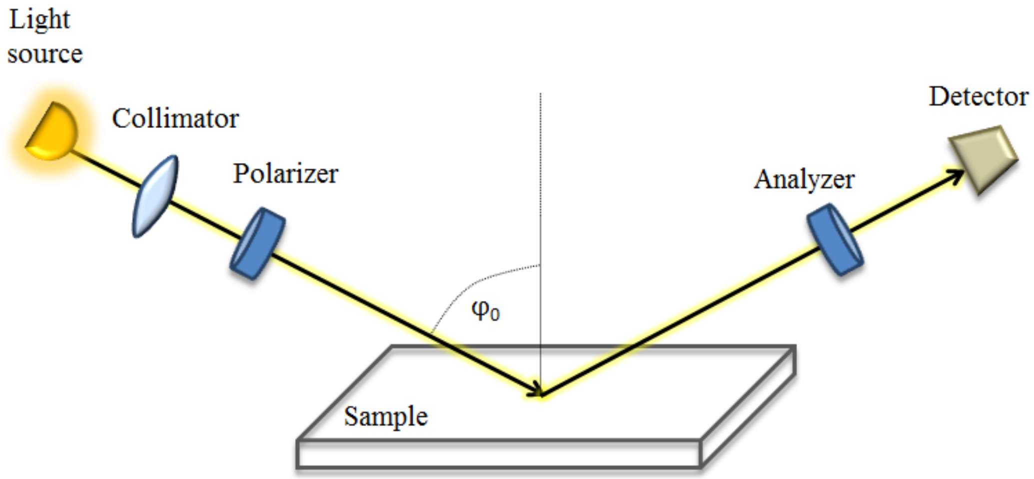

Figure 4.1: Scheme of the basic ellipsometric setup

All spectroscopic ellipsometer arrangements start with a light source and end with a detector that converts light into voltage. It is an arrangement of the optical components between that defines the type of ellipsometer being used. In this work, we use Muller matrix ellipsometer Woolam RC2 with dual rotating compensators and multichannel detection working in the photon energy range from 1.24 to 6.5 eV. Further details on this complicated device can be found in [2, 11]. However, for our purposes, here we discuss only the basic set-up of ellipsometer shown in the Figure 4.1. It is constructed from a rotating polarizer that rotates on frequency ω, sample and analyzer. For this type of setup and general elliptical polarization, one can determine alternating current signal on detector I as

$$I \approx 1 + \alpha \cdot \cos(2\omega t) + \beta \cdot \sin(2\omega t) \tag{4.1}$$

The two important quantities are α and β, which are normalized Fourier coefficients of the signal. One can represent these coefficients in terms of the ψ and Δ defined in the chapter 2.2 and the known polarizer azimuthal angle P as follows ($P=0°$ is in the plane of incidence)

$$\alpha = \frac{\tan^2\psi - \tan^2 P}{\tan^2\psi + \tan^2 P} \tag{4.2}$$

$$\beta = \frac{2\tan\psi\cos\Delta\tan P}{\tan^2\psi + \tan^2 P} \tag{4.3}$$

Solution for ψ and Δ has a form

$$\tan\psi = \sqrt{\frac{1+\alpha}{1-\alpha}}\left|\tan P\right|, \tag{4.4}$$

$$\cos\Delta = \frac{\beta}{\sqrt{1-\alpha^2}} \cdot \frac{\tan P}{\left|\tan P\right|}. \tag{4.5}$$

These equations form the basis of the ellipsometric measurement with a rotating analyzer ellipsometer [11].

For experimental data analyses, we use CompleteEASE software that compares the data acquired by the ellipsometer with an advanced theoretical model of studied multilayer. This model defines the multilayer as a structure that consists of separate layers determined by theirs optical functions (complex permittivity), thicknesses and also a position in the structure. In this work, we use “**Multi Sample Analysis**” (MSA) mode in CompleteEASE software multiple times. MSA is an advanced mode that allows multiple samples to be fitted simultaneously with some of fit parameters common to all samples and other allowed to vary (optical functions of materials, thicknesses, roughness, backside reflections, angle offset,…) [2]. Therefore, MSA allows suppressing the fit error and so more precise analysis. This mode is especially useful, when there are transmission data available. In this case, we are using MSA to fit one theoretical model to the ellipsometric and transmission data simultaneously. This approach is especially meaningful when fitting constants of transparent materials with a bandgap in the measured spectral range.

4.2. Magneto-optical spectroscopy

The simplest way to define MO spectroscopy is to say that it is SE performed in the magnetic field. Therefore, MOKE spectroscopy is basically SE which measures a change in the polarization state of light upon reflection on the sample in magnetic field. Similarly, Faraday effect spectroscopy is SE which measures a change in the polarization state of light upon transmission on the sample in magnetic field. These types of measurements are useful for non-destructive probing of magnetic properties of non-transparent (MOKE) or transparent (Faraday) magnetic materials and nanostructures. Since some materials have absorption edge within measured spectral range, it is a classical approach to combine these measurements for different parts of spectra.

In this work, we measure MOKE by method of nearly crossed polarizators. Figure 4.2 shows very basic scheme of this method: the light beam passing through polarizer, reflecting on the sample in magnetic field, passing through the phase plate and finally through analyzer to the detector. For this type of MOKE setup and general elliptical polarization, one can determine intensity on the detector I as

$$I \approx \cos^2 \gamma + |\Phi_K|^2 \sin^2 \gamma + \sin(2\gamma)\Re(\Phi_K e^{i\delta}) \tag{4.6}$$

Here, γ is an angle between analyzer and polarizer with respect to the crossed position and δ is a phase shift of the phase plate.

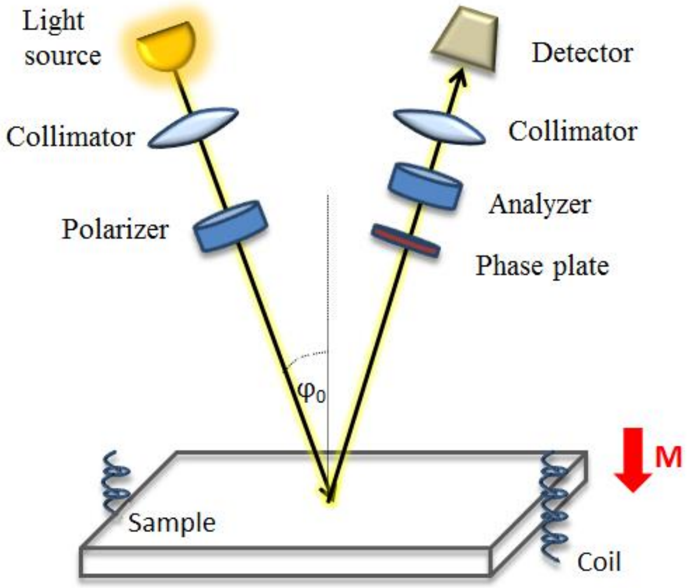

Figure 4.2: Scheme of the basic MOKE setup

If we restrict ourselves to effect linear in Φ_K, and add constant C corresponding to dark current in CCD, we can rewrite resulting dependence of detected intensity on the angle of analyzer α as

$$I \approx \cos^2 \gamma + (\theta_K \cos \delta + \epsilon_K \sin \delta) \sin 2\gamma + C \tag{4.7}$$

Since it is complicated to measure Kerr rotation θ_K and Kerr ellipticity ϵ_K in one measurement, it is usually measured separately. This is done by removing a phase plate, which results in $\delta=0$, therefore, we measure pure Kerr rotation. In order to extract ellipticity, we combine experiments with and without phase plate. For more details, one can see [15].

The basic setup for Faraday effect measurement can be seen in Figure 4.3: the light beam passing through polarizer, the sample in magnetic field and finally through analyzer to detector. For this type of setup, calculations lead to the same expression that it is for MOKE, except from the change in sign of term with MO effect.

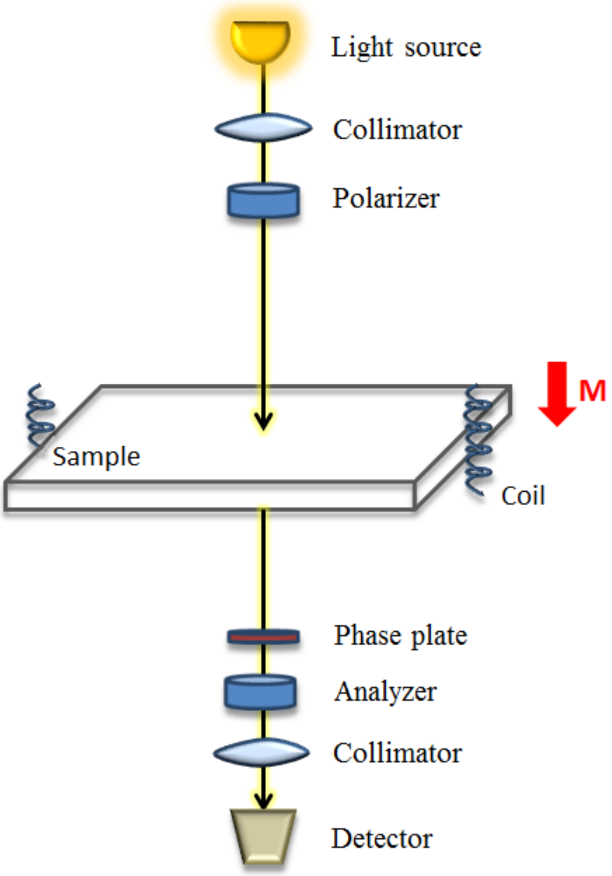

Figure 4.3: Scheme of the basic Faraday effect setup.

5. THIN FILM PREPARATION TECHNIQUES

In the previous chapter we discussed methods used for acquirement of experimental data in this work. Similarly, we devoted this chapter to techniques employed for the preparation of materials/samples studied in this work. These preparation techniques are relatively new, require advance technology and sometimes even allow preparation of bulk materials, thin films and nanostructures which do not normally exist in nature.

5.1 Vertical-gradient-freeze method

In this method is at first polycrystalline material produced by the horizontal synthesis [16]. Afterwards, it is cut into chunks which are placed in a crucible with a seed crystal of the required orientation. As one can see from the Figure 5.1, the crucible is then placed vertically in a furnace. In the furnace is created a temperature gradient with temperature increasing in the direction away from the seed, up to the length of the crystal. Single crystal growth propagates from the seed crystal and, because the crystal forms in the shape of the crucible, diameter control of the ingot is relatively simple [16].

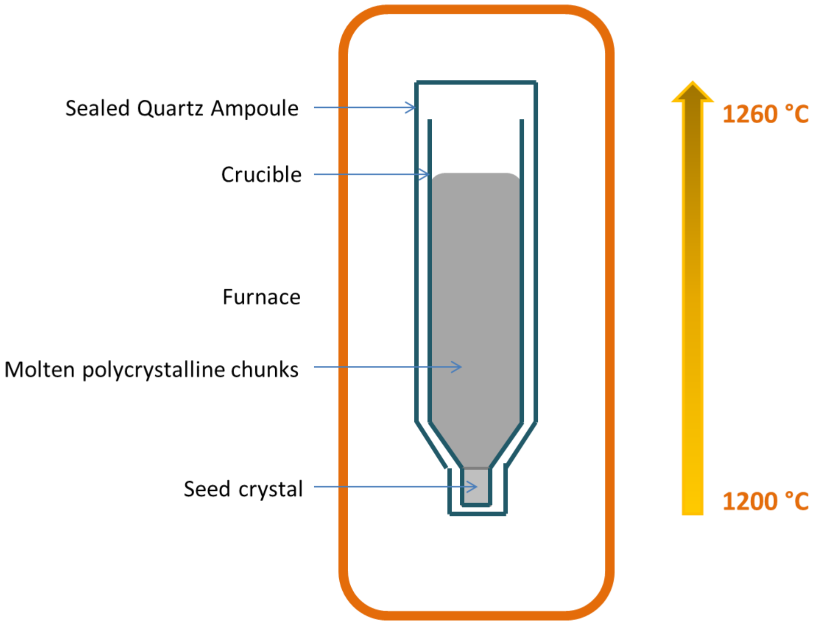

Figure 5.1: Vertical gradient freeze crystal growth

5.2. Sputter deposition

Sputter deposition is a thin films preparation method that involves bombardment of the target (material source) by energetic particles resulting in sputtering target atoms into the gas phase. Since these atoms are not in their thermodynamic equilibrium state, they tend to deposit on all surfaces in the vacuum chamber. Therefore a substrate placed in the chamber is coated with a thin film.

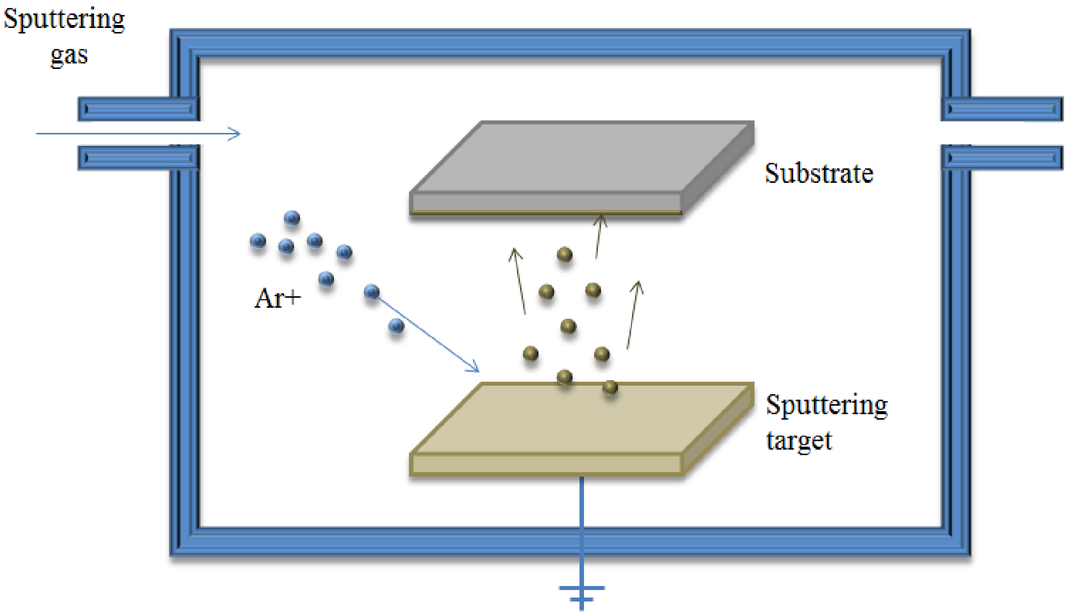

Figure 5.2: Sputter deposition.

Direct Current or DC Sputtering [17] is the most basic and inexpensive technique for deposition of metals or electrically conductive coating materials. Major advantages of this technique are easy control due to DC source and, when preparing metallic films, also low cost. The basic configuration of a DC Sputtering coating system is schematically shown in the Figure 5.2. It consists of the target material placed in a vacuum chamber parallel to the substrate. The vacuum chamber is evacuated to a low pressure and subsequently backfilled with a high purity inert gas. This inert gas is usually Argon with typical sputter pressure range from 0.5mTorr to 100mTorr. Argon is due to its relative mass and ability to convey kinetic energy within high energy molecular collisions in the plasma. Afterwards a DC current is applied to the target which serves as cathode or negative bias (point where electrons enter the system). Subsequently, a positive charge is applied to the substrate which serves as anode or positive charged bias. Firstly, the electrically neutral argon gas atoms are ionized due to the collisions with the negatively charged target, which ejects atoms off into the plasma. Secondly, the ionized argon atoms are driven to the anode substrate which is attracting ionized gas ions, electrons and the most importantly vaporized target material atoms. Finally, these atoms condense into a thin film coating on the substrate. While DC Sputtering is a great choice for preparation of multiple conductive coatings, its main limitation lies in non-conducting dielectric insulating materials. These take on a charge over time which usually results in quality issues like arcing, poisoning of the target material with a charge and even in the complete cessation of sputtering. To overcome these limitations, several technologies such as radio frequency sputtering have been developed.

Radio Frequency or RF Sputtering [17] is very similar to the DC sputtering technique. The difference lies in the alternating of the current electrical potential in the vacuum environment at radio frequencies. This is done to avoid a charge build up on certain types of target material. The charge buildup is cleaned every cycle during the positive cycle when electrons are attracted to the target giving it a negative bias. During the negative cycle, ion bombardment of the target continues normally. The alternating of the current electrical potential is performed by a capacitor. The capacitor is part of an impedance-matching network, which conveys the power transfer from the RF source to the plasma discharge. While RF Sputtering is extremely useful technique, it also has several disadvantages. For example, when using radio waves instead of DC current, deposition rates became considerably slower. Moreover, this technique requires significantly higher voltages (expensive power supplies requirement) to achieve the same deposition results as with DC, and so overheating (advanced circuitry requirement) also becomes an issue.

5.3. Metal Organic Decomposition

Metal Organic Decomposition (MOD) is a technique for manufacturing inorganic films without processing in vacuum or going through a gel or powder step [18]. The key to this method are metal-organic components, prepared by dissolving required element in an appropriate solvent. These metal-organic components are mixed in an appropriate ratio to give a metal-organic solution which results in desired cation stoichiometry for the final film. The simplified process of MOD can be seen in Figure 5.3. The first step is a deposition and spin coating of a metal-organic solution on a substrate and therefore a production of a wet film. Afterwards, the film is heated multiple times (drying, pre annealing). This is done in order to remove any solvent that did not evaporate during the deposition step and also in order to decompose the metal-organic compounds. At the end, this process results into inorganic film of some thickness. This thickness is constant when all the steps are performed under the same conditions. If the inorganic film produced by a single pass through the process is not thick enough, all the steps can be repeated as many times as necessary to produce a film of the required thickness. As soon as the desired film thickness is achieved, the film is heated one more time (annealing) to control features such as oxygen stoichiometry, grain size or preferred orientation.

Metal organic decomposition is a very promising method since it has multiple advantages. First of all, it is inexpensive, guarantees highly uniform chemical composition and purity combined with a good chemical stability [19, 20]. Furthermore, it provides a good productivity, since it involves simple processes performed in the air. MOD also allows epitaxial growth of thin (mostly garnet) films on lattice constant mismatching substrates, which is not possible by techniques such as liquid phase. Finally, MOD ensures a possibility of a thin film formation over a large area.

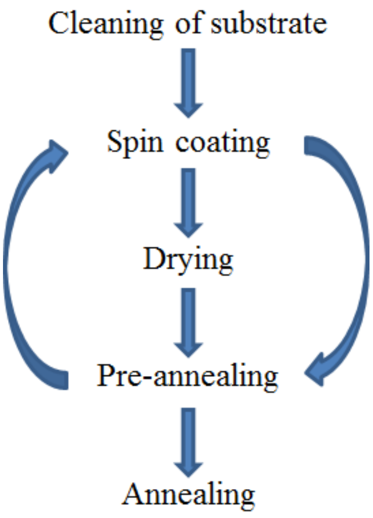

Figure 5.3: Simplified process of MOD

5.4. Pulsed laser deposition

In principle, pulsed laser deposition [21, 22] is a simple technique schematically shown in Figure 5.4. This technique uses high-power pulsed laser beam (typically ~108 Wcm^{-2}) and focuses it into a vacuum chamber to strike a target of a deposited material. This striking event produces plasma plume that augment rapidly away from the target surface. The stroked material is then collected on a substrate where it condenses and grows as a thin film. This process usually occurs in ultra-high vacuum. However, sometimes a background gas, such as oxygen in used when depositing oxides to fully oxygenate the deposited films. In practice, there are multiple variables affecting properties of the film (laser flounce, background gas pressure, substrate temperature etcetera), which optimization requires a lot of time and effort. Application span of this technique is wide. It ranges from the production of superconducting and insulating circuit components to various medical applications. Unfortunately, the fundamental processes occurring during the transfer of material from target to substrate are still not clear and are consequently the focus of much research.

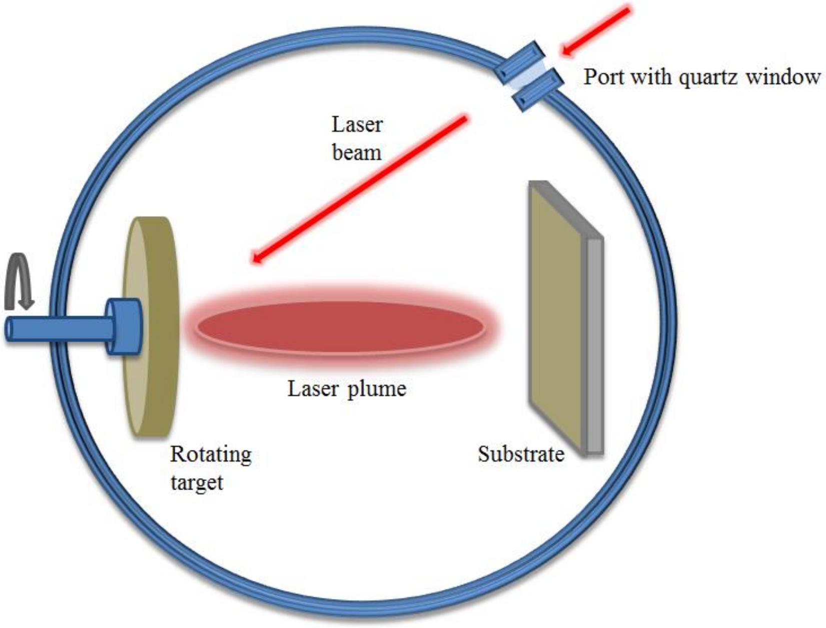

Figure 5.4: Pulsed laser deposition

6. RESULTS

In this part of the thesis, we discussed in detail multiple materials with application potential in several optical and MO devices. We structured this part in sections which are devoted to individual materials: CdZnTe, $Gd_xFe_{(100-x)}$, magnetic garnets and $Ce_{(0.95-x)}Hf_xCo_{0.05}O_{(2-\delta)}$. At the beginning of every section, we discussed the application potential of the material, its properties, samples preparation and samples structure. Afterwards, we focused on SE measurements and analysis. Finally, for magnetic materials, we focused on MO spectroscopy (MOKE and Faraday effect) measurements and analysis.

6.1. CdZnTe

CdZnTe is a very promising crystalline material for high-energy X-ray and gamma ray detectors. This material provides multiple advantages, such as high absorption coefficient, relatively large bandgap (~1.5 eV) at room temperature, and the possibility to achieve resistivity up to ~1010 Ωcm (by compensation of shallow defects). All of these properties combined allow achieving a good signal/noise ratio. On the other hand, surface leakage currents often decrease detector performance. Surface leakage current is strongly dependent on the surface treatment prior to contacts deposition [23]. Moreover, there is also a correlation between material surface treatment and its photoconductivity and resistivity [24]. Surface treatments commonly used for detector fabrication are surface polishing with different size abrasives and chemical etching in different solutions (mostly Br–methanol) [25, 26]. In this section of the thesis, we are therefore focusing not only on the determination of CdZnTe optical functions and but more importantly on CdZnTe surface properties in dependence on the type of the surface treatment. For this purpose we are using SE methods. These methods enable understanding of the correlation between surface treatment and material resistivity and photoconductivity and therefore can be useful for understanding of the variations in the detector performance independent on metallization.

As a sample we used a semi-insulating CdZnTe crystal grown by the vertical-gradient-freeze method with an average Zn concentration of 3.5%. The single-crystalline sample was cut from an ingot by a diamond saw to dimensions 8 x 5 x 2 mm^3. Afterwards we prepared so called contact surfaces (large 8 x 5 mm^2 plane surfaces of the sample) using different treatments. We used polishing by Al_2O_3 with the grain size of 3μm, 1μm, 0.3μm and 0.05μm (POL3, POL1, POL0.3 and POL0.05). Finally, we immersed the sample into a 0.5% Br–methanol chemical solution for 45 s (CHE1) and afterwards into a 1% Br–methanol chemical solution for 180 s (CHE2). Table 6.1.1 shows the summary of used surface preparation treatments. Figure 6.1.1 shows model structure used for SE analysis calculations. In this model we used oxide layer because CdZnTe is easy and fast to oxidize. Surface roughness existence was confirmed by non-contact 3D surface profiler (Zygo, USA).

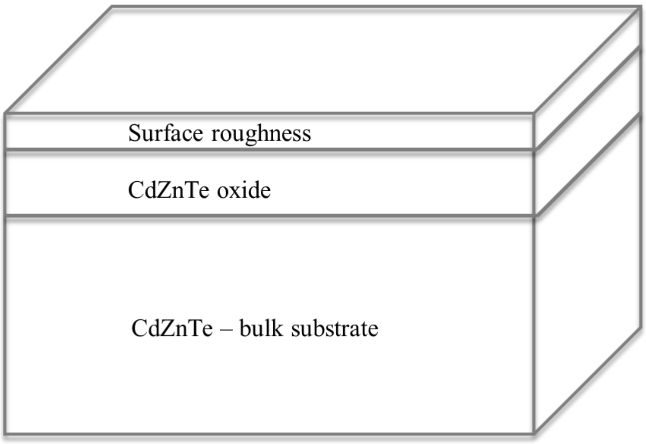

Figure 6.1.1: Model structure of CdZnTe sample used for SE analysis calculations.

Spectroscopic Ellipsometry

We performed SE measurements on a Mueller matrix ellipsometer Woollam RC2. We measured spectral dependence of ellipsometric parameters ψ and Δ in reflection and in the spectral range from 1.25 to 6.5 eV at incident angles 55°, 60° and 65°. We analyzed obtained experimental data using CompleteEase SE software. In order to analyze SE experimental data of studied samples, we fitted CdZnTe and CdZnTe oxide optical functions (diagonal elements of the permittivity tensor ε_{1r} and ε_{1i}) and nominal thicknesses (including surface roughness thickness) to the structural model and experimental data. To ensure Kramers-Kronig consistent results, we parameterized obtained CdZnTe optical functions using four Herzniger-Johs oscillators. We used this type of oscillator due to its ability to describe complicated permittivity spectra shape of crystalline materials. We listed some of used oscillators' parameters in the table 6.1.2. To model CdZnTe oxide optical functions we used EMA method in which we mixed CdZnTe optical functions with void of volume fraction f = 0.26. The EMA method was also used to model surface roughness where we mixed CdZnTe oxide optical functions with void of volume fraction f = 0.5. Figure 6.1.2 shows that used theoretical model describes both: CHE1 and POL3 SE experimental spectra well.

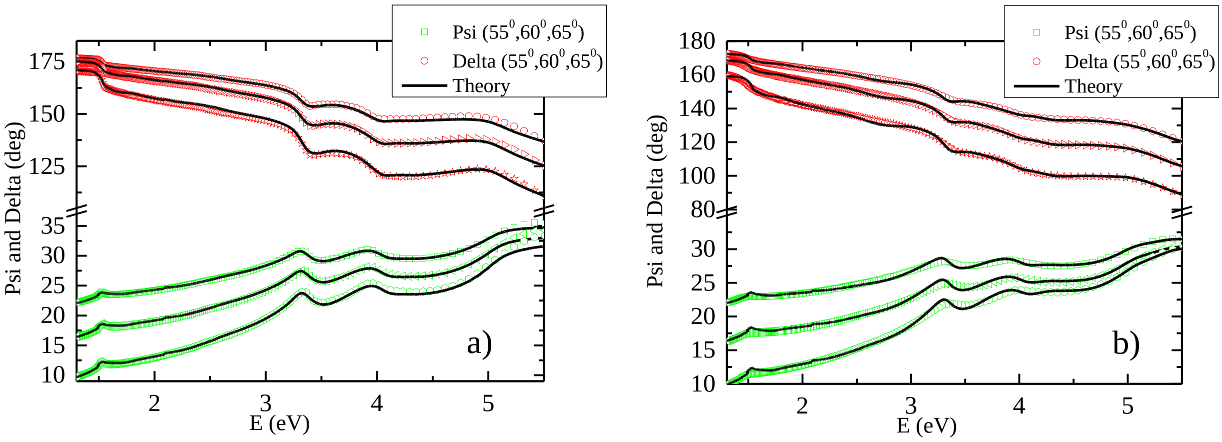

Figure 6.1.2: Measured variable angle SE Psi and Delta spectra of a)CHE1 and b) POL3 samples compared to the theoretical model (black lines).

Figure 6.1.3 shows obtained spectra of the real ε_{1r} and imaginary ε_{1i} part of the CdZnTe permittivity tensor. The real part ε_{1r} is generally decreasing its values with energy while showing three local maxima at 3.2, 3.6 and 4.8 eV. The imaginary part ε_{1i} is generally increasing its values with energy while showing three local maxima at 3.3, 3.9 and 5.2 eV assigned to optical transitions parameterized by Herzinger-Johns oscillators. Moreover, in ε_{1i} spectrum we can observe absorption edge close to 1.5 eV which is in accordance with previous research [27, 28]. We can also observe optical transitions and absorption edge in calculated CdZnTe absorption coefficient spectra shown in Figure 6.1.4. As expected absorption coefficient is increasing its value with energy. All the results correspond well to previously obtained results on CdTe material [29]. We assigned small discrepancies to the fact that in here we are dealing with CdZnTe material and therefore to the influence of Zn.

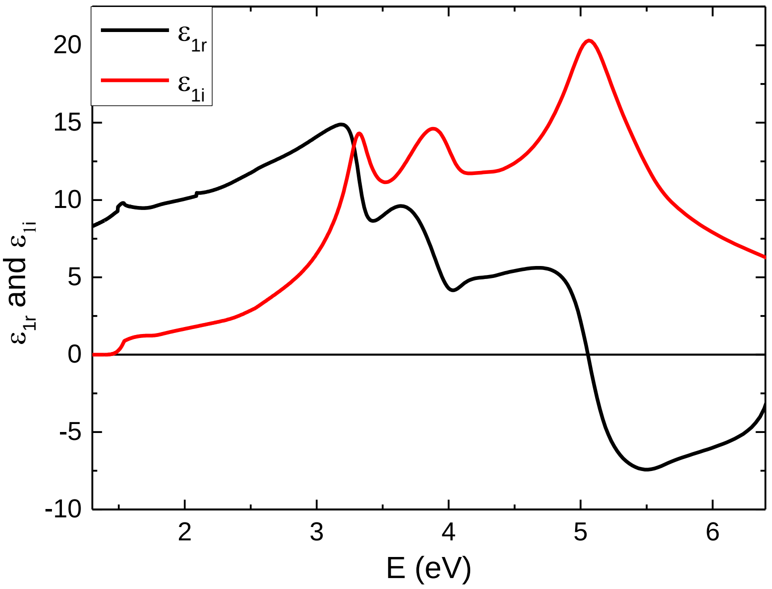

Figure 6.1.3: Real and imaginary parts of diagonal elements of the CdZnTe permittivity tensor.

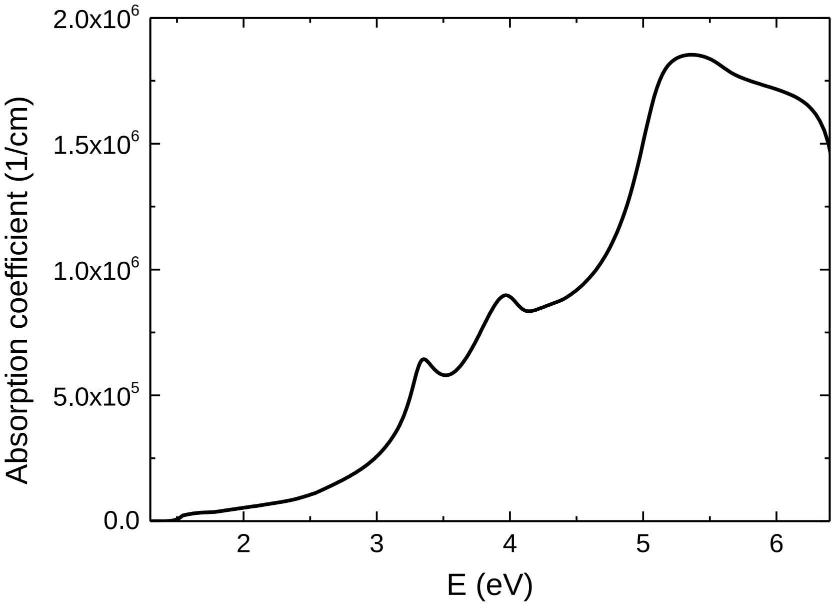

Figure 6.1.4: Calculated absorption coefficient spectra of CdZnTe.

As mentioned previously, in this section we are interested in the CdZnTe surface properties in dependence on the type of surface treatment. For this purpose, we used SE and its sensitivity to the thickness, especially when dealing with nanolayers. We listed fitted CdZnTe oxide and surface roughness thicknesses derived from SE in the table 6.1.1. In here we can see that smaller abrasive size results into thinner GdZnTe oxide layer. Moreover, oxide layer completely diminishes after etching. If one correlates these results with the contactless photoconductivity and resistivity measurements performed by Zazvorka et all. [24], it can be found that CdZnTe oxide layer and also surface roughness influence photoconductivity and resistivity of the sample. They found that with increased surface roughness, resistivity decreases which was assigned to the damaged layer introducing conductive channels into the semi-insulating material. However, on the other hand, thicker oxide layer results into higher resistivity values. Since these two trends act in the opposite direction, one can see maximum in resistivity in dependence on the surface roughness for POL0.3 sample. Photoconductivity is on the other hand negatively influenced for both: increases oxide layer and roughness.

Table 6.1.1: Used surface preparation treatments and thicknesses (CdZnTe oxide layer, surface roughness) derived from SE analysis.

Abbreviation	Method	Abrasive size [30]	CdZnTe oxide thickness [31]	Surface roughness [31]
POL3	Polishing	3	11.6	10.7
POL1	Polishing	1	4.9	0
POL0.3	Polishing	0.3	2	4.5
POL0.05	Polishing	0.05	2.3	0
CHE1	Etching	0.5% Br-methanol/45s	3.9	0.8
CHE2	Etching	1% Br-methanol/180s	0	0.7

Table 6.1.2: Fitted parameters of Herzinger-Johns oscillators used to parameterize optical functions of CdZnTe in the spectral range from 1.25 to 6.4 eV. In here, E stands for central energies of oscillators; Amp represents amplitudes and Br broadenings.

	Herzinger-Johns 1			Herzinger-Johns 2			Herzinger-Johns 3			Herzinger-Johns 4		
	E_0 (eV)	Amp	Br (eV)	E_0 (eV)	Amp	Br (eV)	E_0 (eV)	Amp	Br (eV)	E_0 (eV)	Amp	Br (eV)
CdZnTe	1.54	0.88	0.001	3.3	11	0.04	4.05	6.5	0.06	5.1	19	0.08

6.2. $Gd_xFe_{(100-x)}$

Amorphous ferrimagnetic thin films composed of rare earth and transition metals attracted considerable attention because of their useful technological applications [32-35]. As one of theirs important representative, $Gd_xFe_{(100-x)}$ has significant advantages, such as large magnetization density, and possibility to adjust its compensation temperature, coercive and saturation magnetization by changing the composition [36-38]. Another valuable feature of $Gd_xFe_{(100-x)}$ is that it enables direct access to its spins through the electromagnetic interactions, which makes this material subject of importance for future magnetic recording (such as heat assisted magnetic recording) and information processing technologies. Recent numerical atomic scale modeling simulations of the spin dynamic in Heisenberg $Gd_xFe_{(100-x)}$ ferrimagnet demonstrated that the rapid transfer of energy into the spin system leads to switching of the magnetization within a few ps without necessity of applied magnetic field. The experiment in GdFeCo alloys, which used linearly polarized fs laser pulse to produce the ultra-fast heating, confirmed this prediction [39-41]. Moreover, by using circularly polarized laser pulses, it is possible to take an advantage of the magnetic circular dichroic effect to record a magnetic domain in which the helicity of the laser pulse influences the final magnetization direction [39, 41-43]. These mechanisms allow the $Gd_xFe_{(100-x)}$ magnetic domain light spin manipulation and hence coherent control of the magnetization precession at fluencies as low as 6 $\mu J/cm^2$ [44] and in rates of ps [41, 42, 45]. All of mentioned properties make $Gd_xFe_{(100-x)}$ substantial material for modern micro- and nano-electronic research, where it is often used in domain wall junctions or magneto-optical (MO) memories [32, 34, 35].

Recently, a novel concept of high speed MO spatial light modulator (MO-SLM) for holographic displays based on giant magnetoresistance with $Gd_xFe_{(100-x)}$ as a free layer was proposed [33]. This device is shown in Figure 6.2.1. As one can see, every pixel consists of the ‘free magnetization layer (FL)/ nonmagnetic spacer/ pinned magnetization layer (PL)’ structure. Free layer magnetization is controlled by spin polarized current. When the magnetizations of FL and PL are aligned, the polarization of the light reflected on the structure will rotate to the one direction. When magnetizations of FL and PL head against each other, the polarization of the light reflected on the structure will rotate to the opposite direction. Therefore, in the multi-pixel structure, we can actually create interference pattern crucial for holography, just by using a polarization filter. The main advantage of this approach is the response time in terms of 0.015 µs and pixel size in terms of 10 µm [46].

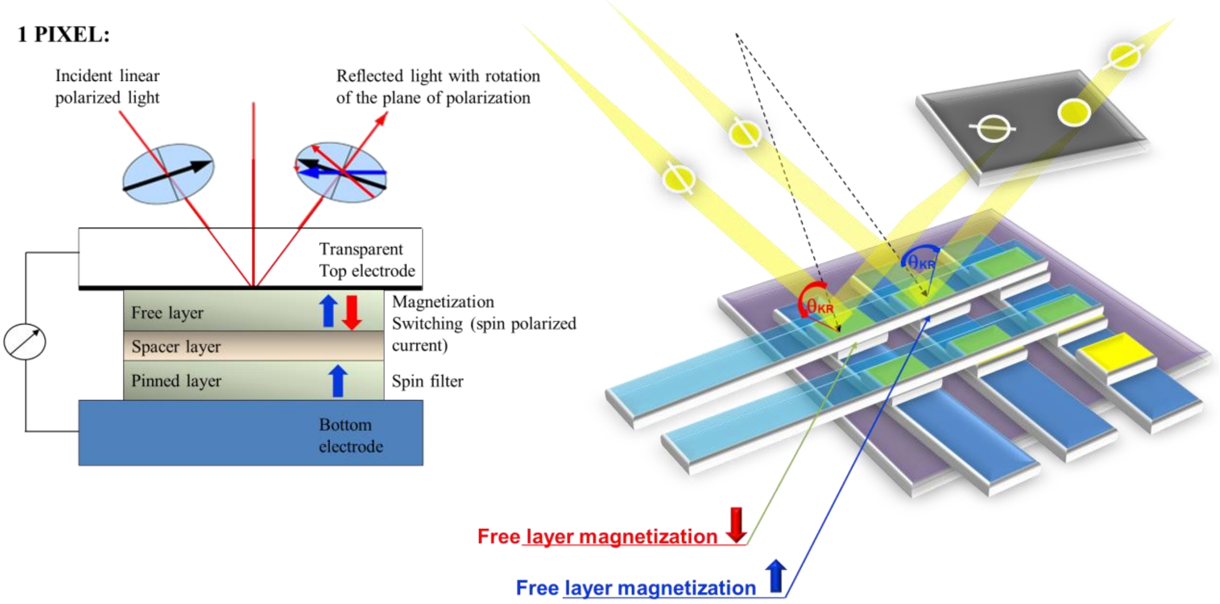

Figure 6.2.1: Concept of high speed MO spatial light modulator for holographic displays based on GMR.

When using $Gd_xFe_{(100-x)}$ for MO-SLM driven by spin transfer torque, it is very important that $Gd_xFe_{(100-x)}$ shows perpendicular anisotropy. This happens when the Fe concentration is about the compensation concentration, which is for this material about 75% [47] (this composition is also often used for MO applications such as MO disk storage [33]). Since in here $Gd_xFe_{(100-x)}$ acts as FL, it is very important to control its composition precisely, because it significantly affects its magnetic switching property. Coercivity shows maxima when the $Gd_xFe_{(100-x)}$ composition is the compensation one, and it gets smaller when the composition becomes Fe rich (compared to the compensation composition). Spin-torque switching current of the spin MO-SLM is significantly reduced with an increase in Fe concentration and it shows very small switching current when composition is slightly Fe richer than the compensation one [46, 48]. Therefore it is meaningful to investigate optical properties of the $Gd_xFe_{(100-x)}$ material around the compensation concentration.

The main purpose of our investigation was the determination of the complete permittivity tensors for $Gd_xFe_{(100-x)}$ thin films with various compositions (x=18.3, 20, 24.7, 26.7). We were interested in the permittivity tensor spectra because it provides a deeper look at optical and MO properties of material. Moreover, the knowledge of the complete tensor allows the theoretical prediction of complex physical properties of complicated multilayered nanostructures containing $Gd_xFe_{(100-x)}$ layer. This is especially useful when designing complicated nanostructured device such as MO-SLM, because it allows proposal of desired structure without necessity of preparing and measuring multiple samples.

In this work is $Gd_xFe_{(100-x)}$ covered by a coating to avoid the oxidation process [49]. However, this fact complicates its analysis. Optical properties of coating materials (here Ru, SiO_2) may slightly differ in dependence on material they are deposited on. The reason behind this behavior is usually the lattice mismatch between the film and substrate that induces strains of various kinds [50-52]. In order to deal with this problem we used 2 different coating materials which allowed more precise determination of $Gd_xFe_{(100-x)}$ permittivity tensors. SE analysis showed very similar optical properties of individual $Gd_xFe_{(100-x)}$ compositions for both coatings, which demonstrated a good stability of $Gd_xFe_{(100-x)}$ layer.

In this section, we used SE at energies from 1.3 to 5.5 eV and MO spectral measurements at energies from 1.5 to 5.5 eV. From SE data, we derived the diagonal permittivity tensor elements ε_{1r} and ε_{1i} spectra of $Gd_xFe_{(100-x)}$ thin films. We examined MO properties by polar MOKE rotation and ellipticity measurements. From these data we determined the spectral dependence of the off-diagonal $Gd_xFe_{(100-x)}$ permittivity tensor elements ε_{2r} and ε_{2i}. We also performed MOKE hysteresis measurements, which demonstrated changes in the magnetization in dependence on $Gd_xFe_{(100-x)}$ composition.

For our samples, we used silicon substrate with thermally oxidized SiO_2 layer. Afterwards, we deposited $Gd_xFe_{(100-x)}$ and Ru coating by direct current sputtering technique in Kr gas of pressure 8.7x10-2 Pa with a deposition rate of 3.6 nm/min. Finally, we deposited SiO_2 coating by ion beam sputtering technique with radio frequency ion source. Theoretical model structures used for SE and MOKE analysis calculations are shown in Figure 6.2.2.

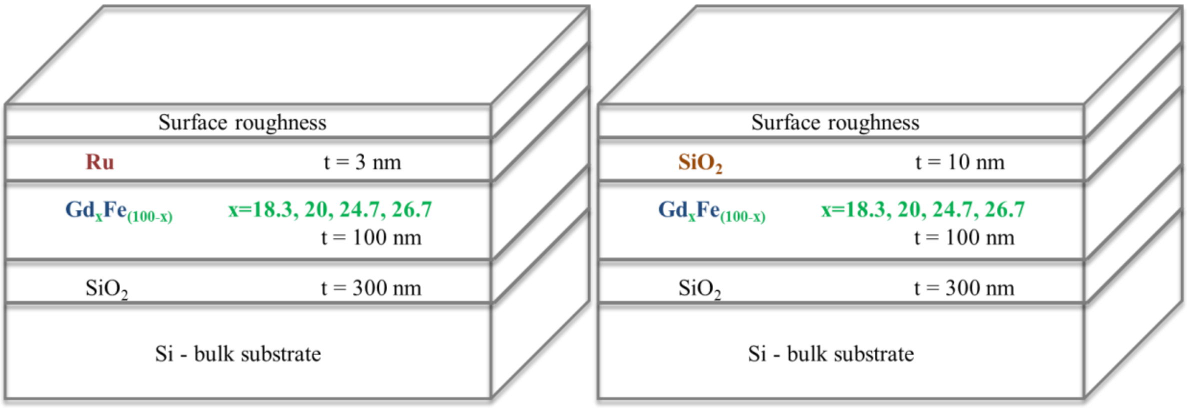

Figure 6.2.2: Model structure of GdFe/Ru and GdFe/SiO_2 samples used for SE and MOKE analysis calculations.

a) Spectroscopic Ellipsometry

We measured ellipsometric Psi and Delta parameters of the reflected light in the spectral range from 1.3 to 5.5 eV for incident angles 55°, 60° and 65°. Obtained experimental data were analyzed using CompleteEase software. In order to analyze SE experimental data of studied samples we fitted $Gd_xFe_{(100-x)}$ optical functions (diagonal elements of the permittivity tensor ε_{1r} and ε_{1i}) and nominal thicknesses to the structural models and experimental data. In order to avoid the false minima result of the fitting process, we used the MSA mode to derive the $Gd_{18.3}Fe_{81.7}$ and $Gd_{24.7}Fe_{75.3}$ optical functions from the experimental data for both coatings simultaneously. In MSA mode, we set $Gd_xFe_{(100-x)}$ (x=18.3 or x=24.7) optical functions as the fit parameter common for both samples. We set optical functions of coating materials and thicknesses as fit parameters varying for each sample independently. Figure 6.2.3 shows that theoretical model describes both: $Gd_{20}Fe_{80}$/Ru and $Gd_{20}Fe_{80}/SiO_2$ SE experimental spectra well.

We parameterized obtained optical functions to ensure Kramers-Kronig consistent results. We used two Lorentz oscillators and one Drude term in the spectral range from 1.5 to 6 eV. We used Lorentz oscillators due to their ability rapidly approach zero beyond the FWHM position and the Drude term to describe the free carrier effect on the dielectric response. We listed parameters of used parameterizations in the table 6.2.1. We determined constants of Si, SiO_2 and Ru from SE measurements on individual samples. We listed derived thicknesses in the table 6.2.2. To confirm thicknesses of $Gd_xFe_{(100-x)}$ layers derived from SE, we also performed XRF measurements. We listed thicknesses of $Gd_xFe_{(100-x)}$ layers derived by XRF in the table 6.2.2. As you can see, values derived from SE and XRF correspond well.

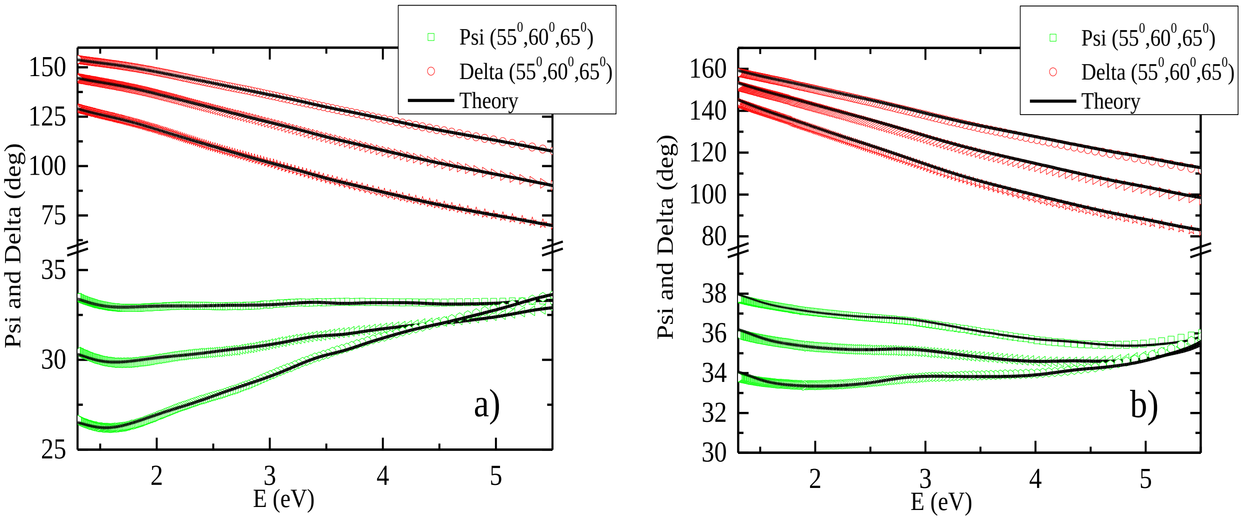

Figure 6.2.3: Measured variable angle SE Psi and Delta spectra of a)Gd20Fe/Ru and b) Gd20Fe/SiO_2 samples compared to the theoretical model .

Table 6.2.1: Fitted parameters of Lorentz oscillators and Drude term used to parameterize optical functions of $Gd_xFe_{(100-x)}$ in the spectral range from 1.5 to 6 eV. In here, E stands for central energies of oscillators; Amp represents amplitudes and Br broadenings. For Drude model, N represents carrier concentration, μ carrier mobility and m* carrier effective mass.

	Lorentz (E = 1.89 eV)		Lorentz (E = 2.57 eV)		Drude term		
	Amp	Br (eV)	Amp	Br (eV)	N (cm^{-3})	M ($cm^2V^{-1}s^{-1}$)	m*
Gd**18.3**Fe	6.66	2.30	1.10	1.09	$1.098*10^{23}$	0.354	0.514
Gd**20.0**Fe	6.23	2.43	1.28	1.43	$1.095*10^{23}$	0.352	0.533
Gd**24.7**Fe	6.04	2.69	1.43	1.84	$1.110*10^{23}$	0.340	0.564
Gd**26.7**Fe	5.82	2.83	1.67	1.99	$1.113*10^{23}$	0.332	0.573

Table 6.2.2: Fitted thicknesses used for model of Gd$_x$Fe$_{(100-x)}$ in SE and XRF in the spectral range from 1.5 to 6 eV. In here, t stands for thickness and r for roughness on top.

	t_{SiO2} (nm) SE	t_{GgFe} (nm) SE	t_{GgFe} (nm) XRF	t_{Ru} (nm) *coating*	t_{SiO2} (nm) *coating*	r (nm) SE
Gd**18.3**Fe/**Ru**	307	131.6	136.9	3.1	--	2
Gd**18.3**Fe/**SiO$_2$**	307	130	136.9	--	11.3	0.3
Gd**20.0**Fe/**Ru**	307	103	99.6	2.9	--	2
Gd**24.7**Fe/**Ru**	307	95	87.7	2.7	--	1.9
Gd**24.7**Fe/**SiO$_2$**	307	87.7	87.7	--	10.5	0.7
Gd**26.7**Fe /**Ru**	307	93.4	93.4	2.2	--	1.9

Figure 6.2.4 shows real parts of the diagonal permittivity tensor elements ε_{1r} and Figure 6.2.5 shows imaginary parts of the diagonal permittivity tensor elements ε_{1i} of the Gd$_x$Fe$_{(100-x)}$ thin films. Figure 6.2.6 shows calculated absorption coefficient spectra. The ε_{1r} spectra are characteristic by one global minimum at 2.9 eV while the ε_{1i} amplitudes decrease their values with increasing energy in the measured spectral range for all the compositions. As expected, absorption coefficient spectra have increasing character with energy. All the spectra show similar behavior to Fe and Gd [53, 54] and also to the results previously reported on Gd$_x$Fe$_{(100-x)}$ films by other groups [37, 55]. The behavior in the spectral range from 1.5 to 3eV, where ε_{1r} decreases its value for higher energies is similar to the behavior of some transitions metals (including Cr, Gd, Ru, Ti [53, 54]). This behavior is usually explained by intra-band transitions, which are for some transition metals not negligible in measured spectral region [54]. Finally, to discuss the Gd substitution effect, we would like to note in here, that higher Gd content decreases both, ε_{1r} and ε_{1i} amplitudes and therefore the refraction index, especially at extreme 2.9 eV. Gd substitution is increasing absorption coefficient of this material bellow 5 eV, however it has the opposite effect above.

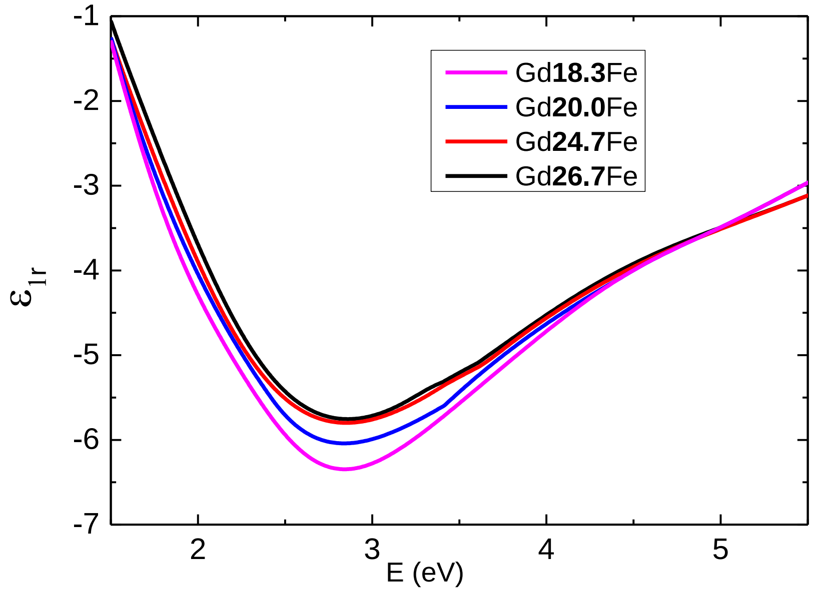

Figure 6.2.4: Real parts of diagonal elements of the permittivity tensor of the $Gd_xFe_{(100-x)}$ thin films.

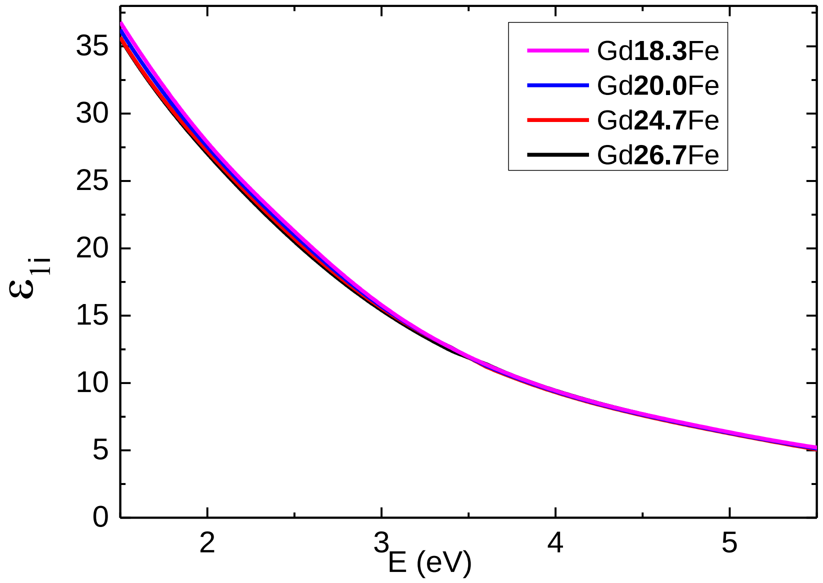

Figure 6.2.5: Imaginary parts of diagonal elements of the permittivity tensor of the $Gd_xFe_{(100-x)}$ thin films.

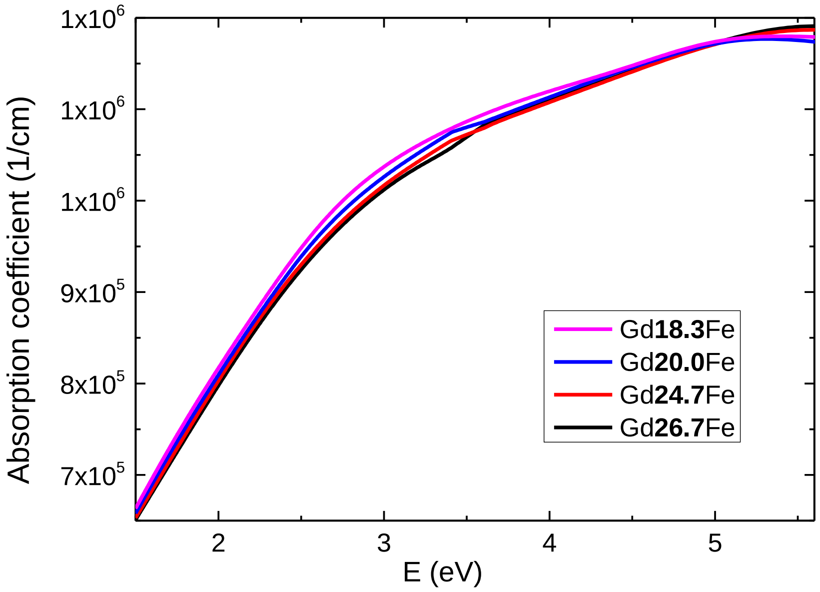

Figure 6.2.6: Calculated absorption coefficients of Gd_xFe_{100-x} thin films.

b) MOKE spectroscopy

We measured MO properties by MOKE spectroscopy. We obtained the MOKE rotation and ellipticity spectra in the polar configuration. We acquired all the spectra at the room temperature for nearly normal light incidence. Applied magnetic field was 1.2 T, which was enough for magnetic saturation of samples. Incident light was s-polarized. We recorded data in the photon energy range from 1.5 to 5.5 eV. We measured MOKE rotation hysteresis loops by differential intensity detection method at 2.38 eV. We performed all measurements in the polar geometry and at the room temperature. Field was ranging from -1.8 T up to 1.8 T, which was far beyond saturation point.

We would like to start this section with polar MOKE hysteresis measurements shown in Figure 6.2.7. First thing to notice is that easy axis of $Gd_xFe_{(100-x)}$ magnetization lies out-of-plane for all the samples. However, when Gd reaches the compensation concentration ($x \approx 25$) the magnetization direction changes to the opposite site. Moreover, the ferrimagnetic nature of $Gd_xFe_{(100-x)}$ causes, that samples Gd20Fe/Ru, Gd18.3Fe/SiO_2 and Gd18.3Fe/SiO_2 have “not squared” shape of hysteresis loops.

The reason is that when being farther from the compensation point, $Gd_xFe_{(100-x)}$ magnetic sub-lattices saturates on different paces [56]. Shapes of all hysteresis loops are therefore characteristic for out-of-plane hysteresis loops of ferrimagnetic materials around the compensation point [56]. Further thing to discuss, is the opposite direction of the magnetization for samples with the Gd concentration x=24.7 (Gd24.7Fe/Ru and Gd24.7Fe/SiO_2). Since this concentration is extremely close to the compensation point, it would be reasonable to assume that the dispersion of the Gd concentration during the film preparation process causes this behavior. However, we believe that in this case (based on experience), coating affects the Gd24.7Fe properties more than Gd concentration dispersion, since SiO_2 may oxidize Gd selectively.

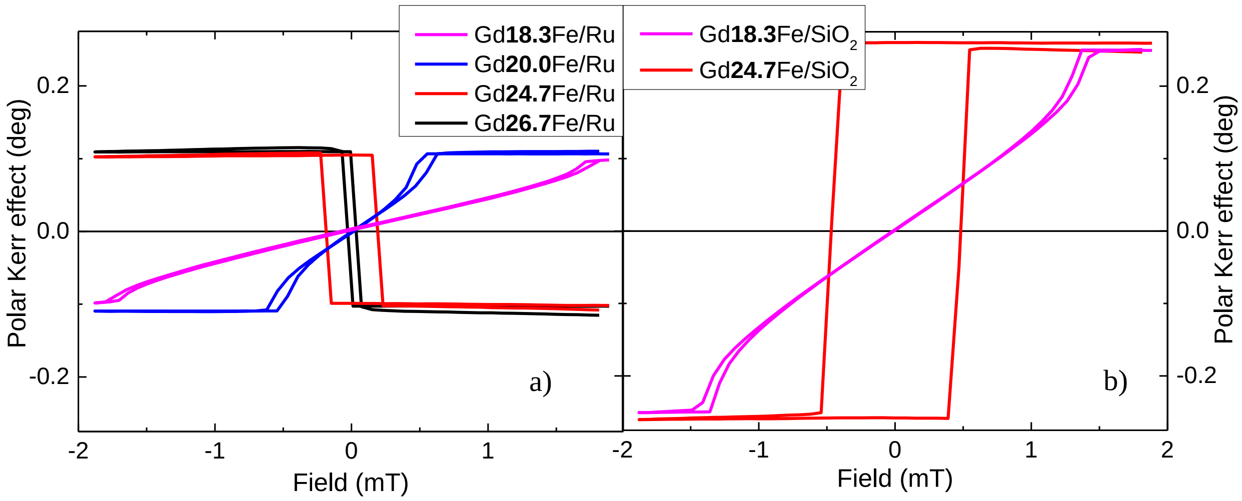

Figure 6.2.7: Hysteresis loops of examined samples with a) Ru and b) SiO_2 coatings at 2.38 eV.

Figure 6.2.8 shows MOKE rotation and Figure 6.2.9 MOKE ellipticity spectra. Firstly, both spectra are characteristic by increasing rotation and ellipticity amplitudes toward to smaller energies. Secondly, samples with SiO2 coating show much higher MO signal than samples with Ru coating (also possible to see from hysteresis loops measurements). We attributed this to multiple reflections in measured energy region for SiO2 coated samples. Furthermore, we can observe that substitution of Gd is increasing amplitudes of MOKE. Moreover, as expected, amplitudes of MOKE rotation and ellipticity changes the sign when Gd reaches the compensation concentration (x ≈ 25) and therefore when magnetization direction changes. All the data correspond with the hysteresis loops measurements.

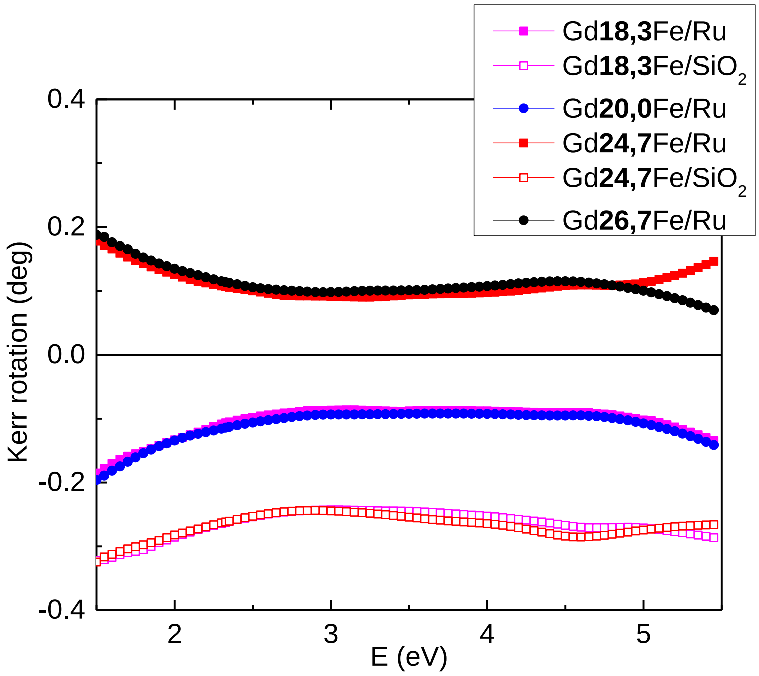

Figure 6.2.8: Polar MOKE rotation spectra of examined $Gd_xFe_{(100-x)}$ samples with Ru and SiO_2 coatings.

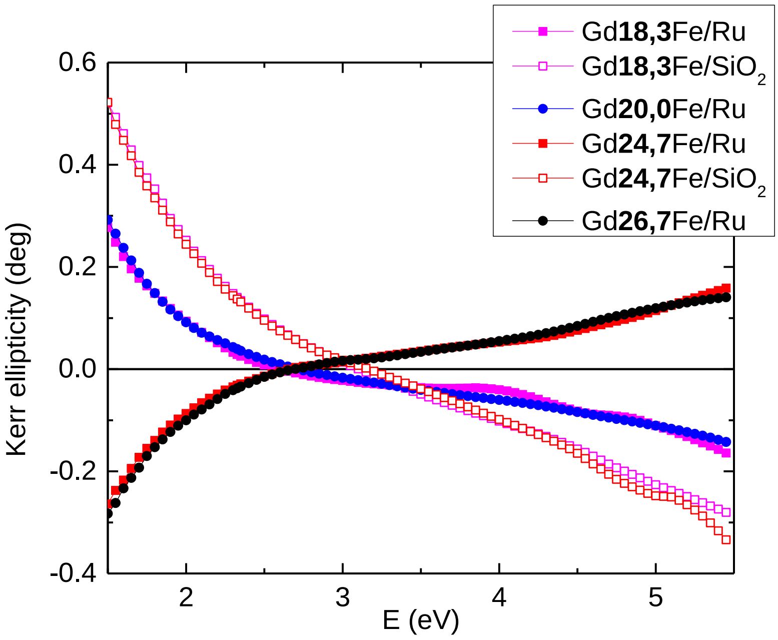

Figure 6.2.9: Polar MOKE ellipticity spectra of examined $Gd_xFe_{(100-x)}$ samples with Ru and SiO_2 coatings.

We used obtained MOKE spectra to calculate the off-diagonal elements of the $Gd_xFe_{(100-x)}$ permittivity tensors. For the off-diagonal elements calculations, we used the diagonal elements of the permittivity tensors and thicknesses determined by SE. Figure 6.2.10 shows calculated real parts of the off-diagonal elements ε_{2r} and Figure 6.2.11 imaginary parts of the off-diagonal elements ε_{2i}. The ε_{2r} spectra are characteristic by one global extreme around 2.5 eV while ε_{2i} amplitudes decrease with energy in the measured spectral range. Amplitudes of $Gd_xFe_{(100-x)}$ off-diagonal permittivity elements spectra are smaller than amplitudes of Fe, which is the most probably caused by the presence of the Gd. To discuss the effect of Gd, it is also important to note, that Gd substitution decreases amplitudes of both, the real and imaginary part of the permittivity tensors. We attributed this to the fact that the magnetic moment of Fe is in this ferrimagnetic alloy stronger than the magnetic moment of Gd.

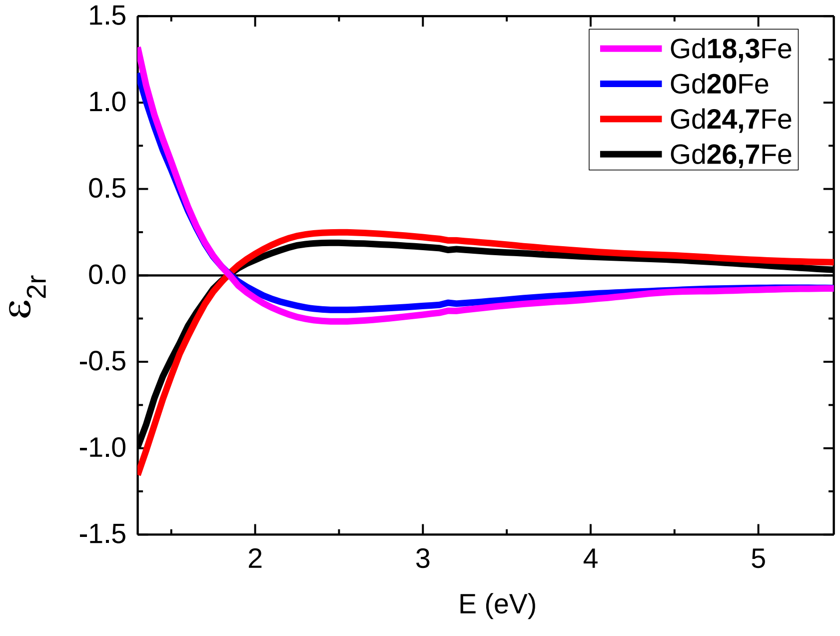

Figure 6.2.10: **Real parts of the off-diagonal elements of the permittivity tensors of $Gd_xFe_{(100-x)}$.**

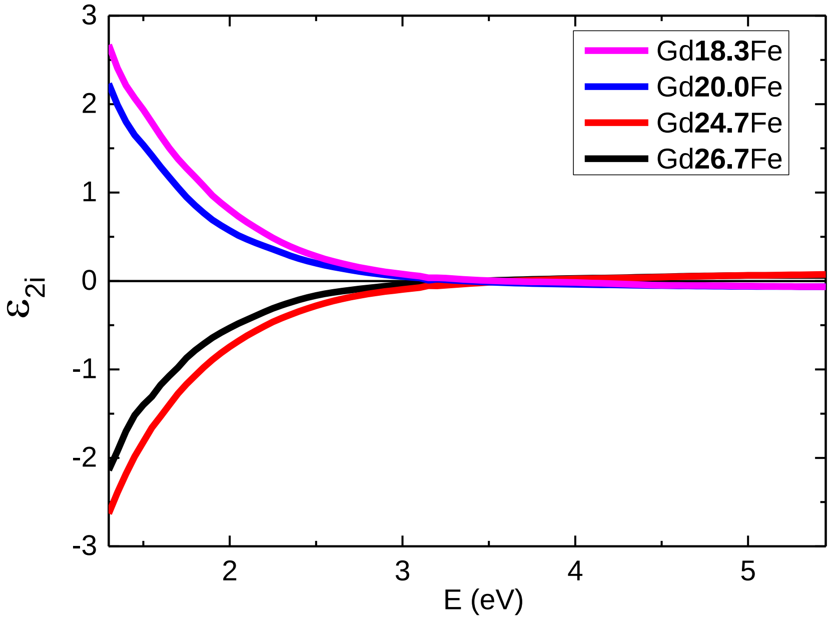

Figure 6.2.11: Imaginary parts of the off-diagonal elements of the permittivity tensors of $Gd_xFe_{(100-x)}$.

We parameterized spectra of the off-diagonal elements of the $Gd_xFe_{(100-x)}$ permittivity tensor in terms of microscopic theory. For this purpose we used one Dia transition term with parameters listed in table 6.2.3 for all compositions. From the data we can see that increased Gd concentration is increasing amplitude of the transition only. From these results one can assume that the MO effect observed in MOKE spectra comes from different probabilities of transition between an orbital singlet ground state and excited state split by the combined effect of spin-orbit coupling and an exchange field and that Gd concentration is decreasing this splitting.

Table 6.2.3: Fitted parameters of Dia and Para transitions used to parameterize off-diagonal elements of the $Gd_xFe_{(100-x)}$ permittivity tensor in the spectral range from 1.5 to 5.5 eV. Here, E_0 stands for central energy of the transition; *Amp* represents amplitude of the transition and Γ_0 is half-width in a half-height of the transition.

	Dia tr. 1		
	E_0 (eV)	Amp	Γ_0 (eV)
Gd18.3Fe	1	1.7	0.8
Gd20.0Fe	1	1.9	0.8
Gd24.7Fe	1	2.2	0.8
Gd26.7Fe	1	2.4	0.8

6.3. Magnetic garnets

Magnetic garnets are crystalline materials with a common structure shown in Figure 6.3.1 and described by a general formula $\{A^{3+}\}_3[B^{3+}]_2(C^{3+})_3O_{12}$. In this formula, A stands for doubly positively charged metal ion (Y, Nd, Yb, Lu) surrounded by 8 oxygen ions. B stands for metal ions with three or four positive charges (Fe, Bi, Ga, Al), surrounded by 6 oxygen ions and C for mostly ions with 4 negative charges (Fe, Bi, Ga, Al, surrounded by 4 oxygen ions [38].

These complex materials have recently attracted a considerable attention as they have high application potential. This is manly given by several magneto-electric, spintronic and MO phenomena, such as spin Seebeck effect [57], spin Hall magneto-resistance [58] as well as high MOKE and Faraday effect in the visible-light region. In this section we focus on bismuth substituted yttrium iron garnets $Y_{3-x}Bi_xFe_5O_{12}$ (Bix:YIGs); as well as on bismuth and gallium substituted neodymium iron garnets $Nd_2BiFe_{(5-x)}Ga_xO_{12}$ (Bi1:NIGxGs) and $Nd_{0.5}Bi_{2.5}Fe_{(5-x)}Ga_xO_{12}$ (Bi2.5:NIGxGs). Both of these materials exhibit strong spin-orbit coupling enhanced by 6p orbitals of Bi. Furthermore, Bi1:NIGxGs and Bi2.5:NIGxGs exhibit strong out-of-plane magnetic anisotropy achieved by Ga substitution and crystal orientation (111) of the GGG substrate. Currently, people use various techniques to grow magnetic garnet thin films of high optical and MO quality [31, 59-71]. As explained in section 5.3, MOD has demonstrated to be a very promising method for this type of material.

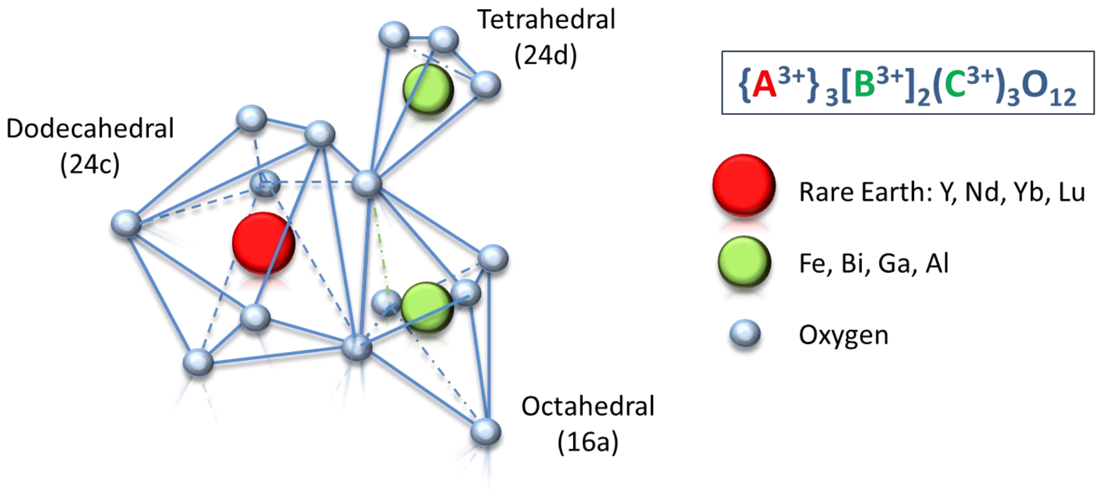

Figure 6.3.1: Atomic structure common to magnetic garnets.

All of mentioned properties combined make studied garnets suitable for applications such as magnetic recording or non-reciprocal photonic devices (including optical isolators and circulators). Moreover, garnets are much desired material for various MO visualizers and microscopes [72, 73]. Figure 6.3.2 shows MOKE microscope which images magnetic domains on the surface of magnetic materials. In this device, polarized light reflects on the magnetic sample (for example magnetic credit card) and passes through an analyzer (polarizing filter), before going through a regular optical microscope. When the polarized light reflects on the magnetic sample, MOKE causes different changes in the light polarization for differently oriented magnetic domains. These polarization changes are afterwards converted by the analyzer into the light intensity changes, which are visible. However, magnetic domains are not easily to observe for materials that exhibit small MO effects or materials that are covered by a non-transparent protecting layer (plastic layer in cards). Therefore, to make magnetic domains visible, MOKE microscope uses transparent MO imaging plate that exhibits huge MO effect (garnet film). This MO plate is put on the sample and it copies its magnetic field. Therefore, we do not observe MO effect on examined sample, but on MO plate with identical magnetic domains shape as the sample.

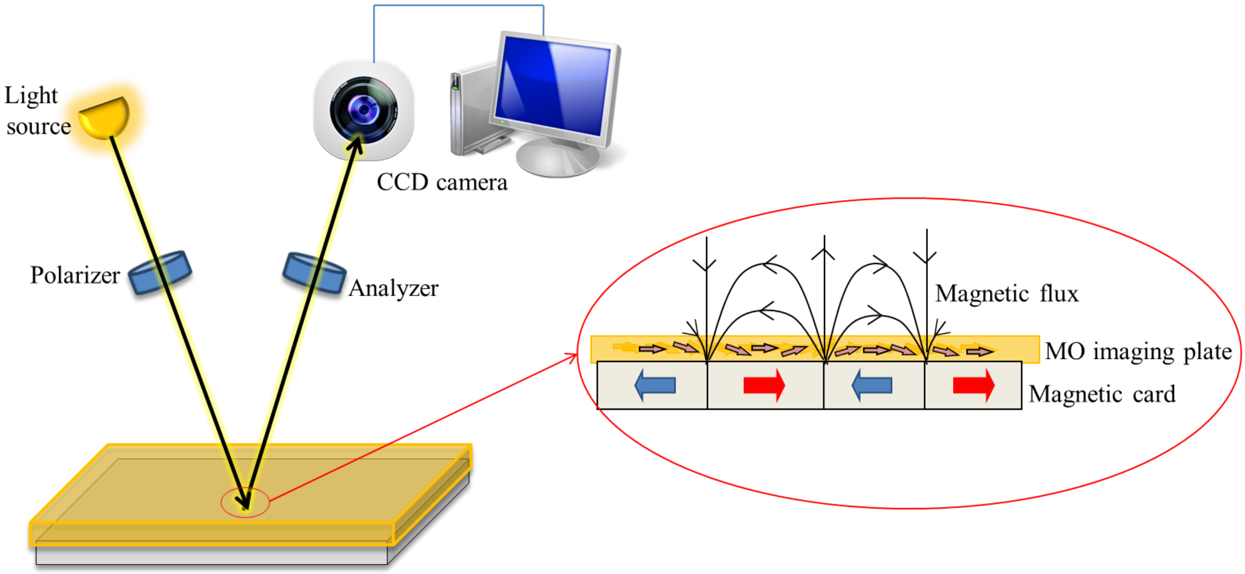

Figure 6.3.2: MOKE microscope principle and magnetic response of MO imaging plate to a material with magnetic domains.

6.3.1 $Y_{3-x}Bi_xFe_5O_{12}$

In this sub-section, we focused on the determination of complete permittivity tensors of Bix:YIGs thin films with various Bi concentrations. We used optical and MO spectral measurements at energies from 1.5 to 5 eV. We compared obtained results to the properties of investigated Bix:YIGs thin films prepared by MOD to properties of bulk-like Bix:YIGs with small Bi concentrations prepared by epitaxial growth [8, 74]. We examined optical properties by SE supported by transmission intensity measurements. From these data we derived the diagonal permittivity tensor elements. We examined MO properties by spectroscopic MOKE and Faraday effect measurements and analysis. Using a combination of the SE and MO measurements we determined the spectral dependence of off-diagonal permittivity tensor elements. Finally, we parameterized obtained results in terms of microscopic theory which relates permittivity tensor spectra to energy-level splitting and transition probabilities.

We focused on $Y_{3-x}Bi_xFe_5O_{12}$ thin films (x= 1.5, 2, 2.5, 3) prepared on $Gd_3Ga_5O_{12}$ (GGG) (100) substrates. We listed compositions of garnet films in the table 6.3.1. The thin films were prepared by MOD method. MOD liquids for garnet films consisted of solutions made of Bi, Y, and Fe carboxylates. The total concentration of carboxylates was 3 – 4% [20, 75]. We prepared MOD liquids by mixing each solution to obtain desired chemical compositions. We spin-coated MOD liquids on GGG(100) substrates using 3000 rpm for 60 s. We followed this process by drying at 100 °C for 30 minutes using a hot-plate. Afterwards, we pre-annealed samples at 450 °C for 30 minutes in order to decompose organic materials and obtain amorphous oxide films. We repeated procedure from spin coating to pre-annealing four or five times in order to obtain appropriate thicknesses. Nominal thicknesses of studied garnet films were 160 and 200 nm (see table 6.3.1). We determined nominal thicknesses from the number of MOD cycles calibrated by X-ray measurements. Finally, we annealed samples for the crystallization in a furnace using 700 °C for 3 hours. We performed all thermal treatments in the air. For further information on garnet films prepared by MOD see Ref. [19]. Figure 6.3.3 shows theoretical model structure of Bix:YIGs samples used for SE, MOKE and Faraday effect analyses.

Table 6.3.1: Compositions and nominal thicknesses of examined garnet films.

Film composition	Indication in Figures and text	Nominal thickness (nm)
$Bi_3Fe_5O_{12}$	Bi3IG	200
$Y_{0.5}Bi_{2.5}Fe_5O_{12}$	Bi2.5YIG	160
$Y_1Bi_2Fe_5O_{12}$	Bi2YIG	200
$Y_{1.5}Bi_{1.5}Fe_5O_{12}$	Bi1.5YIG	200

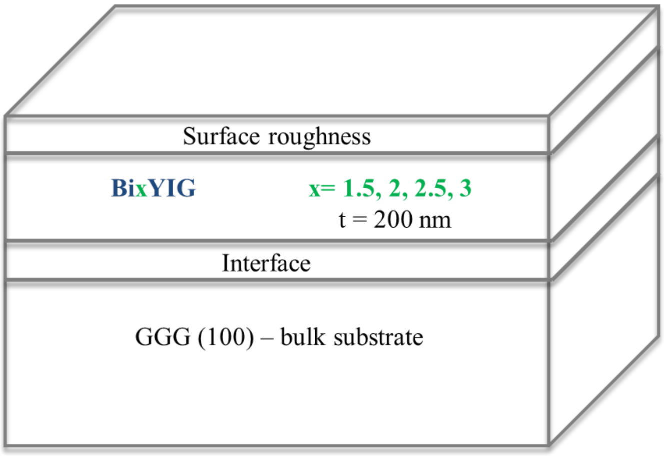

Figure 6.3.3: Model structure of Bix:YIGs samples used for SE, MOKE and Faraday analysis calculations.

a) Spectroscopic Ellipsometry

We performed SE measurements on a Mueller matrix ellipsometer Woollam RC2. We measured spectral dependence of ellipsometric parameters ψ and Δ in reflection and at incident angles 55°, 60° and 65°. We used the same equipment to measure the transmission spectra at the incidence angle 0°. All measurements were performed in the spectral range from 1.5 to 6.5 eV. We analyzed SE experimental data using a CompleteEase software provided by Woollam Co.. We used MSA mode to obtain optical functions spectra (diagonal elements of the permittivity tensor ε_{1r} and ε_{1i}) of GGG and Bix:YIGs materials. In MSA mode, we combined ellipsometric and transmission measurements. We used transmission spectra because of the strong interference observed in ψ and Δ in the transparent spectra region bellow 2.5 eV. We fitted the SE and transmission experimental data using model structure shown in Figure 6.3.3. Figure 6.3.4 shows that theoretical model describes both: SE and transmission experimental spectra well. To ensure Kramers-Kronig consistent results we parameterized obtained optical functions. We parameterized optical functions of GGG substrate (Figure 6.3.5) by one Tauc-Lorentz oscillator in whole measured spectral range. We parameterized calculated optical functions of Bix:YIGs by three Gaussian oscillators (especially in the spectral range 3-5.5 eV) and one general Herzinger-Johns oscillator (especially bellow 3 eV). Since substrates were transparent and both-side polished, we considered back reflections in the SE analysis. We fitted all thicknesses (including roughness and interface layer) by the CompleteEase software and subsequently used them in MOKE and Faraday spectra analysis. Table 6.3.2 shows some parameters of used oscillators. Table 6.3.3 shows fitted thicknesses.

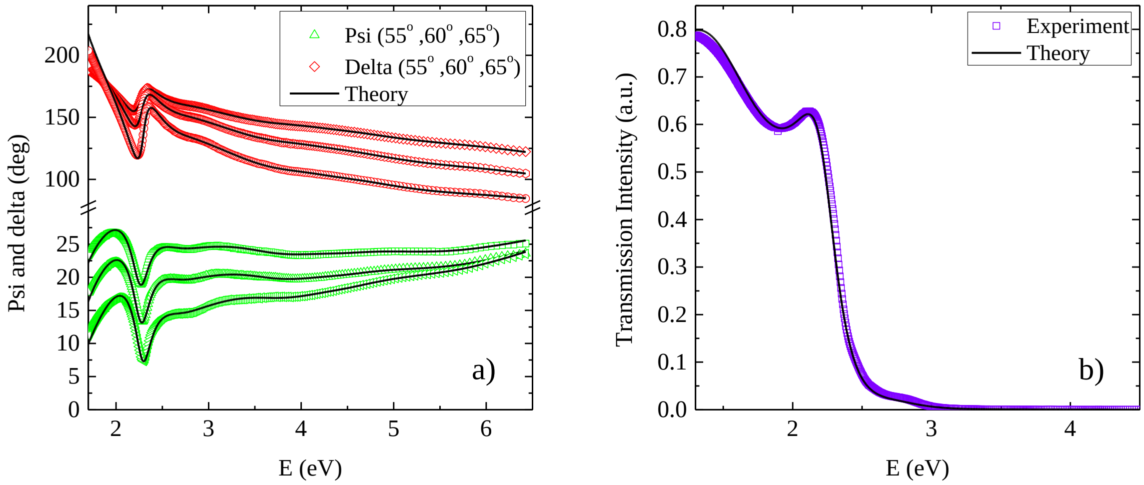

Figure 6.3.4: Experimental data for Bi3YIG layer on GGG substrate compared to the theoretical model. a) Variable angle Psi and Delta SE data. b) Measured transmission intensity spectra.

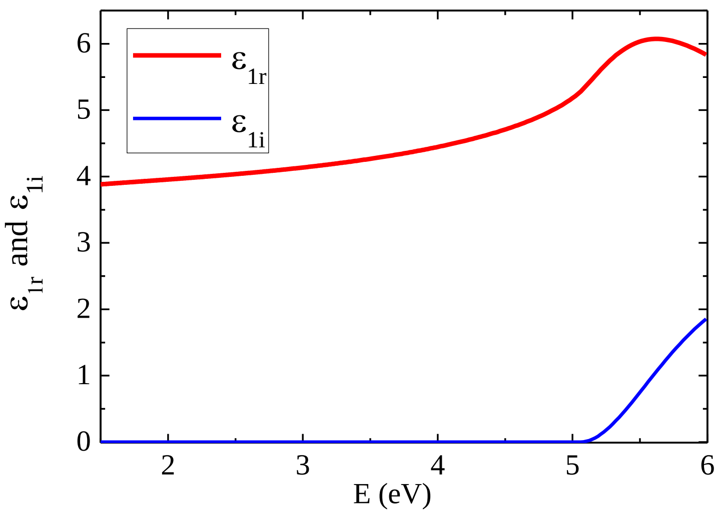

Figure 6.3.5: Spectral dependence of diagonal elements ε_{1r} and ε_{1i} of the GGG (100) substrate permittivity tensor.

Table 6.3.2: Fitted parameters of Gaussian and Herzinger-Johns functions used to parameterize optical functions of Bix:YIGs layers on GGG substrates in the spectral range 1.5 - 6.5 eV. Here, E_0 stands for central energy of the function; Amp represents amplitude of the function and Br its broadening.

	Gaussian 1			Gaussian 2			Gaussian 3			Herzinger-Johns	
	E_0 (eV)	Amp	Br (eV)	E_0 (eV)	Amp	Br (eV)	E_0 (eV)	Amp	Br (eV)	E_0 (eV)	Amp
Bi3IG	3.27	1.64	0.81	4.36	3.4	1.65	6.27	5.05	3.09	2.60	2.33
Bi2.5YIG	3.2	2.7	1.15	4.33	2.29	1.64	6.51	4.26	3.87	2.49	2.40
Bi2YIG	3.04	1.15	0.77	4.25	1.56	1.68	6.36	2.98	2.37	2.53	1.86
Bi1.5YIG	2.71	0.83	0.46	4.23	0.99	2.19	7.31	2.13	4.18	2.89	1.46

Table 6.3.3: Fitted thicknesses and volume fractions used for model of Bix:YIGs layers on GGG substrate in the spectral range 1.5 - 6.5 eV. Here, $T_{Bi:YIG}$ stands for Bi:YIG film thickness; R_{rough} represents film roughness with volume fractions f_{rough}; R_{interf} represents thickness of film/GGG interface with volume fractions $f_{interf.}$

	$T_{Bi:YIG}$ (nm)	R_{rough} (nm)	f_{rough}	R_{interf} (nm)	f_{interf}
Bi3IG	177	7	0.5	4	0.5
Bi2.5YIG	132	5	0.4	2	0.5
Bi2YIG	165	12	0.6	3	0.5
Bi1.5YIG	175	12	0.5	4	0.5

We performed transmission electron microscopy (TEM) measurement on Bi2.5YIG sample. We did this measurement to observe the film quality and also to confirm thicknesses derived from SE. Figure 6.3.6 shows results of the TEM measurement. This measurement confirmed that the film was uniform and epitaxially grown on GGG. (This was expected since X-ray diffraction data of previously grown Bix:YIGs in our laboratory also revealed garnet structure [76].) TEM also revealed that the film thickness was around 132 nm, which is almost 30 nm less than the nominal thickness. Moreover, we can observe interfacial layer in the form of contrast layer between GGG and Bi2.5YIG. These observations are in a very good agreement with the SE analysis results (Table 6.3.3). Finally, we performed AFM roughness measurement on Bi1.5YIG sample. We did this measurement to verify relatively high roughness derived from SE. This measurement revealed roughness 11 nm which is in a good agreement with SE result.

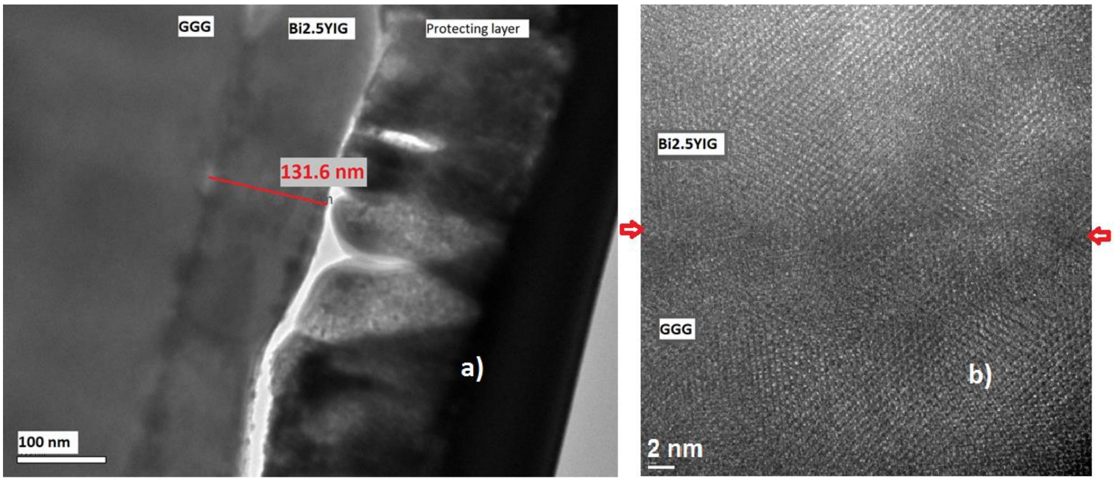

Figure 6.3.6: a) TEM picture of the Bi2.5YIG sample. b) TEM picture of the interface between GGG and Bi2.5YIG layer.

Figures 6.3.7 and 6.3.8 shows spectra of calculated optical functions ε_{1r} and ε_{1i} for all Bix:YIG samples. In the case of ε_{1r} we observed one global maximum around 2.4 eV and local maxima around 3.2 and 4.4 eV. We also observed optical transitions around 2.5, 3.2 and 4.4 eV. The absorption edge near 2.1 eV was clearly visible. Bi3YIG and Bi2.5YIG spectra have in the UV region similar shape. This shape is however different from Bi2YIG and Bi1.5YIG spectra. This observation corresponds to the off-diagonal elements of the permittivity tensor spectra discussed later in this section, where we observe a bigger change in absorption between Bi2YIG and Bi2.5YIG samples. All spectra clearly demonstrated that the bismuth substitution increases amplitudes of ε_{1r} and ε_{1i} in the measured spectral range.

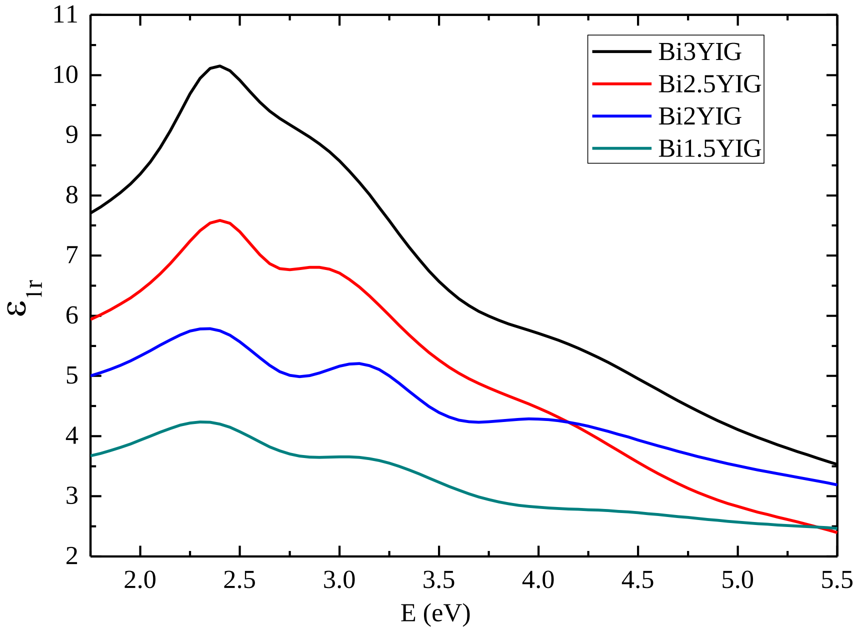

Figure 6.3.7: Real parts of diagonal elements of the permittivity tensor of Bix:YIGs.

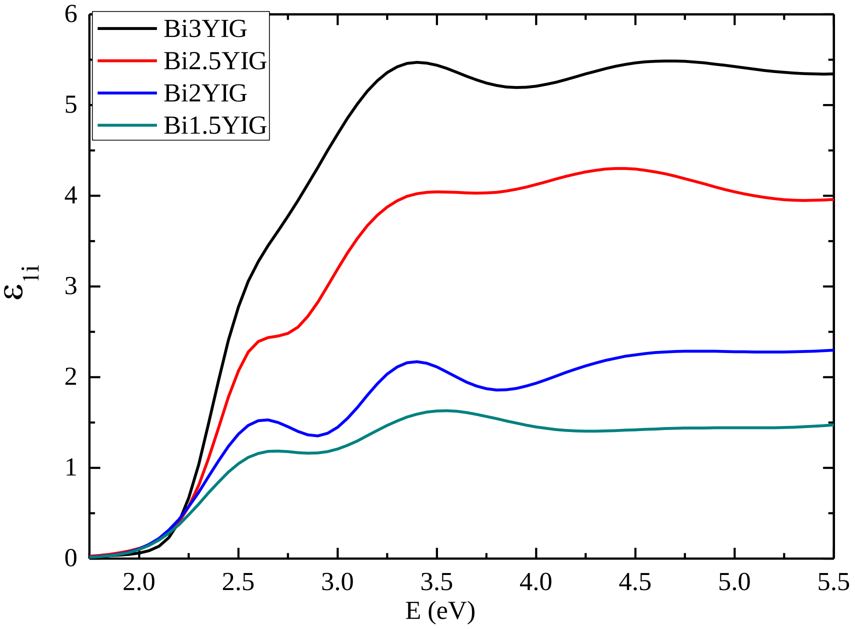

Figure 6.3.8: Imaginary parts of diagonal elements of the permittivity tensor of Bix:YIGs.

When we compare our results to the results previously reported on bulk-like films [8], we can notice smaller ε_{1i} amplitude and an absorption edge shift from 2.5 to 2.2 eV. However, similar measurements performed on thin single crystal Bix:YIGs films show absorption data similar to our results [30, 77, 78]. Therefore we atributed this disprepancy to the difference between properties of thin and bulk-like films. Previous investigations [79-83] demonstrated that properties of ultra-thin films may significantly differ from properties of thicker films. Difference is ussually caused either by materials' inhomogeneities or, as the thickness of the films decreases, by the increasing influence of surface and interface defective layers (in here modeled by EMA) [81, 82, 84].

b) MOKE and Faraday effect spectroscopy

We measured Bix:YIGs MO properties by MOKE and MO Faraday effect spectroscopy. We measured MOKE rotation and ellipticity spectra in the polar configuration. We acquired the spectra at room temperature and at nearly normal light incidence. Applied magnetic field was 1.2 T which was enough for samples saturation. We used p-polarized light. We recorded data in the photon energy range from 1.4 to 5 eV. Faraday rotation and ellipticity spectra were acquired at room temperature using magnetic field 665 mT, which was enough for samples saturation. We recorded Faraday experimental spectra in the photon energy range from 1.4 to 4 eV. Faraday hysteresis loops were measured at 3 eV.

Figure 6.3.9 shows measured MOKE rotation spectra. Figure 6.3.10 shows measured MOKE ellipticity spectra. We observed MOKE rotation maxima around 3.4 and 4 eV and MOKE ellipticity maxima near 3.3 and 4.4 eV. These values are characteristic for Bix:YIGs MOKE spectra [8, 74]. Furthermore, we observed strong MO interference in the form of strong oscillations in the spectral range bellow 3 eV. Since our samples had different thicknesses, we observed different interference patterns for each of them. Spectra clearly demonstrated that bismuth substitution increases amplitudes of MOKE rotation and ellipticity effectively in the measured spectral range.

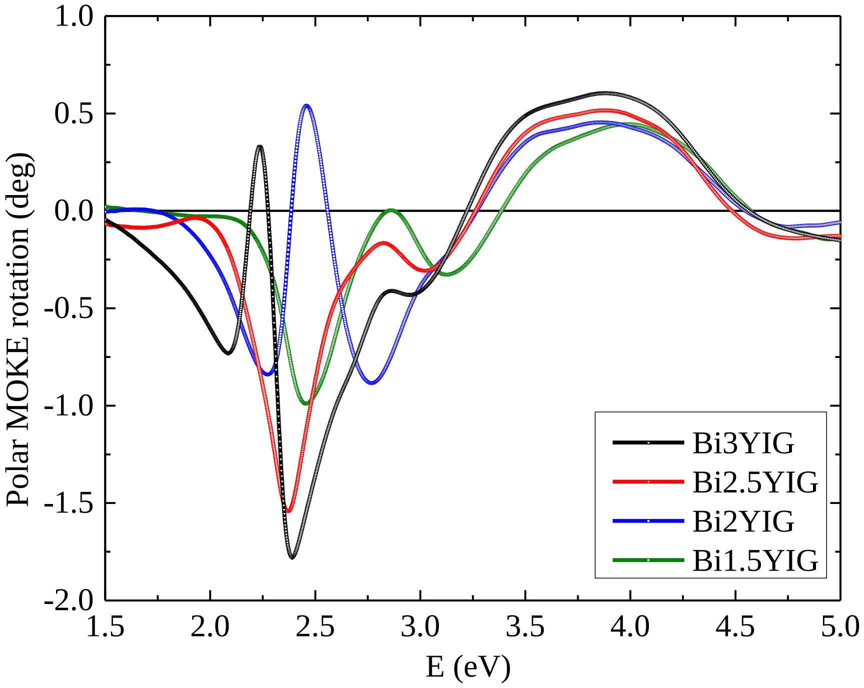

Figure 6.3.9: Polar MOKE rotation spectra of Bix:YIGs on GGG substrates.

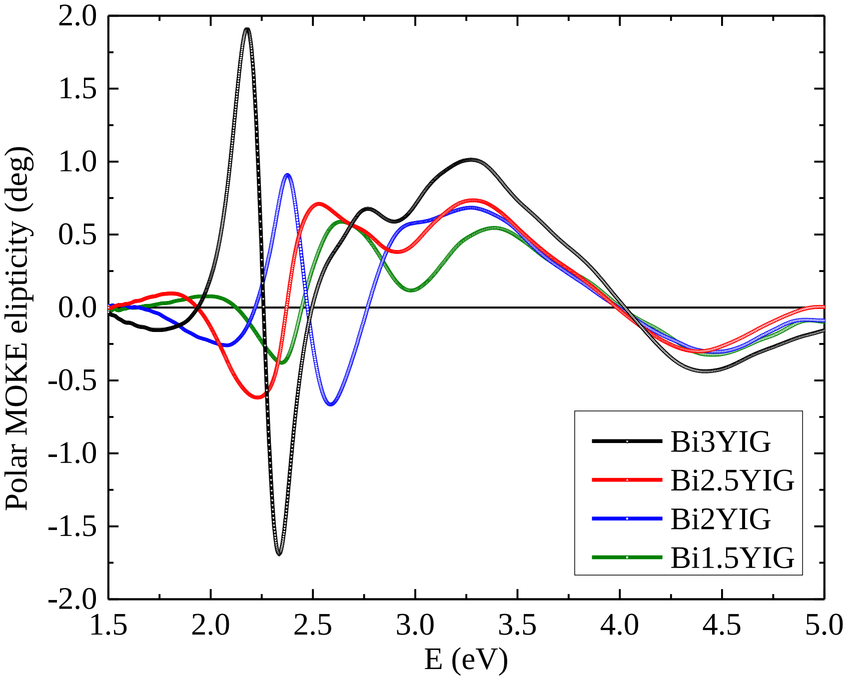

Figure 6.3.10: Polar MOKE ellipticity spectra of Bix:YIGs on GGG substrates.

Figure 6.3.11 shows measured MO Faraday rotation spectra. Figure 6.3.12 shows measured MO Faraday ellipticity spectra. Experimental data were corrected for the rotation from the substrate. We observed Faraday rotation minima near 2.4 eV and two maxima near 2.7 and 3.2 eV. Faraday ellipticity showed maxima at 2.7 and minima at 3.3 eV. As expected, spectra demonstrated that bismuth substitution leads to the enhancement of the MO Faraday rotation near to 2.4, 2.7 and 3.2 eV and ellipticity near 2.7 eV. We demonstrated Faraday rotation angle enhancement by Faraday hysteresis loop measurements shown in Figure 6.3.13.

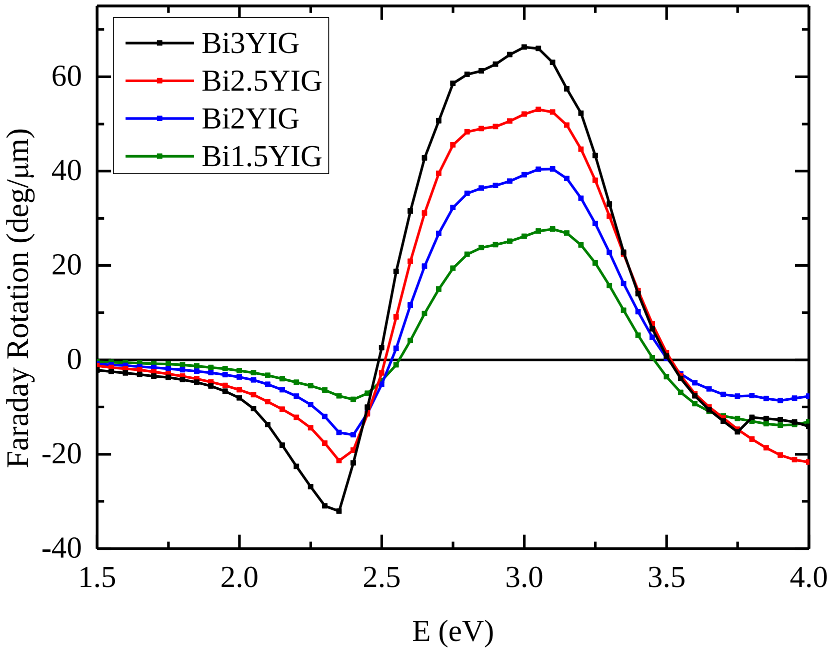

Figure 6.3.11: Faraday effect rotation spectra of Bix:YIGs on GGG substrates.

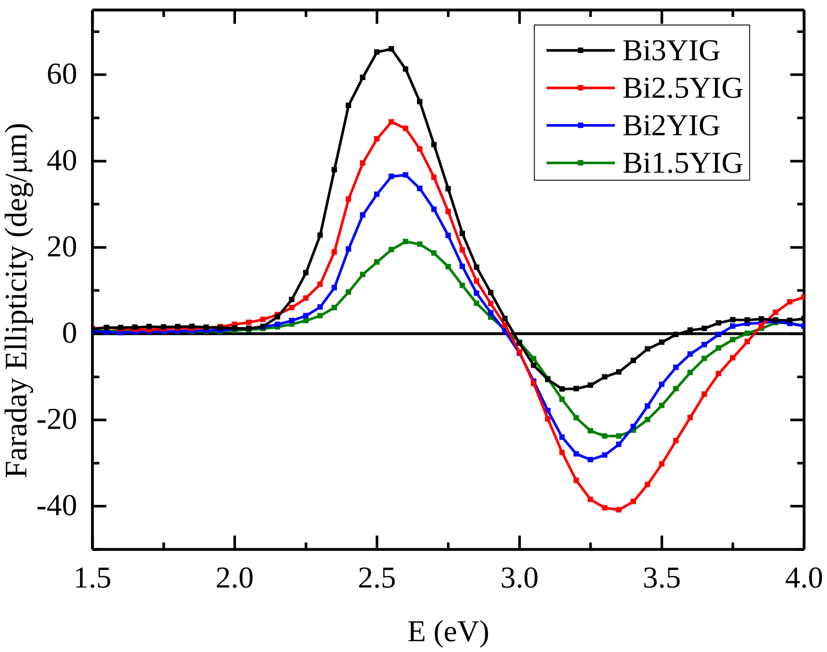

Figure 6.3.12: Faraday effect ellipticity spectra of Bix:YIGs on GGG substrates.

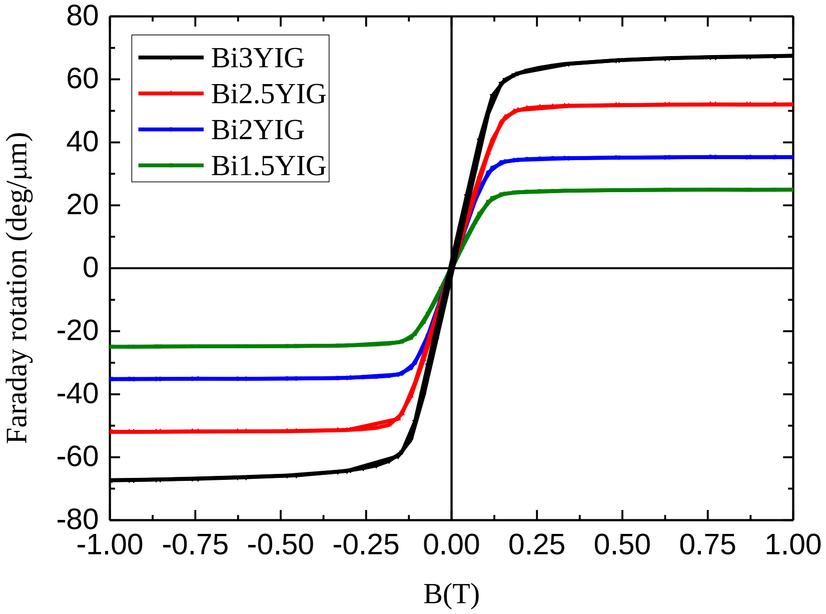

Figure 6.3.13: Faraday effect rotation hysteresis loops of Bix:YIGs on GGG substrates.

We calculated the off-diagonal elements of the permittivity tensor ε_{2r} and ε_{2i} from MOKE and Faraday effect spectra. We performed calculations using Yeh's 4x4 matrix formalism and diagonal elements of the permittivity tensor determined by SE. As mentioned previously, there was strong MO interference bellow 3 eV in MOKE spectra. Therefore, we used MO Faraday effect spectra in the spectral range from 1.5 to 3 eV and MOKE spectra in the spectral range from 3 to 5 eV. Figure 6.3.14 shows the real part of off-diagonal permittivity tensor elements ε_{2r} spectra. We observed sharp global maxima at 2.4 eV and local maxima at 4.2 eV. Minima around 2.7 eV and 3.1 eV were also observed, especially for higher Bi substitutions. As expected, bismuth increases ε_{2r} amplitudes at extremes 2.4, 2.7 and 3.1 significantly.

Figure 6.3.15 shows the imaginary part of off-diagonal permittivity tensor elements ε_{2i} spectra. We observed clear maxima at 2.5 and 4.5 eV and one minimum near 3.4 eV. Spectra demonstrated that bismuth substitution increases amplitudes of ε_{2i}, especially at extremes 2.3, 3.4 and 4.5.

We parameterized spectra of the off-diagonal elements of the Bix:YIGs permittivity tensors ε_{2r} and ε_{2i} in terms of microscopic theory. For this purpose we used two Para transition terms at 2.4 and 3.1 eV and three Dia transition terms at 0.5, 2.5, 3.3 and 4.45-4.65 eV. We used the Dia transition at 0.5 eV only to model the effect of the transitions outside of the measure spectral range. Therefore, we do not attribute it any physical meaning. We listed some of used parameters in table 6.3.4. From these data, we can see that Bi substitution increases amplitudes almost of all listed transitions. Moreover, it lowers energy of Dia transition at 4.65 eV which most likely exist due to charge transfers from oxygen to octahedral Fe [8]. We associated Dia transitions at 2.5 eV and 3.3 eV, which are the strongest, with transitions t2(Fe3+) → t2g(Fe2+) and eg(Fe3+) → e(Fe2+). These transitions are mainly responsible for the remarkable increase of the Faraday rotation in the visible and near infrared region. Since Bi is substituted per Y and not for Fe, positive impact of Bi on these transitions have been previously explained by increase in super-exchange interaction caused by enhancement of electronic exchange [85]. This enhancement is the most probably facilitated by mixing 6p orbitals of Bi with 2p orbitals of Oxygen and 3d orbitals of iron which leads to considering of Bi ion as a magnetic ion [8, 85, 86]. Maxima at

2.4 eV are mainly created by the overlap of secondary negative peaks of these two dominant Dia transitions [8].

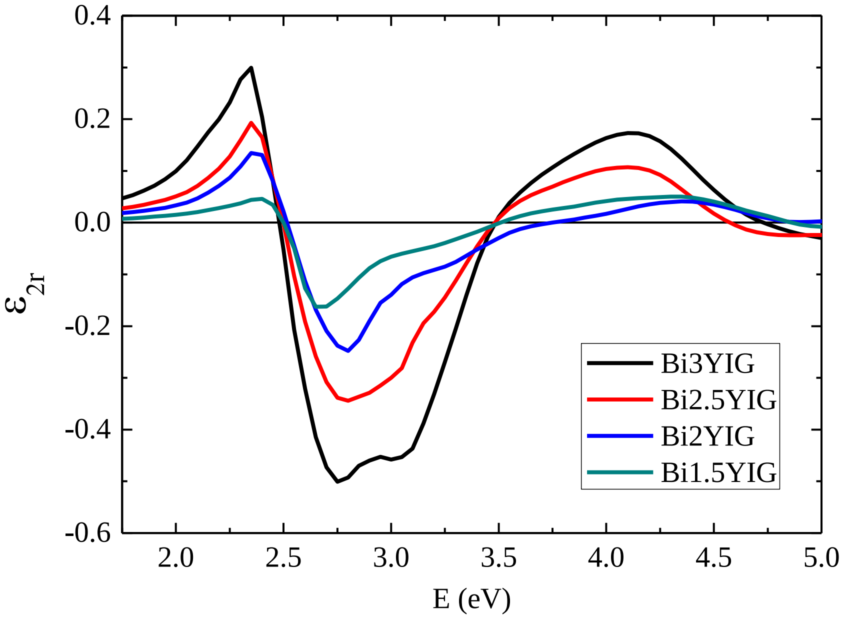

Figure 6.3.14: Real parts of off-diagonal elements of the permittivity tensor of Bix:YIGs.

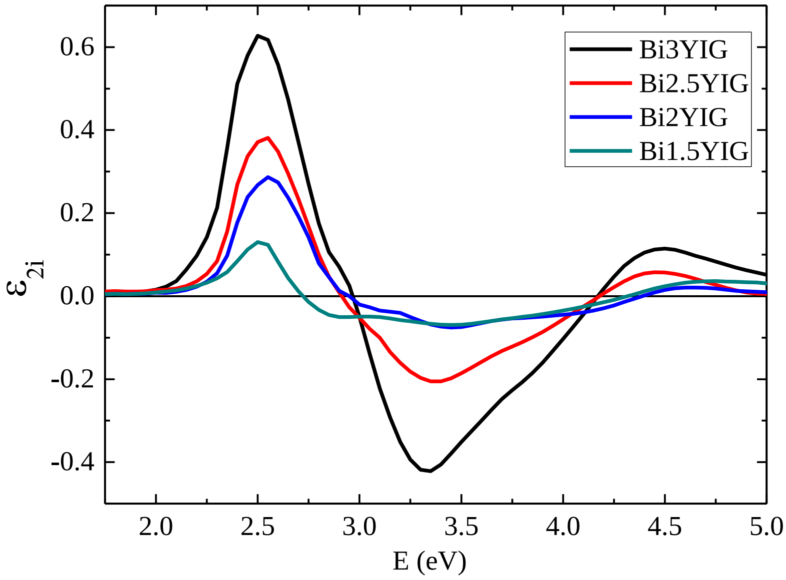

Figure 6.3.15: Imaginary parts of off-diagonal elements of the permittivity tensor of Bix:YIGs.

Table 6.3.4: Fitted parameters of Dia and Para transitions used to parameterize off-diagonal elements of Bix:YIGs permittivity tensors in the spectral range from 1.5 to 5.5 eV. Here, E_0 stands for central energy of the transition; *Amp* represents amplitude of the transition and Γ_0 is half-width in a half-height of the transition.

	Dia tr. 1			Dia tr. 2			Dia tr. 3			Dia tr. 4			Para tr. 1			Para tr. 1		
	E_0 (eV)	Amp	Γ_0 (eV)	E_0 (eV)	Amp	Γ_0 (eV)	E_0 (eV)	Amp	Γ_0 (eV)	E_0 (eV)	Amp	Γ_0 (eV)	E_0 (eV)	Amp	Γ_0 (eV)	E_0 (eV)	Amp	Γ_0 (eV)
Bi3IG	0.5	0.03	0.4	2.5	0.8	0.17	3.3	0.5	0.4	4.45	0.15	0.3	2.4	0.09	0.2	3.1	0.05	0.15
Bi2.5YIG	0.5	0.03	0.4	2.55	0.5	0.2	3.3	0.25	0.4	4.5	0.1	0.3	2.45	0.08	0.2	3.1	0	0.15
Bi2YIG	0.5	0.03	0.4	2.55	0.35	0.2	3.3	0.1	1	4.55	0.05	0.4	2.45	0.06	0.2	3.1	0	0.15
Bi1.5YIG	0.5	0.03	0.4	2.55	0.2	0.15	3.3	0.1	1	4.65	0.06	0.55	2.45	0.02	0.2	3	0.01	0.15

We would like to note in here that all the calculated permittivity tensor elements spectra have characteristic shape of diagonal and off-diagonal permittivity tensor elements of bulk-like epitaxial Bix:YIGs with small Bi concentrations [8, 74]. As explained earlier, properties of epitaxial films may differ from the properties of bulk-like materials. Therefore, we attributed result discrepancy to the fact that in this work we characterized epitaxial thin films. Results demonstrated, that MOD in as an effective technique for preparation of epitaxial thin garnet films on GGG substrate.

6.3.2. $Nd_2BiFe_{(5-x)}Ga_xO_{12}$ & $Nd_{0.5}Bi_{2.5}Fe_{(5-x)}Ga_xO_{12}$

In this sub-section, we focused on the determination of complete permittivity tensors of Bi1:NIGxGs and Bi2.5:NIGxGs thin films. We used optical and MO spectral measurements at energies from 1.5 to 5.5 eV. We examined optical properties by SE supported by transmission intensity measurements. From these data we derived the diagonal permittivity tensor elements. We examined MO properties by spectroscopic polar MOKE and Faraday effect rotation and ellipticity measurements. From these data we determined the spectral dependence of off-diagonal permittivity tensor elements. Finally, we parameterized obtained results in terms of microscopic theory.

We focused on $Nd_2BiFe_{(5-x)}Ga_xO_{12}$ and $Nd_{0.5}Bi_{2.5}Fe_{(5-x)}Ga_xO_{12}$ thin films (x = 0, 0.25, 0.75, 1) prepared by MOD method on $Gd_3Ga_5O_{12}$ (GGG) (111) substrates. Compositions of garnet films are listed in the table 6.3.5. MOD liquids for garnet films consisted of solutions made of Nd, Bi, Ga, and Fe carboxylates [20, 75]. We prepared MOD liquids by mixing each solution to obtain desired chemical compositions. We spin-coated those solutions on GGG (111) substrates with 3000 rpm for 30 s and continued by drying at 100 °C for 10 minutes using a hot-plate. In order to decompose organic materials and obtain amorphous oxide films, we pre-annealed samples at 450 °C for 10 minutes. We repeated this procedure, from spin coating to pre-annealing, 5 times in order to obtain appropriate thickness. Nominal thicknesses of studied garnet films were 200 nm (based on the number of MOD cycles calibrated by X-ray measurements). Finally, we annealed samples for crystallization in a furnace at 700 °C for 3 hours. We performed all the thermal treatments in the air. Figure 6.3.16 shows theoretical model structure of Bi1:NIGxGs and Bi2.5:NIGxGs samples used for SE, MOKE and Faraday effect analysis.

Table 6.3.5. Composition and nominal thicknesses of examined garnet films

Film composition	Indication in Figures and text	Nominal thickness (nm)
$Nd_2BiFe_5O_{12}$	Bi1NIG	200
$Nd_2BiFe_{4.75}Ga_{0.25}O_{12}$	Bi1NIG(0.25)G	200
$Nd_2BiFe_{4.25}Ga_{0.75}O_{12}$	Bi1NIG(0.75)G	200
$Nd_2BiFe_4GaO_{12}$	Bi1NIGG	200
$Nd_{0.5}Bi_{2.5}Fe_4GaO_{12}$	Bi2.5NIG	200
$Nd_{0.5}Bi_{2.5}Fe_{4.75}Ga_{0.25}O_{12}$	Bi2.5NIG(0.25)G	200
$Nd_{0.5}Bi_{2.5}Fe_{4.25}Ga_{0.75}O_{12}$	Bi2.5NIG(0.75)G	200
$Nd_{0.5}Bi_{2.5}Fe_4Ga_1O_{12}$	Bi2.5NIGG	200

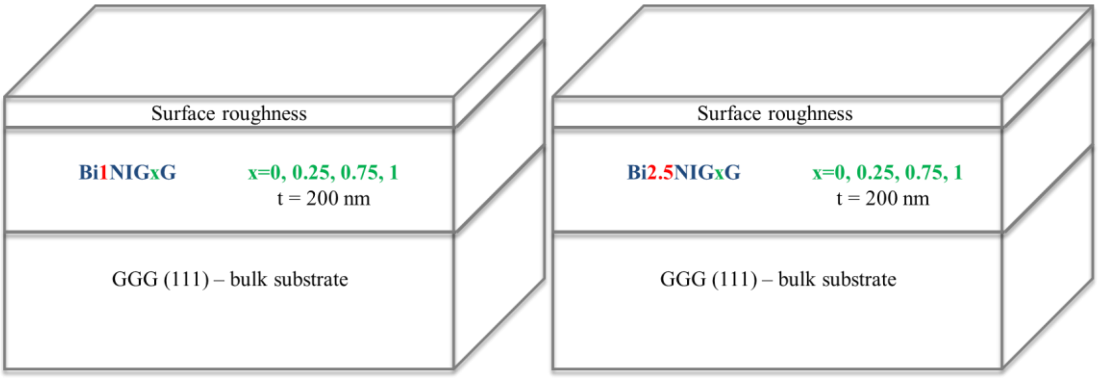

Figure 6.3.16: Model structure of Bi1NIGG and Bi2.5NIGG samples used for SE, MOKE and Faraday analysis calculations.

a) Spectroscopic Ellipsometry

We performed SE measurements on a Mueller matrix ellipsometer Woollam RC2. We measured spectral dependence of ellipsometric parameters ψ and Δ in reflection and at incident angles 55°, 60° and 65°. We used the same equipment to measure the transmission spectra at the incidence angle 0°. We performed measurements in the spectral range from 1.5 to 6.5 eV.

We analyzed SE experimental data using a CompleteEase software provided by Woollam Co.. We used MSA mode to obtain optical functions spectra (diagonal elements of the permittivity tensor ε_{1r} and ε_{1i}) of Bi1:NIGxGs and Bi2.5:NIGxGs. In MSA mode, we combined ellipsometric and transmission measurements. Transmission spectra supplemented our analysis because of the strong interference observed in ψ and Δ in the transparent region bellow 2.5 eV. We fitted the SE and transmission experimental data using model structure shown in Figure 6.3.16. To ensure Kramers-Kronig consistent results we parameterized obtained optical functions ε_{1r} and ε_{1i} of Bi1:NIGxGs and Bi2.5:NIGxGs by five Gaussian functions. Since substrates were transparent and both-side polished, we considered back reflections in the SE analysis. We fitted all thicknesses, including roughness in the CompleteEase software. We subsequently used these thicknesses in MOKE and Faraday spectra analysis. We listed some parameters of used parameterization functions in the Table 6.3.6 and the fitted thicknesses in the Table 6.3.7. Fitted interface thickness was zero for all the samples. This corresponds to epitaxial growth of our films on GGG substrate. Figure 6.3.17 shows that used theoretical model describes both: SE and transmission experimental spectra well.

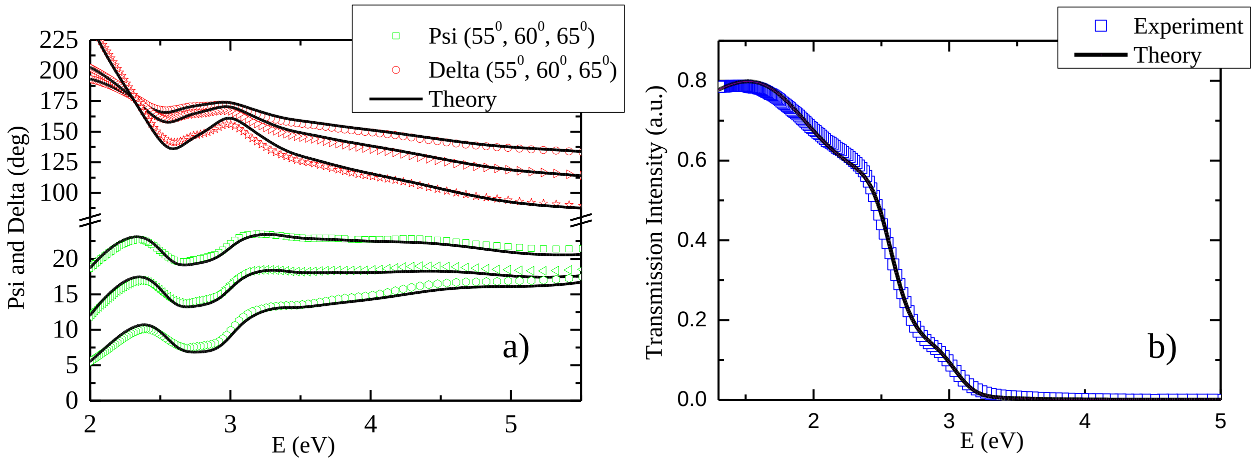

Figure 6.3.17: Experimental data for Bi1NIG layer on GGG substrate compared to the theoretical model. a) Variable angle Psi and Delta SE data. b) Measured transmission intensity spectra.

Table 6.3.6: Fitted parameters of Gaussian functions used to parameterize optical properties of Bi1:NIGxGs and Bi2.5:NIGxGs layers on GGG substrates in the spectral range from 1.5 to 6.5 eV. Here, E_0 stands for central energy of the function; Amp represents amplitude of the function and Br its broadening.

	Gaussian **1**			Gaussian **2**			Gaussian **3**		
	E_0 (eV)	Amp	Br (eV)	E_0 (eV)	Amp	Br (eV)	E_0 (eV)	Amp	Br (eV)
Bi**1**NIG	2.75	0.76	0.39	3.27	0.76	0.32	3.42	1.81	0.80
Bi**1**NIG(0.25)G	2.79	0.72	0.42	3.25	1.11	0.24	3.45	1.64	0.63
Bi**1**NIG(0.75)G	2.76	0.39	0.38	3.33	1.08	0.62	4.16	2.70	1.58
Bi**1**NIGG	2.75	0.19	0.29	3.38	1.32	0.84	4.26	1.07	0.88
Bi**2.5**NIG	2.59	1.35	0.35	3.33	4.91	1.03	4.12	3.12	0.93
Bi**2.5**NIG(0.25)G	2.61	1.31	0.34	3.17	3.11	0.80	4.03	3.14	1.52
Bi**2.5**NIG(0.75)G	2.63	1.13	0.36	3.18	2.72	0.82	4.08	3.03	1.58
Bi**2.5**NIGG	2.63	1.18	0.37	3.19	3.18	0.86	4.16	3.28	1.49

Gaussian **4**			Gaussian **5**		
E_0 (eV)	Amp	Br (eV)	E_0 (eV)	Amp	Br (eV)
4.06	2.69	1.39	5.70	3.20	3.16
4.02	2.92	1.40	5.72	3.18	3.06
5.48	1.41	1.43	6.98	2.69	2.40
5.31	1.81	2.26	8.02	2.5	4.59
4.94	2.04	1.21	6.24	3.53	3.28
5.40	3.69	2.30	7.94	5.66	3.61
5.72	3.88	2.82	7.22	2.76	2.59
6.09	5.22	2.48	7.05	6.41	4.21

Table 6.3.7: Fitted thicknesses and volume fractions used for model of Bi1:NIGxGs and Bi2.5:NIGxGs layers on GGG substrate in the spectral range from 1.5 to 6.5 eV. Here, $T_{Bi:NIGG}$ stands for film thickness; R_{rough} represents film roughness with volume fractions f_{rough}.

	$T_{Bi:NIGG}$ (nm)	R_{rough} (nm)	f_{rough}
Bi**1**NIG	168.5	0	0.5
Bi**1**NIG(0.25)G	205	0	0.5
Bi**1**NIG(0.75)G	250	0	0.5
Bi**1**NIGG	265	0	0.5
Bi**2.5**NIG	150	10	0.5
Bi**2.5**NIG(0.25)G	152	5.2	0.5
Bi**2.5**NIG(0.75)G	155	4.6	0.5
Bi**2.5**NIGG	157	5	0.5

Figure 6.3.18(a) shows parameterized optical functions ε_{1r} of Bi1:NIGxGs and Figure 6.3.18(b) parameterized optical functions ε_{1r} of Bi2.5:NIGxGs. From these spectra, it is apparent that Ga substitution decreases amplitudes of ε_{1r} for Bi1:NIGxGs bellow 4 eV and increasing them above. On the other hand, Ga substitution does not noticeably influence amplitudes of ε_{1r} for Bi2.5:NIGxGs. The only exception is ε_{1r} spectra of Bi2.5:NIG above 3.5 eV. We attribute this result to the fact that this composition contains no Ga.

Figure 6.3.19(a) shows parameterized optical functions ε_{1i} of Bi1:NIGxGs and Figure 6.3.19(b) parameterized optical functions ε_{1i} of Bi2.5:NIGxGs. In here we can observe that Ga substitution increases ε_{1i} amplitudes and therefore absorption of

Bi1:NIGxGs in measured spectral range. However it decreases ε_{1i} amplitudes of Bi2.5:NIGxGs. Moreover, the absorption of Bi2.5:NIGxGs is almost 30% stronger than absorption of Bi1:NIGxGs. We attribute this result to the higher Bi concentration which was demonstrated in the part devoted to Bix:YIGs.

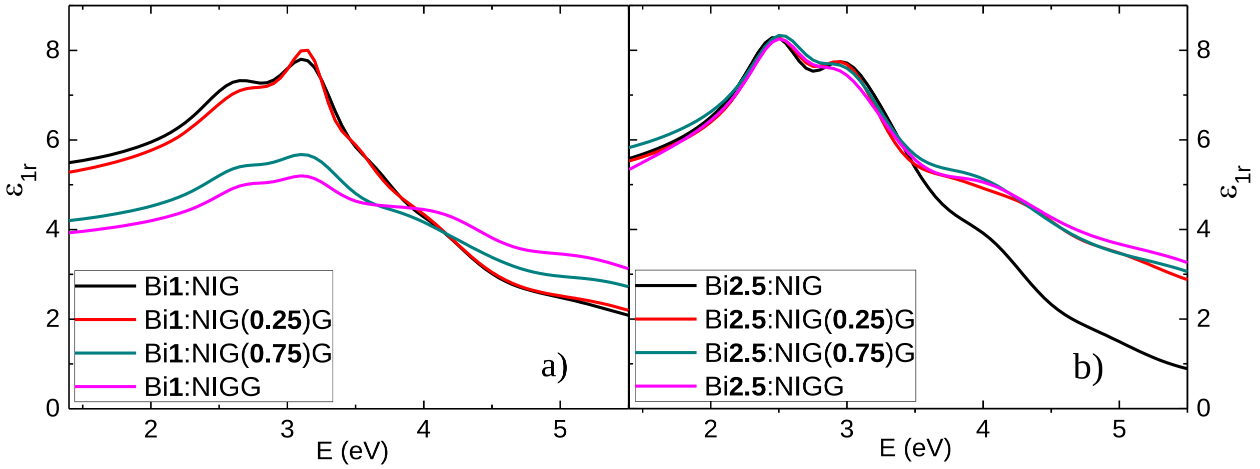

Figure 6.3.18: Real parts of the diagonal permittivity tensor elements ε_{1r} for a) Bi1:NIGxGs and b) Bi2.5:NIGxGs.

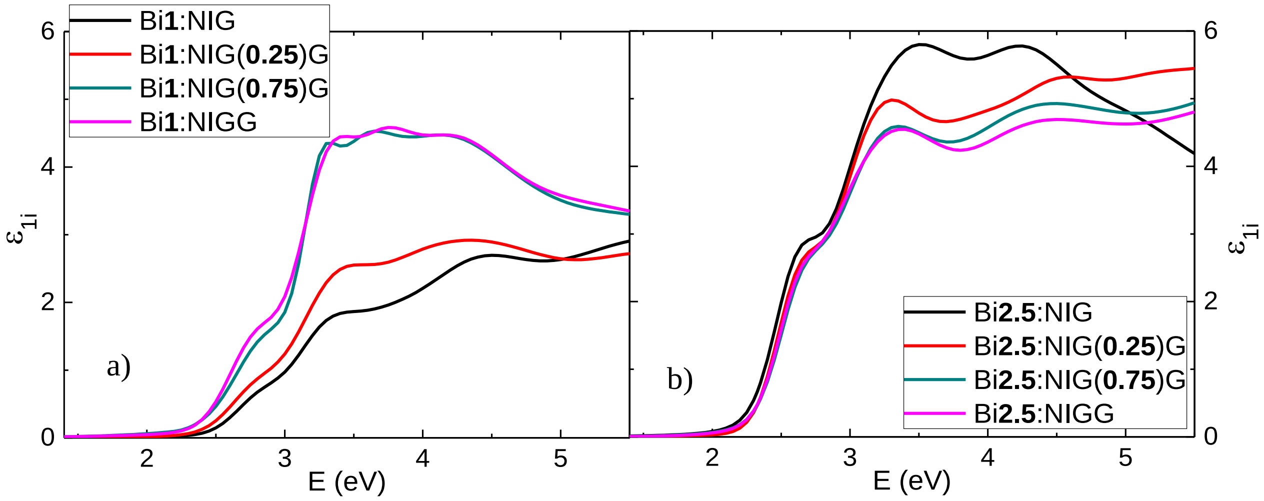

Figure 6.3.19: Imaginary parts of the diagonal permittivity tensor elements ε_{1i} for a) Bi1:NIGxGs and b) Bi2.5:NIGxGs.

b) MOKE and Faraday effect spectroscopy

We studied MO properties of Bi1:NIGxGs and Bi2.5:NIGxGs by MOKE and MO Faraday effect spectroscopy. We measured spectra of polar MOKE rotation and ellipticity at room temperature at nearly normal light incidence. We applied magnetic field 1.2 T, which was enough for samples saturation. Incident light was p-polarized. We recorded data in the photon energy range from 1.4 to 5 eV. Similarly, we measured spectra of Faraday rotation and ellipticity at room temperature using magnetic field 670 mT (enough for samples saturation). We recorded experimental data in the photon energy range from 1.4 to 4 eV.

Figure 6.3.20(a) shows measured MOKE rotation spectra of Bi1:NIGxGs and Figure 6.3.20(b) of Bi2.5:NIGxGs. Figure 6.3.21(a) shows measured MOKE ellipticity spectra of Bi1:NIGxGs and Figure 6.3.21(b) of Bi2.5:NIGxGs. Firstly, we can observe strong MO interference in the form of strong oscillations in the spectral range bellow 3 eV for Bi1:NIGxGs and Bi2.5:NIGxGs in both, rotation and ellipticity. Since our samples had different thicknesses, we observed different interference patterns for each one of them (see Table 6.3.7). Secondly, MOKE rotation shows extremes around 3.5 and 4.5 eV for both sample sets. However, it is apparent that Bi2.5:NIGxGs shows higher MOKE amplitudes at extremes caused by the higher Bi content [8, 87]. Finally, MOKE ellipticity shows extreme around 4.1 eV for both sample sets which is characteristic for iron garnets MOKE spectra [8, 74, 87]. Important observation here is that Ga substitution decreases MOKE rotation amplitudes at extremes. As expected, spectra demonstrated that Bi substitution increases and Ga substitution decreases amplitudes of MOKE ellipticity.

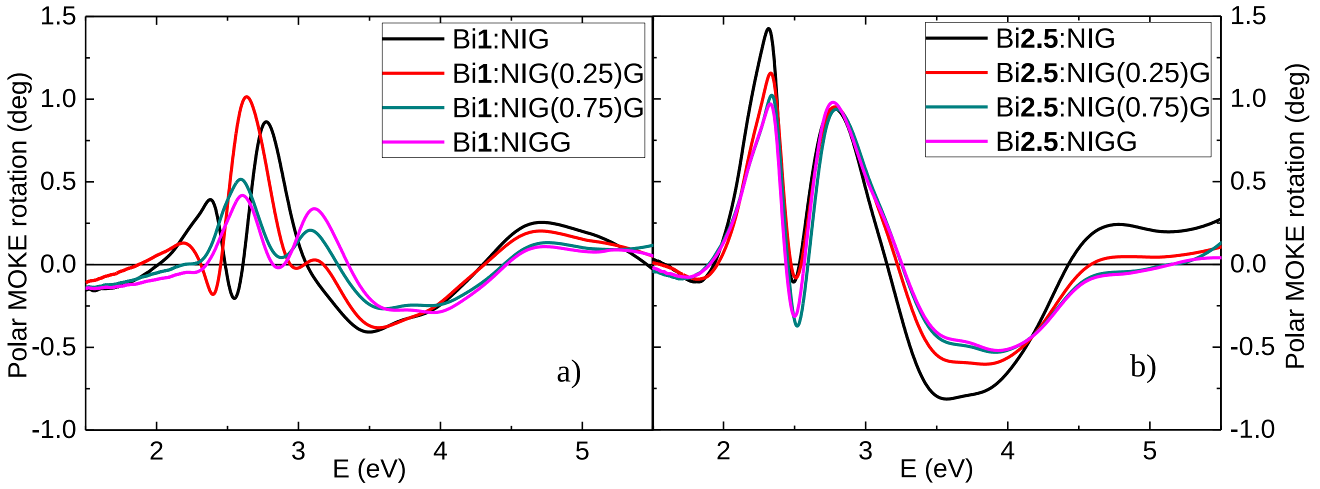

Figure 6.3.20: Polar MOKE rotation spectra for a) Bi1:NIGxGs and b) Bi2.5:NIGxGs on GGG substrates.

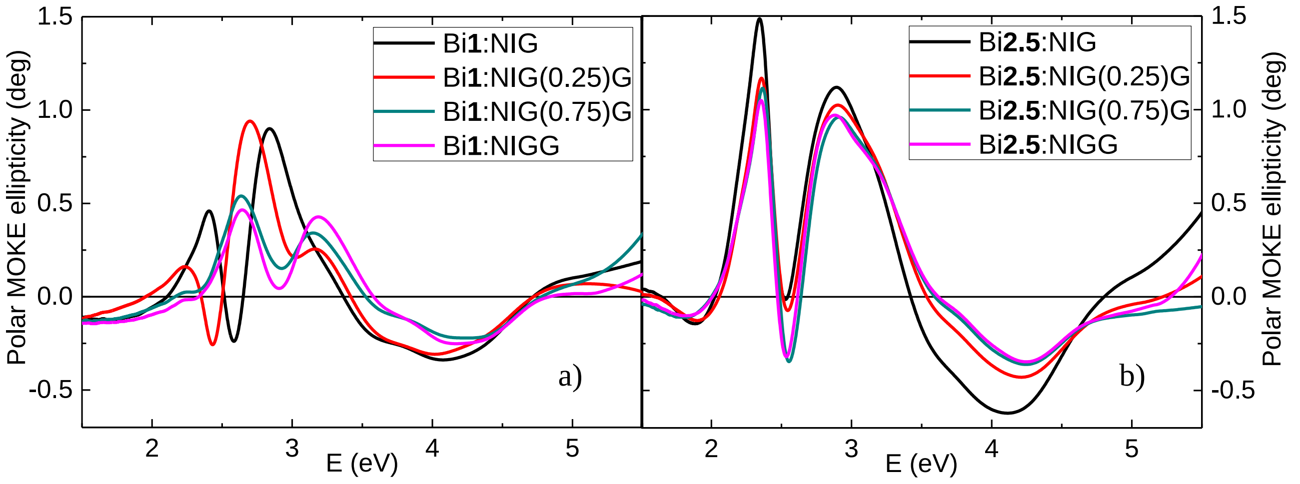

Figure 6.3.21: Polar MOKE ellipticity spectra for a) Bi1:NIGxGs and b) Bi2.5:NIGxGs on GGG substrates.

Figure 6.3.22(a) shows measured MO Faraday rotation spectra for Bi1:NIGxGs and Figure 6.3.22(b) for Bi2.5:NIGxGs. Figure 6.3.23(a) shows measured MO Faraday ellipticity spectra for Bi1:NIGxGs and Figure 6.3.23(b) for Bi2.5:NIGxGs. We corrected experimental data for the rotation from the substrate. We observed Faraday rotation extremes near 2.5 and 3 eV, and Faraday ellipticity extremes near 2.3 and 3.3 eV for both sample sets. Spectra clearly demonstrated that Bi2.5:NIGxGs shows higher Faraday rotation and ellipticity amplitudes at extremes, caused by the higher

Bi content [8, 74, 87]. One important thing to notice is that Ga substitution decreases MO Faraday effect amplitudes at extremes. This effect of Ga will be discussed later in the part devoted to the microscopic analysis of studied materials.

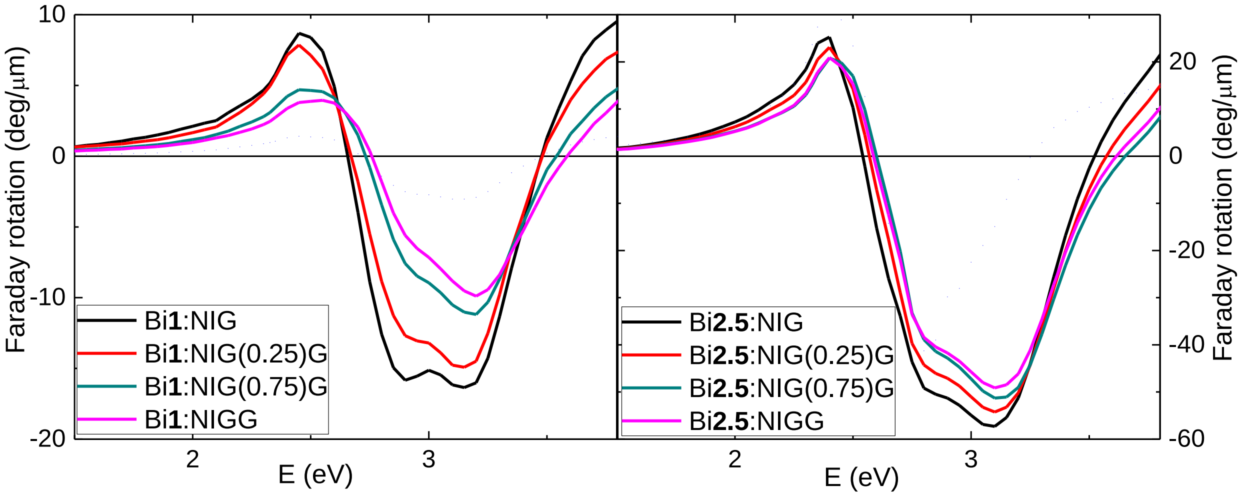

Figure 6.3.22: MO Faraday rotation spectra for a) Bi1:NIGxGs and b) Bi2.5:NIGxGs on GGG substrates.

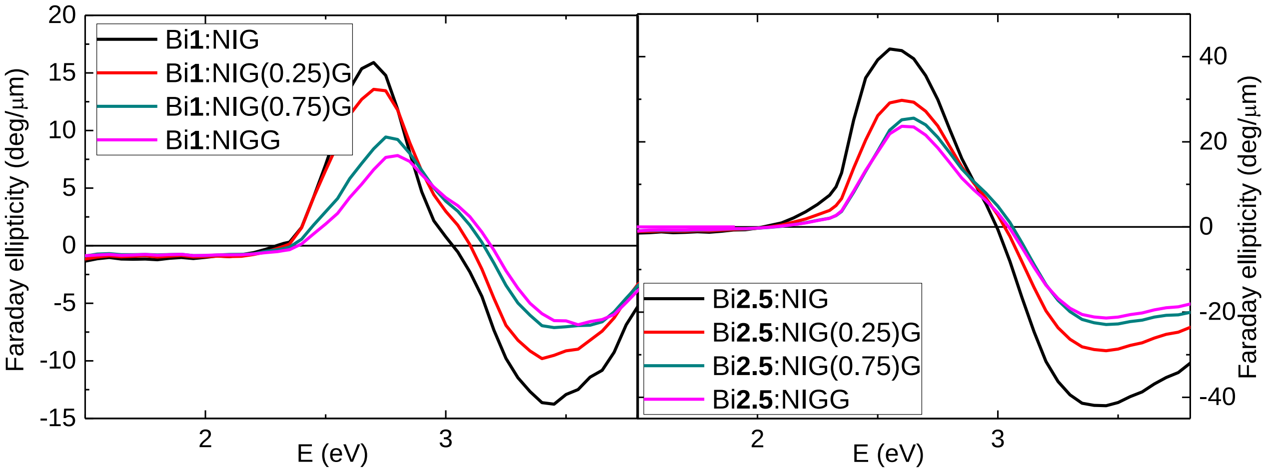

Figure 6.3.23: MO Faraday ellipticity spectra for a) Bi1:NIGxGs and b) Bi2.5:NIGxGs on GGG substrates.

We calculated off-diagonal elements of the permittivity tensor ε_{2r} and ε_{2i} from MOKE and Faraday effect spectra. We performed calculations using Yeh's 4x4 matrix formalism and diagonal elements of the permittivity tensor determined by SE. As already mentioned, there was strong MO interference bellow 3 eV in MOKE spectra. Therefore, we used MO Faraday effect spectra in the spectral range from 1.5 to 3 eV and MOKE spectra in the spectral range from 3 to 5 eV. Figure 6.3.24(a) shows real parts of off-diagonal permittivity tensor elements ε_{2r} of Bi1:NIGxGs and Figure 6.3.24(b) of Bi2.5:NIGxGs. Figure 6.3.25(a) shows imaginary parts of off-diagonal permittivity tensor elements ε_{2i} of Bi1:NIGxGs and Figure 6.3.25(b) of Bi2.5:NIGxGs. As expected from previous results, Bi substitution increases ε_{2r} and ε_{2i} amplitudes at extremes for both, Bi1:NIGxGs and Bi2.5:NIGxGs. However, Ga substitution acts in an opposite manner and it decreases ε_{2r} and ε_{2i} amplitudes.

To explain the effect of Ga properly, one has to look at the results from microscopic theory. For this purpose, we parameterized off-diagonal elements spectra of Bi1:NIGxGs and Bi2.5:NIGxGs permittivity tensors, ε_{2r} and ε_{2i}. We listed some of used transitions parameters in table 6.3.4. We used four Para transition terms at 2.4-2.5, 3-3.2, 3.6-4.1 and 5.7-6.6 eV to represent crystal field transitions. Furthermore, we used four Dia transition terms at 0.5, 2.58-2.8, 3.3-3.58 and 4.05-4.4 eV. We used Dia transition at 0.5 eV and Para transition at 5.7-6.6 eV only to model combined effect of transitions outside of measured spectral range and we do not assign them any physical meaning in here. First thing to notice is that the main contribution comes, similarly to Bix:YIGs, from Dia transitions at 2.58-2.8 eV and 3.3-3.58 eV. These are associated with transitions t2(Fe3+) → t2g(Fe2+) and eg(Fe3+) → e(Fe2+) respectively. As mentioned before, these transitions are mainly responsible for the remarkable increase of the Faraday rotation in the visible and near infrared region. From the data in the table 6.3.4 one can see that Ga substitution is decreasing these transitions for both materials. This is in accordance with the assumption, that Ga is mostly substituted for Fe3+ tetrahedral, which is crucial for both transitions. Maxima at 2.4 eV are mainly created by the overlap of secondary negative peaks of these two Dia transitions. One can also notice that Ga substitution lowers energy of much smaller Dia transition at 4.65 eV which most likely exist due to charge transfers from oxygen to octahedral Fe. This is in accordance with the assumption that Ga is in a smaller percentage also substituted per Fe3+ octahedral.

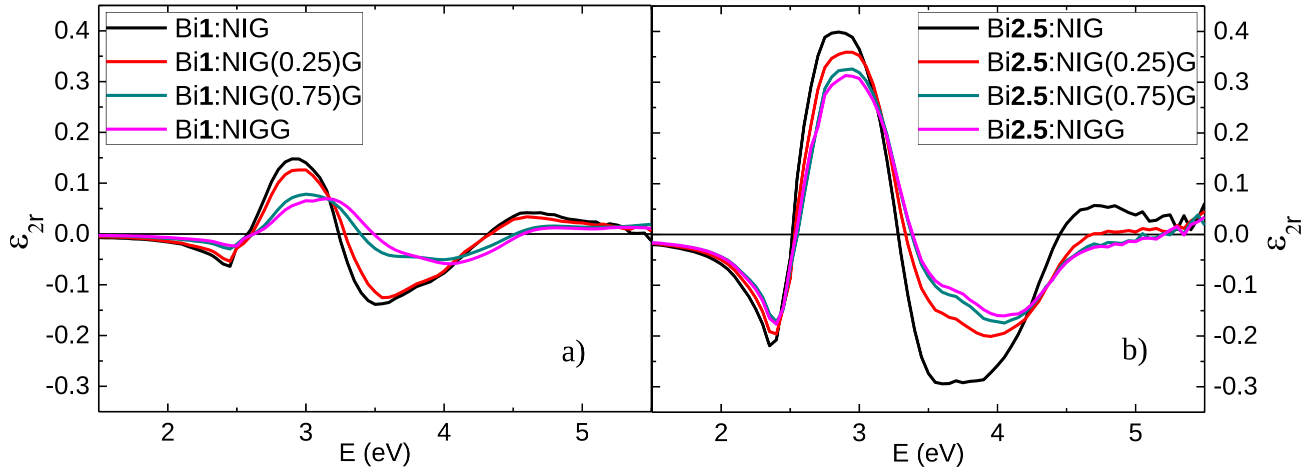

Figure 6.3.24: Real parts of the off-diagonal permittivity tensor elements ε_{2r} for a) Bi1:NIGxGs and b) Bi2.5:NIGxGs.

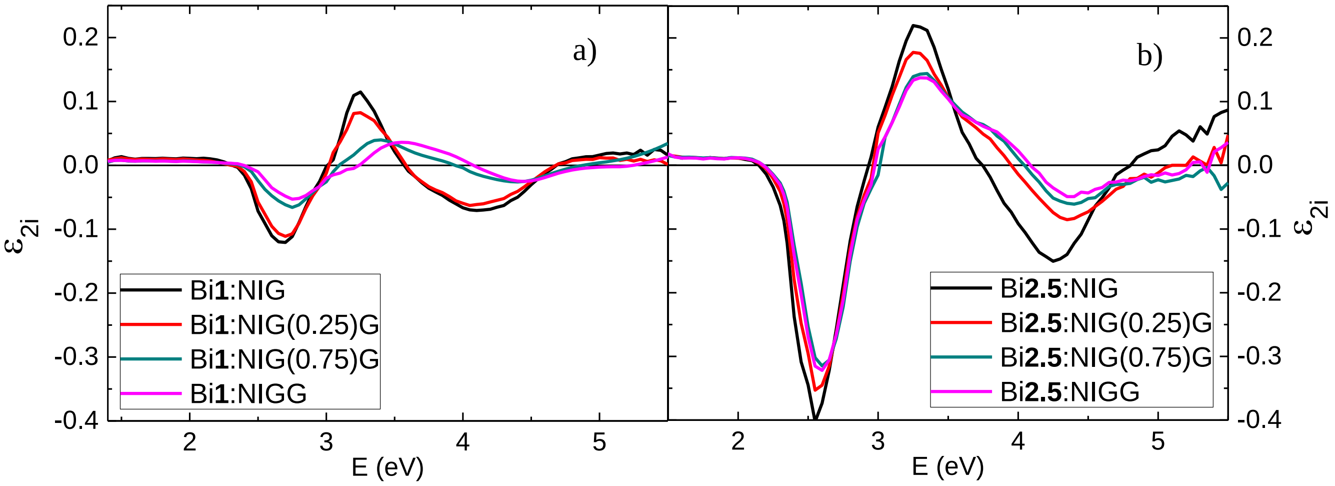

Figure 6.3.25: Real parts of the off-diagonal permittivity tensor elements ε_{2r} for a) Bi1:NIGxGs and b) Bi2.5:NIGxGs.

Table 6.3.8: Fitted parameters of Para and Dia transitions used to parameterize off-diagonal elements of the permittivity tensors of Bi1:NIGxGs and Bi2.5:NIGxGs layers prepared on GGG (111) substrates in the spectral range from 1.5 to 5.5 eV. Here, E_0 stands for central energy of the function; Amp represents amplitude of the function and Γ_0 is half-width in a half-height of the transition.

	Dia tr. **1**			Dia tr. **2**			Dia tr. **3**			Dia tr. **4**		
	E_0 (eV)	Amp	Γ_0 (eV)	E_0 (eV)	Amp	Γ_0 (eV)	E_0 (eV)	Amp	Γ_0 (eV)	E_0 (eV)	Amp	Γ_0 (eV)
Bi**1**NIG	0.5	0.04	0.4	2.67	0.14	0.2	3.24	0.2	0.2	4.1	0.1	0.6
Bi**1**NIG(0.25)G	0.5	0.03	0.4	2.68	0.14	0.2	3.25	0.16	0.25	4.05	0.09	0.5
Bi**1**NIG(0.75)G	0.5	0.03	0.4	2.75	0.08	0.2	3.35	0.07	0.3	4.39	0.04	0.4
Bi**1**NIGG	0.5	0.03	0.4	2.8	0.065	0.3	3.58	0.065	0.4	4.4	0.05	0.4
Bi**2.5**NIG	0.5	0.03	0.4	2.58	0.55	0.5	3.3	0.38	0.5	4.25	0.28	0.5
Bi**2.5**NIG(0.25)G	0.5	0.03	0.4	2.6	0.45	0.17	3.3	0.28	0.5	4.4	0.17	0.55
Bi**2.5**NIG(0.75)G	0.5	0.03	0.4	2.6	0.43	0.17	3.3	0.24	0.5	4.4	0.12	0.55
Bi**2.5**NIGG	0.5	0.03	0.4	2.6	0.42	0.17	3.3	0.23	0.5	4.4	0.12	0.55

Para tr. **1**			Para tr. **2**			Para tr. **3**			Para tr. **4**		
E_0 (eV)	Amp	Γ_0 (eV)	E_0 (eV)	Amp	Γ_0 (eV)	E_0 (eV)	Amp	Γ_0 (eV)	E_0 (eV)	Amp	Γ_0 (eV)
2.5	0.005	0.3	3	0.025	0.3	3.6	0.03	0.6	5.8	0.03	0.6
2.5	0.005	0.3	3	0.015	0.3	3.6	0.03	0.6	5.8	0.03	0.7
2.5	0.004	0.2	3.1	0.01	0.3	3.8	0.02	0.6	6	0.034	0.78
2.5	0.004	0.3	3.2	0.01	0.2	4	0.02	0.6	6.6	0.035	0.8
2.4	0.07	0.2	3.1	0.009	0.3	3.9	0.06	0.6	5.7	0.06	0.5
2.4	0.05	0.2	3.1	0.009	0.3	4.1	0.07	0.6			
2.4	0.05	0.2	3.2	0.008	0.2	4.1	0.08	0.6			
2.4	0.03	0.2	3.2	0.008	0.3	4.1	0.06	0.6			

6.4. Ce$_{(0.95-x)}$Hf$_x$Co$_{0.05}$O$_{(2-\delta)}$

In recent years, magnetically doped CeO$_2$ attracted a lot of attention since it is a promising magnetic semiconductor and also highly applicable material in the field of integrated photonics. This ranges from MO applications such as integrated MO isolators or magneto-plasmonic sensors to magneto-photonic crystals [88-91]. The main advantage of this material is its high Curie temperature and more importantly a great Si compatibility [92]. Moreover, it is possible to tune CeO$_2$ magnetic properties by doping of the non-magnetic lattice by magnetic ions [88]. In this work we used Hf and Co doping. Successful adoption of this material in MO devices requires complete understanding of the nature and origin of CeO_2 magnetic properties. Even though is the room temperature ferromagnetism in this material explained by an oxygen vacancy mechanism [93, 94], the detail optical and MO analysis is still needed.

In this section, we focused mainly on the determination of full dielectric permittivity tensors of $Ce_{(0.95-x)}Hf_xCo_{0.05}O_{(2-\delta)}$ (CeHfCoO) thin films. For this purpose we used optical and MO spectral measurements at energies from 1.5 to 5.5 eV. We used SE supported by transmission intensity measurements to study CeHfCoO optical properties and to derive the diagonal permittivity tensor elements spectra. We used spectroscopic Faraday effect rotation and ellipticity measurements to study CeHfCoO MO properties and to derive the spectral dependence of off-diagonal permittivity tensor elements. Finally, we parameterized obtained results in terms of microscopic theory.

We studied polycrystalline $Ce_{(0.95-x)}Hf_xCo_{0.05}O_{(2-\delta)}$ thin films (x = 0, 0.15, 0.35, 0.475, 0.6, 0.8, 0.95) prepared by pulsed laser deposition method on 2 types of substrates: amorphous quartz and Si/SiO_2. The deposition was carried out in vacuum (at base pressure 1.0×10^{-6} Torr) with substrate temperature of 700^0C. We listed CeHfCoO thin films compositions and nominal thicknesses (determined by profilometer) in table 6.4.1. Figure 6.4.1 shows theoretical model structure of CeHfCoO samples used for SE and Faraday effect analysis.

Table 6.4.1: Composition and nominal thicknesses of examined CeHfCoO thin films prepared on amorphous quartz and Si/SiO_2 substrates.

Film composition	Indication in Figures and text	Nominal thickness (nm)
$Ce_{0.95}Co_{0.05}O_{(2-\delta)}$	Ce0.95CoO	310
$Ce_{0.8}Hf_{0.15}\ Co_{0.05}O_{(2-\delta)}$	CeHf0.15CoO	310
$Ce_{0.6}Hf_{0.35}\ Co_{0.05}O_{(2-\delta)}$	CeHf0.35CoO	310
$Ce_{0.475}Hf_{0.475}\ Co_{0.05}O_{(2-\delta)}$	CeHf0.475CoO	340
$Ce_{0.35}Hf_{0.60}\ Co_{0.05}O_{(2-\delta)}$	CeHf0.60CoO	310
$Ce_{0.15}Hf_{0.80}\ Co_{0.05}O_{(2-\delta)}$	CeHf0.80CoO	300
$Hf_{0.95}Co_{0.05}O_{(2-\delta)}$	Hf0.95CoO	150

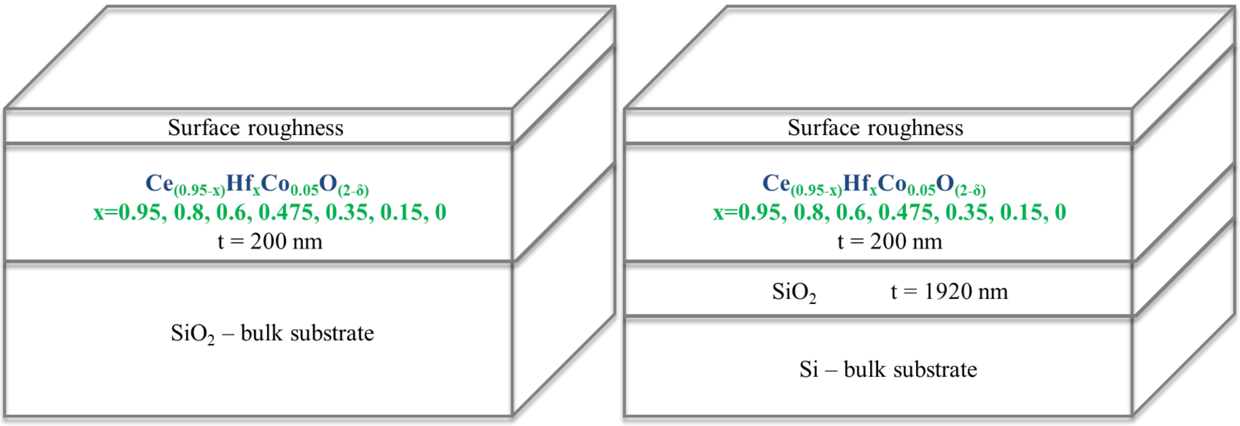

Figure 6.4.1: Model structure of CeHfCoO samples used for SE and Faraday analysis calculations.

a) Spectroscopic Ellipsometry

We performed SE measurements on a Mueller matrix ellipsometer Woollam RC2. We measured spectral dependence of ellipsometric parameters ψ and Δ in reflection and at incident angles 55°, 60° and 65°. We used the same equipment to measure the transmission spectra of CeHfCoO thin films prepared on transparent amorphous quartz substrates and we used incidence angle 0°. We performed measurements in the spectral range from 1.5 to 6.5 eV.

We analyzed SE experimental data using a CompleteEase software provided by Woollam Co.. We used MSA mode to obtain optical functions spectra (diagonal elements of the permittivity tensor ε_{1r} and ε_{1i}) of CeHfCoO thin films. In MSA mode, we combined SE and transmission measurements for each CeHfCoO film composition on both substrates. This means that for each composition we took experimental data from CeHfCoO sample prepared on quartz substrate (ψ, Δ and transmission experimental spectra) and combined them with experimental data from CeHfCoO sample prepared on Si/SiO$_2$ substrate (ψ and Δ experimental spectra). In MSA, we treated CeHfCoO, Si and SiO$_2$ optical functions as parameters common for both samples. We treated all thicknesses (including roughness thickness) as parameters allowed to wary for each sample independently. This approach provided us with the more accurate results since it ensured that obtained constants describe all types of experimental data well. Figure 6.4.2 shows that used theoretical model describes both SE experimental spectra well for both substrates. As a final SE step, we parameterized derived diagonal elements of the permittivity tensor ε_{1r} and ε_{1i} using a combination of Tauc-Lorentz and Lorentz oscillators. We did this to obtain Kramers-Kronig consistent results. We listed some parameters of used oscillator functions in Table 6.4.2 and the fitted thicknesses in Table 6.4.3. We subsequently used all fitted thicknesses (including roughness) obtained from SE analysis in Faraday effect analysis.

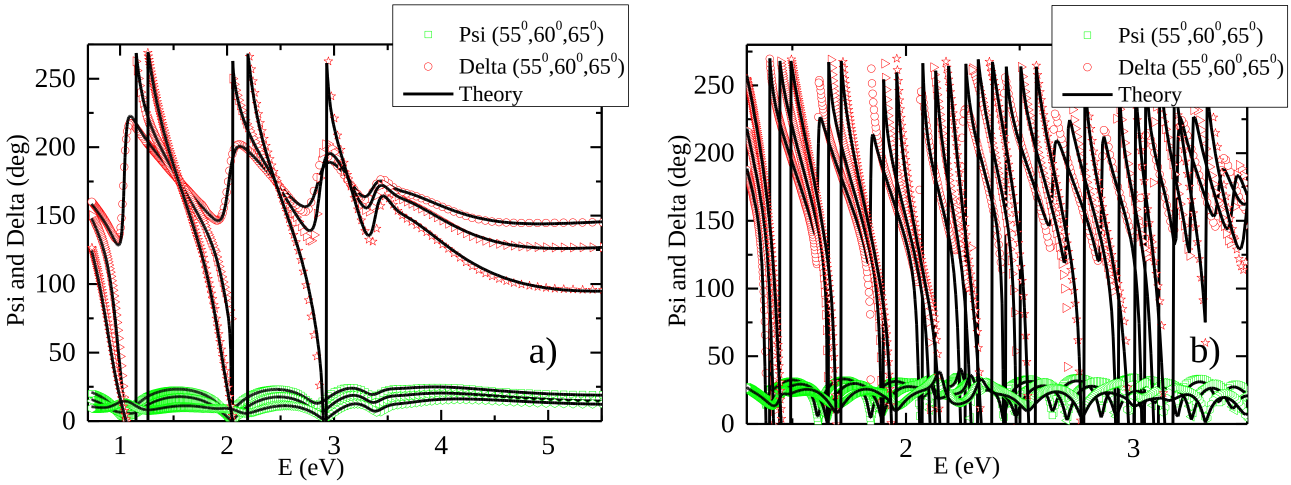

Figure 6.4.2: Measured SE variable angle Psi and Delta spectra of a) CeHf0.15CoO prepared on Si/SiO2 substrate and b) CeHf0.15CoO prepared on quartz substrate compared to the theoretical model.

Table 6.4.2: Fitted parameters of oscillator functions used to parameterize optical properties of CeHfCoO thin films prepared on amorphous quartz and Si/SiO$_2$ substrates in the spectral range from 1.7 to 5 eV. Here, E$_0$ stands for central energy of the function; Amp represents amplitude of the function and Br its broadening.

	Tauc-Lorentz			Lorentz **1**			Lorentz **2**		
	E_0 (eV)	Amp	Br (eV)	E_0 (eV)	Amp	Br (eV)	E_0 (eV)	Amp	Br (eV)
Ce0.95CoO									
CeHf0.15CoO									
CeHf0.35CoO									
CeHf0.475CoO									
CeHf0.60CoO									
CeHf0.80CoO									
Hf0.95CoO									

Lorentz **3**			Lorentz **4**		
E_0 (eV)	Amp	Br (eV)	E_0 (eV)	Amp	Br (eV)

Table 6.4.3: Fitted thicknesses and volume fractions used for model of CeHfCoO layers on quartz and Si/ SiO_2 substrate in the spectral range from 1.7 to 5 eV. Here, T/quartz and R/quartz stand for thickness and roughness of CeHfCoO films prepared on quartz substrate respectively; T/Si and R/Si stand for thickness and roughness of CeHfCoO films prepared on Si substrate.

	T /quartz (nm)	R /quartz (nm)	T/Si (nm)	R/Si (nm)
Ce0.95CoO				
CeHf0.15CoO				
CeHf0.35CoO				
CeHf0.475CoO				
CeHf0.60CoO				
CeHf0.80CoO				
Hf0.95CoO				

Figure 6.4.3 shows real parts of diagonal permittivity tensor elements ε_{1r} of CeHfCoO films. The spectral dependence of ε_{1r} is similar in shape to results obtained on pure or Co doped CeO_2 films [95-97]. We can observe that all the spectra are characteristic by one global maxima shifting from 3.6 eV to higher energies when Hf content increasing. Moreover, it is apparent that Hf content decreases ε_{1r} amplitudes in the whole measured spectral range. This is caused by smaller absorption. One extra thing to observe are slightly higher amplitudes for Hf0.95Co material then expected (above 3 eV) from the trend that shows other compositions when increasing Hf content. We assume that this is probably caused by missing Co in the structure.

Figure 6.4.4 shows imaginary parts of the diagonal permittivity tensor elements ε_{1i} of CeHfCoO thin films. In here we can observe optical bandgap energies to be shifted from 3.21 to 4.1 eV when Hf content increases. These energies are related to O2p -> Ce4f electronic transitions [97-99]. Moreover, one can see that Hf doping decreases ε_{1i} amplitudes in the whole measured spectral range. From this result we assume that when is Hf replacing Ce in the material; it actually acts against optical vacancies from isolated Ce4f states localized within the optical bandgap. These vacancies serves as recombination centers for optically excited electrons from the valence band to the 4f band of the oxide and are responsible for enhanced optical absorption [97, 98, 100]. One more thing to support this theory is increased absorption tail bellow 3.2 eV for our samples. This absorption tail was previously explained by the effect of midgap defects (midgap oxygen vacancies, Co states) [97] and it can be clearly seen that this tail disappearing when Hf content increases.

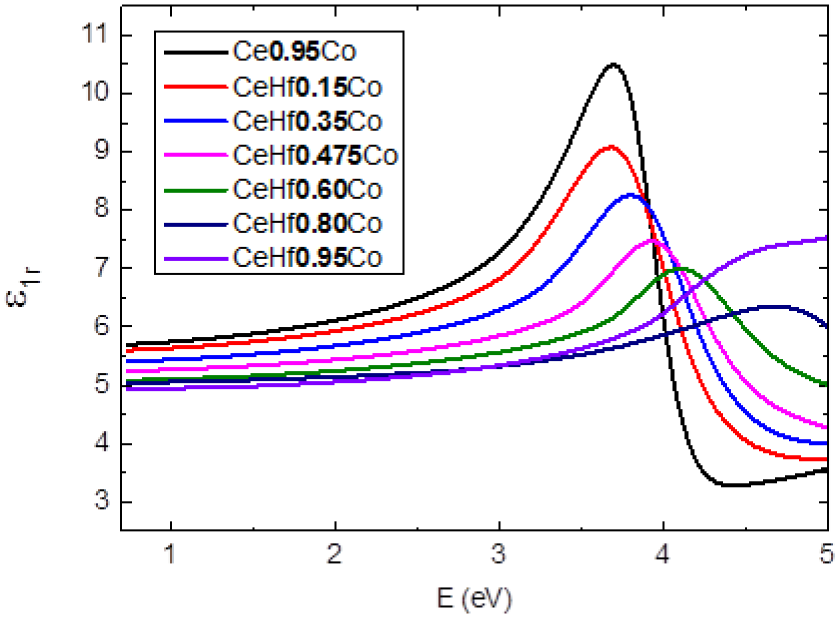

Figure 6.4.3: Real parts of the diagonal permittivity tensor elements ε_{1r} for CeHfCoO thin films.

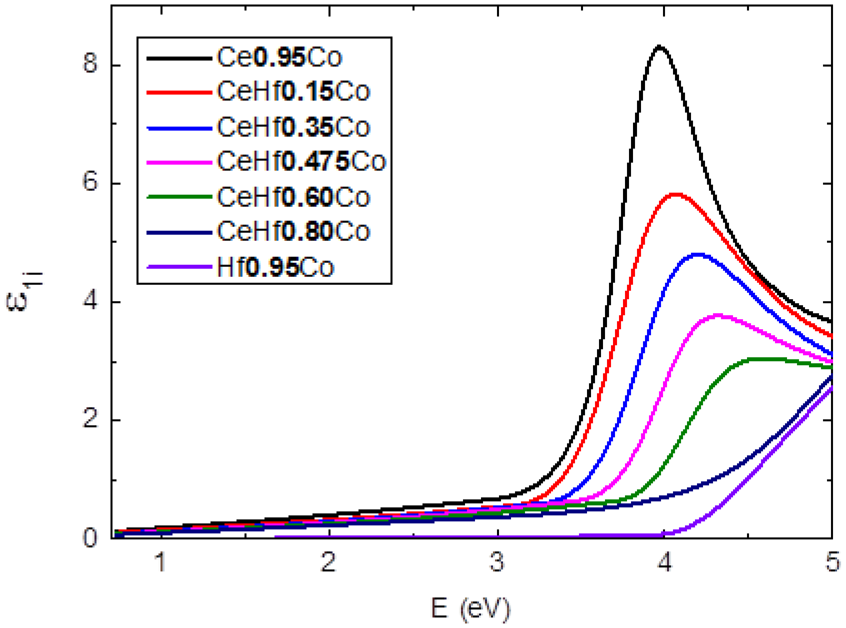

Figure 6.4.4: Imaginary parts of the diagonal permittivity tensor elements ε_{1i} for CeHfCoO thin films.

b) Faraday effect spectroscopy

We studied MO properties of examined samples by MO Faraday effect spectroscopy. We performed this type of measurement only on samples with quartz substrate since these samples are transparent in the whole measured spectral range. Therefore, there was no need for additional MOKE measurement. We acquired all the spectra at room temperature and normal light incidence. We applied magnetic field 670 mT, which was enough for samples saturation. Incident light was p-polarized. We recorded data in the photon energy range from 0.7 to 4 eV.

Figure 6.4.5 shows measured MO Faraday rotation spectra of CeHfCoO films. Figure 6.4.6 shows measured MO Faraday ellipticity spectra of CeHfCoO films. We corrected experimental data for the rotation from the substrate. We observed Faraday rotation extreme shifting from 2.9 eV to higher energies and decreased rotation amplitudes when Hf content increased. On the other hand, ellipticity amplitudes increased their values when Hf content increased. Spectra of the fully Hf substituted sample Hf0.95CoO has different rotation and ellipticity amplitudes than expected from the trend seen on other samples when Hf concentration increases. We attribute this to the missing Ce in the structure.

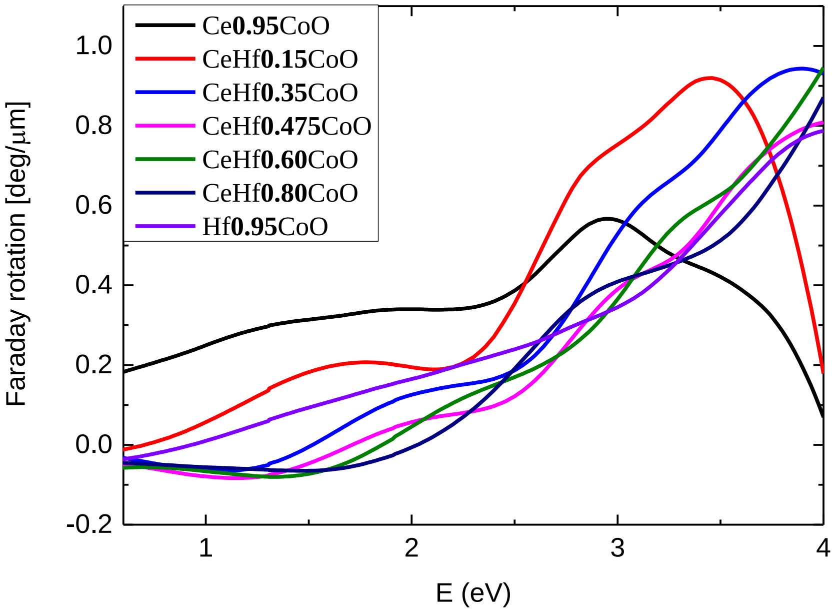

Figure 6.4.5: MO Faraday rotation spectra of CeHfCoO films prepared on quartz substrates.

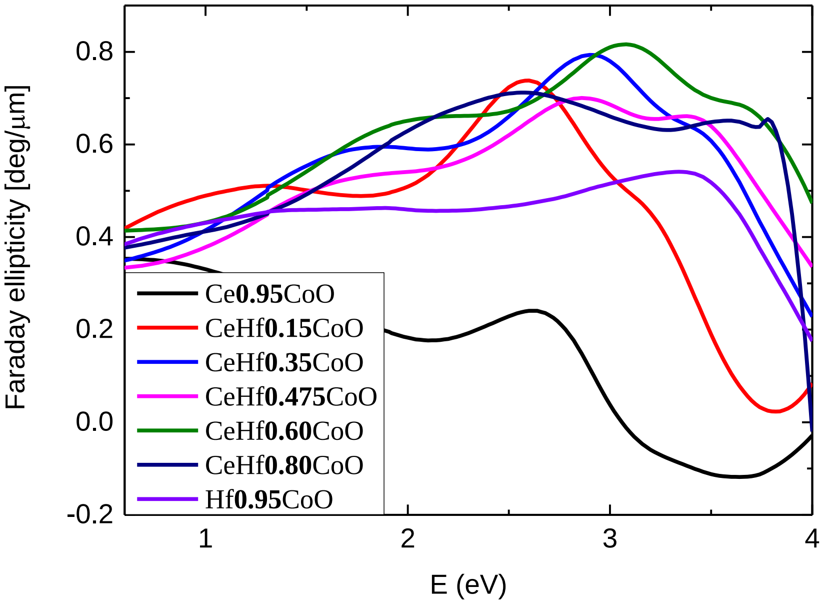

Figure 6.4.6: MO Faraday ellipticity spectra of CeHfCoO films prepared on quartz substrates.

We calculated the off-diagonal elements of the permittivity tensor ε_{2r} and ε_{2i} from Faraday effect spectra using Yeh's 4x4 matrix formalism and diagonal elements of the permittivity tensor determined by SE. Figure 6.4.7 shows the real parts of the off-diagonal permittivity tensor elements ε_{2r}. Figure 6.4.8 shows the imaginary parts of the off-diagonal permittivity tensor elements ε_2. Spectra clearly demonstrated that Hf substitution decreases both, ε_{2i} and ε_{2r} amplitudes and shifting their maxima to higher energies in the measure spectral range. This can be explained by the fact that perpendicular magnetic anisotropy and room temperature feromagnetism in this material is attributed to the magnetoelastic effects. These effects originate from distortions which are caused by in-plane compressive strain and vary mainly with Ce-Co content [97, 101]. Hf substitution not only influences this content, but it also reduces oxygen vacancies which also play an important role in CeHfCoO magnetism.

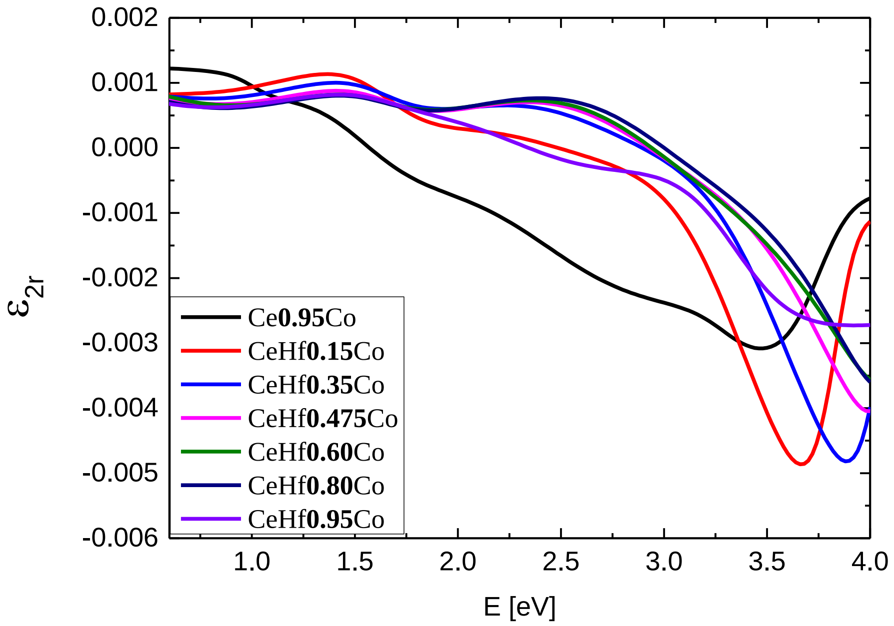

Figure 6.4.7: Real parts of the off-diagonal permittivity tensor elements ε_{2r} of CeHfCoO films

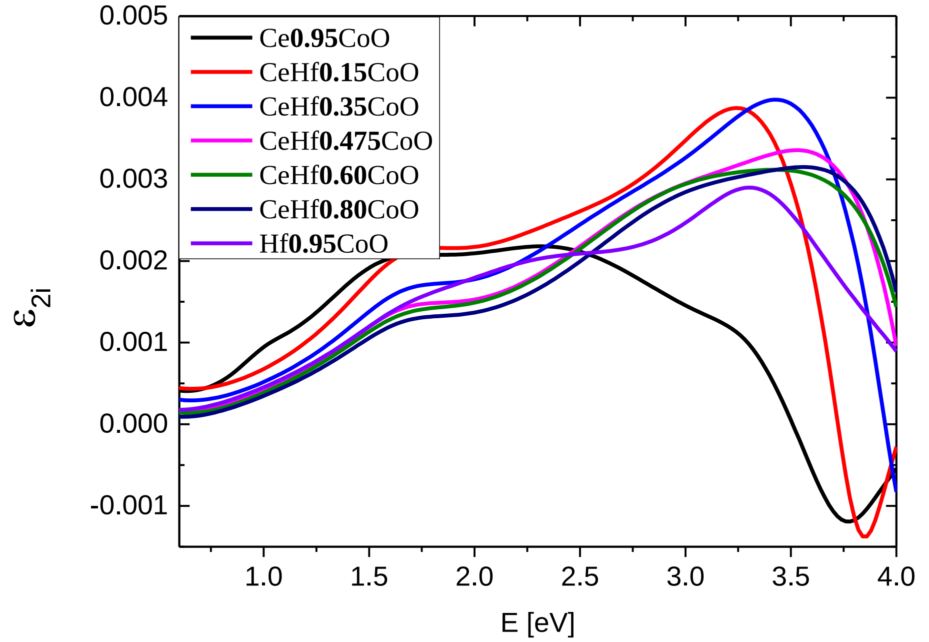

Figure 6.4.8: Imaginary parts of the off-diagonal permittivity tensor elements ε_{2i} of CeHfCoO films.

In order to relate calculated spectra to the microscopic theory, we parameterize them by the sum of Para and Dia oscillator terms. We listed some of used parameters in table 6.4.4. From the result, one can clearly see that the main MO contribution comes from Dia transitions 1 (1.5-1.65 eV), 2 (2.42-2.95 eV) and 4 (3.75-4.3 eV). These therefore correspond to excited state split by the combined effect of exchange field and spin-orbit coupling. Moreover, they are all decreasing their values with increased Hf content. Transition 1 refers to localized 4f states in the band gap while transition 4 to the oxygen electronic transitions [97].

Table 6.4.4: Fitted parameters of Para and Dia transitions used to parameterize off-diagonal elements of the permittivity tensors of HfCoCoO films in the spectral range from 1.5 to 5.5 eV. Here, E_0 stands for central energy of the function; Amp represents amplitude of the function and Γ_0 is half-width in a half-height of the transition.

	Dia tr 1			Dia tr 2			Dia tr 3		
	E_0 (eV)	Amp	Γ_0 (eV)	E_0 (eV)	Amp	Γ_0 (eV)	E_0 (eV)	Amp	Br (eV)
Ce0.95Co	1.53	0.0014	0.5	2.42	0.0022	0.9	3.3	0.0005	0.3
CeHf0.15Co	1.65	0.0011	0.4	2.4	0.0014	0.8	3.35	0.0038	0.6
CeHf0.35Co	1.65	0.0008	0.4	2.65	0.0015	0.8	3.55	0.0038	0.7
CeHf0.475Co	1.65	0.0007	0.4	2.85	0.0018	0.8	3.75	0.003	0.7
CeHf0.60Co	1.65	0.0006	0.4	2.9	0.0017	0.8	3.82	0.0027	0.9
CeHf0.80Co	1.65	0.0006	0.4	2.95	0.0019	0.8	3.85	0.0027	0.7
Hf0.95Co	1.65	0.0004	0.4	2.3	0.0017	0.85	3.35	0.0023	0.5

	Dia tr 4			Dia tr 5			Para tr 1		
	E_0 (eV)	Amp	Γ_0 (eV)	E_0 (eV)	Amp	Γ_0 (eV)	E_0 (eV)	Amp	Γ_0 (eV)
Ce0.95Co	3.75	0.002	0.3	1	0.0003	0.2	0.35	0.0008	0.9
CeHf0.15Co	3.83	0.004	0.2	-	-	-	0.4	0.0004	0.7
CeHf0.35Co	4.05	0.004	0.2	-	-	-	0.35	0.0005	0.7
CeHf0.475Co	4.15	0.0035	0.2	-	-	-	0.3	0.0006	0.7
CeHf0.60Co	4.2	0.0033	0.2	-	-	-	0.3	0.0007	0.7
CeHf0.80Co	4.2	0.0032	0.2	-	-	-	0.27	0.0007	0.7
Hf0.95Co	4.3	0.001	0.2	-	-	-	0.27	0.0006	0.7

7. CONCLUSIONS

In this part of the thesis, we would like to conclude our findings for all investigated materials.

To conclude our results on CdZnTe, it is important to remind us that this material is a subject of interest for high-energy X-ray and gamma ray detectors. CdZnTe oxide layer and also surface roughness influence two important parameters for these types of detectors: photoconductivity and resistivity. We found in here, that smaller abrasive size results into thinner GdZnTe oxide layer and that this oxide layer completely diminishes after etching. When compared these findings to resistivity measurements, it was found that surface roughness decreases resistivity (damaged layer introducing conductive channels into the semi-insulating material), while oxide layer increases resistivity values. Maximum in resistivity was therefore found for sample polished by Al_2O_3 with the grain size of 0.3μm which showed both, small oxide layer as well as roughness. Photoconductivity was negatively influenced for both: increases oxide layer and roughness. When looking at the optical properties of material, we derived full permittivity tensor spectra of CdZnTe. We found that CdZnTe absorption increases with energy. We observed absorption edge close to 1.5 eV and three optical transitions at 3.3, 3.9 and 5.2 eV.

To conclude our results on $Gd_xFe_{(100-x)}$, it is important to note that perpendicular magnetic anisotropy is substantial for its application potential (MO-SLM, MO disk storage). This type of anisotropy is characteristic for concentrations close to $x \approx 25$, compensation concentration. We derived permittivity tensors for $Gd_xFe_{(100-x)}$ compositions close to this concentration. Our investigation of optical properties showed that $Gd_xFe_{(100-x)}$ absorption generally increases with energy in the measured spectral range from 1.5 to 5.5 eV. When investigating the effect of Gd substitution, we found that higher Gd content decreases both, ε_{1r} and ε_{1i} amplitudes and therefore the refraction index in the measured spectral range. Moreover, we found that Gd substitution increases absorption coefficient of this material bellow 5 eV, however it has the opposite effect above. Our investigation of magneto-optical properties of $Gd_xFe_{(100-x)}$ showed that Gd substitution decreases both, ε_{2r} and ε_{2i} amplitudes. We attributed this to the fact that the magnetic moment of Fe is in this ferrimagnetic alloy stronger than the magnetic moment of Gd. Perpendicular anisotropy of $Gd_xFe_{(100-x)}$ was confirmed for all the samples. Moreover, we observed change in the magnetization direction to the opposite site when reaching the compensation concentration. We used one Dia transition to parameterize spectra of the off-diagonal elements of the $Gd_xFe_{(100-x)}$ permittivity tensor in terms of microscopic theory. We assumed that the MO effect comes from different probabilities of transition between an orbital singlet ground state and split excited state and that Gd concentration decreases this splitting.

When investigating magnetic garnets, we started with Bix:YIGs thin films with various Bi concentrations and determined their full permittivity tensors at energies from 1.5 to 5 eV. TEM measurement confirmed that Bix:YIGs films grow uniformly and epitaxially on GGG. We found that bismuth substitution increases amplitudes of ε_{1r} and ε_{1i} in the measured spectral range. We observed optical transitions at 2.5, 3.2 and 4.4 eV and the absorption edge near 2.1 eV. As expected, we found that bismuth substitution leads to the enhancement in MOKE and Faraday effects which is crucial for garnet application potential. This result is also connected to the fact that bismuth increases ε_{2r} and ε_{2i} amplitudes at their extremes significantly. We used two Para transitions and three Dia transition to parameterize ε_{2r} and ε_{2i}.in terms of microscopic theory. We found that Bi substitution increases amplitudes almost of all transitions. It however lowers energy of Dia transition at 4.65 eV which most likely exist due to charge transfers from oxygen to octahedral Fe. We associated strongest Dia transitions at 2.5 eV and 3.3 eV with transitions t2(Fe3+) → t2g(Fe2+) and eg(Fe3+) → e(Fe2+). These are mainly responsible for the increase in MO effects. We attributed positive impact of Bi on these transitions to the increase in super-exchange interaction caused by the enhancement of electronic exchange.

As a second part of magnetic garnet research, we determined complete permittivity tensors of Bi1:NIGxGs and Bi2.5:NIGxGs thin films with different Ga concentrations at energies from 1.5 to 5.5 eV. We found that Ga substitution decreases amplitudes of ε_{1r} for Bi1:NIGxGs bellow 4 eV and increasing them above. On the other hand, Ga substitution does not noticeably influence amplitudes of ε_{1r} for Bi2.5:NIGxGs. We also found that Ga substitution increases therefore absorption of Bi1:NIGxGs in measured spectral range. However it decreases absorption for

Bi2.5:NIGxGs. Furthermore, the absorption of Bi2.5:NIGxGs is almost 30% stronger than absorption of Bi1:NIGxGs. We attribute this to the higher Bi concentration. When looking at MO properties, we found that Bi substitution increases and Ga substitution decreases amplitudes of MO effects. This is connected to ε_{2r} and ε_{2i} amplitudes which are increased by Bi and decreased by Ga substitution. To explain the effect of Ga properly we parameterized ε_{2r} and ε_{2i} spectra in terms of microscopic theory. We used four Para transitions to represent crystal field transitions. We also used four Dia transitions. The main contribution comes from Dia transitions associated with transitions t2(Fe3+) → t2g(Fe2+) and eg(Fe3+) → e(Fe2+), mainly responsible for the remarkable increase in MO effects. We found that Ga substitution is decreasing these transitions. This is in accordance with the assumption, that Ga is mostly substituted for Fe3+ tetrahedral, which is crucial for both transitions. We also found that Ga substitution lowers energy of much smaller Dia transition at 4.65 eV which most likely exist due to charge transfers from oxygen to octahedral Fe. This is in accordance with the assumption that Ga is in a smaller percentage also substituted per Fe3+ octahedral.

Finally, we focused on the determination of full dielectric permittivity tensors of CeHfCoO thin films with different Hf concentrations in the spectral range from 1.5 to 5.5 eV. We found that Hf content decreases ε_{1r} amplitudes in the whole measured spectral range. We also observed optical bandgap energies to be shifted from 3.21 to 4.1 eV when Hf content increased. We related these energies to O2p -> Ce4f electronic transitions. Similarly, we found that Hf doping decreases absorption in the whole measured spectral range. From this result we assumed that when is Hf replacing Ce in the material; it actually acts against optical vacancies from isolated Ce4f states localized within the optical bandgap, responsible for enhanced optical absorption. Absorption tail bellow 3.2 eV supported this theory and it was attributed to the effect of midgap defects. When investigating MO properties, we found that Faraday rotation extreme is shifting from 2.9 eV to higher energies. Rotation values decreased when Hf content increased. On the other hand, ellipticity values acted in the opposite manner. We also found that Hf substitution decreases both, ε_{2i} and ε_{2r} amplitudes and it is shifting their maxima to higher energies in the measure spectral range. This was explained by magnetoelastic effects which originate from distortions caused by in-plane compressive strain and vary with Ce-Co content. Hf substitution influences this content and reduces oxygen vacancies important for CeHfCoO magnetism. We parameterized ε_{2r} and ε_{2i} spectra in terms of microscopic theory by the sum of Para and Dia oscillator terms. We found that the main MO contribution comes from Dia transitions at (1.5-1.65 eV) which refers to localized 4f states in the band gap and at (3.75-4.3 eV) which refers to the oxygen electronic transitions.

List of Abbreviations

MO - Magneto-optical

SE - Spectroscopic Ellipsometry

MOKE - Magneto-optical Kerr Effect

EMA - Effective Medium Approximation method

MSA – Multi Sample Analysis

MOD - Metal Organic Decomposition

MO-SLM – Magneto-optical Spatial Light Modulator

GGG – Gadolinium Gallium Garnet, $Gd_3Ga_5O_{12}$

Bix:YIGs – Bismuth substituted Yttrium Iron Garnets, $Y_{3-x}Bi_xFe_5O_{12}$

Bi1:NIGxGs – Bismuth (1) and Gallium (x) substituted Neodymium Iron Garnets, $Nd_2BiFe_{(5-x)}Ga_xO_{12}$.

Bi2.5:NIGxGs - Bismuth (2.5) and Gallium (x) substituted Neodymium Iron Garnets, $Nd_{0.5}Bi_{2.5}Fe_{(5-x)}Ga_xO_{12}$

CeHfCoO – Hafnium and Cobalt substituted Cerium Oxide, $Ce_{(0.95-x)}Hf_xCo_{0.05}O_{(2-\delta)}$

Bibliography

1. F. Wooten, Optical Properties of Solids (Academinc Press, INC., 1972).

2. I. J.A. Woollam Co., CompleteEASE Data Analysis Manual (J.A. Woollam Co., Inc., 2011).

3. D. D. S. Meneses, M. Malki and P. Echegut, "Structure and lattice dynamics of binary lead silicate glasses investigated by infrared spectroscopy," J. Non-Cryst. Solids **352**(8), 769–776 (2006).

4. G. E. J. Jr. and F. A. Modine, "Parameterization of the optical functions of amorphous materials in the interband

5. region," Appl. Phys. Lett. **69**(3), 371-373 (1996).

6. T. E. Tiwald, D. W. Thompson, J. A. Woollam, W. Paulson and R. Hance, "Application of IR variable angle spectroscopic ellipsometry to the determination of free carrier concentration depth profiles," Thin Solid Films **313-314**(1-2), 661-666 (1998).

7. B. Johs, C. M. Herzinger, J. H. Dinan, A. Cornfeld and J. D. Benson, "Development of a parametric optical constant model for $Hg_{1-x}Cd_xTe$ for control of composition by spectroscopic ellipsometry during MBE growth," Thin Solid Films **313-314**(1-2), 137-142 (1998).

8. F. J. Kahn, P. S. Pershan and J. P. Remeika, "Ultraviolet Magneto-Optical Properties of Single-Crystal Orthoferrites, Garnets, and Other Ferric Oxide Compounds," Phys. Rev. **186**(3), 891-918 (1969).

9. S. Wittekoek, T. J. A. Poprna, J. M. Robertson and P. F. Bongers, "Magneto-optic spectra and the dielectric tensor elements of bismuth-substituted iron garnets at photon energies between 2.2—5.2 eV," Phys. Rev. B **12**(7), 2777-2788 (1975).

10. Š. Višňovský, Optics in Magnetic Multilayers and Nanostructures (Taylor & Francis, 2006).

11. G. Fowles, Introduction to Modern Optics (Dover publications, INC., 1989).

12. I. J.A. Woollam Co., Guide to using WVASE 2012).

13. P. Yeh, "Optics Of Anisotropic Layered Media: A New 4 X 4 Matrix Algebra," Surf. Sci. **96**(1-3), 41-53 (1979).

14. Š. Višňovský, "Magneto-Optical Effects In Crystals At The Normal Incidence," Czech. J. Ph. **37**(2), 218-231 (1987).

15. D. Schmidt and M. Schubert, "Anisotropic Bruggeman Effective Medium Approaches for Slanted Columnar Thin Films," J. Appl. Phys. **114**(8), 083510 (083511) (2013).

16. M. Nyvlt, Optical interactions in ultrathin magnetic film structures, Doctoral thesis, Charles University, (1996).

17. W. T. Ltd, Vertical Gradient Freeze, http://www.wafertech.co.uk/growth.htm, (2016).

18. C.-I. U. O. S. Trento, RF-Sputtering principles, http://www.tn.ifn.cnr.it/facilities/rf-sputtering-facility/rf-sputtering-principles, (2016).

19. T. Ishibashi, A. Mizusawa, M. Nagai, S. Shimizu, K. Sato, N. Togashi, T. Mogi, M. Houchido, H. Sano and K. Kuriyama, "Characterization of epitaxial $(Y,Bi)_3(Fe,Ga)_5O_{12}$ thin films grown by metalorganic decomposition method," J. Appl. Phys. **97**(1), 013516 (013514) (2005).

20. T. Ishibashi, K. Kawata, T. H. Johansen, J. He, N. Harada and K. Sato, "Magneto-optical Indicator Garnet Fimls Grown by Metal-organic Decomposition Method," J. Phys. Soc. Jpn. **32**(2-2), 150-153 (2008).

21. W. L. Prellier, P.; Mercey, B., "Colossal-magnetoresistive manganite thin film," Journal of Physics: Condensed Matter **13**(R915-R944 (2001).

22. O. I. ANDOR, Pulsed Laser Deposition, http://www.andor.com/learning-academy/pulsed-laser-deposition-an-introduction-to-pulsed-laser-deposition, (2017).

23. A. Hossain, A. E. Bolotnikov, G. S. Camarda, Y. Cui, S. Babalola, A. Burger and R. B. James, "Effects of Surface Processing on the Response of CZT Gamma Detectors: Studies with a Collimated Synchrotron X-Ray Beam," Journal of Electronic Materials **37**(9), 1356-1361 (2008).

24. J. Zázvorka, J. Franc, P. Moravec, E. Jesenská, L. Šedivý, J. Ulrych and K. Mašek, "Contactless resistivity and photoconductivity correlation to surface preparation of CdZnTe," Applied Surface Science **315**(144-148 (2014).

25. V. G. Ivanits'ka, P. Moravec, J. Franc, Z. F. Tomashik, P. I. Feychuk, V. M. Tomashik, L. P. Shcherbak, K. Mašek and P. Höschl, "Chemical Etching of CdTe in Aqueous Solutions of H2O2-HI-Citric Acid," Journal of Electronic Materials **36**(8), 1021-1024 (2007).

26. S. Tari, F. Aqariden, Y. Chang, C. Grein, J. Li and N. Kioussis, "Impact of Surface Treatment on the Structural and Electronic Properties of Polished CdZnTe Surfaces for Radiation Detectors," Journal of Electronic Materials **42**(11), 3252-3258 (2013).

27. S. Lalitha, S. Z. Karazhanov, P. Ravindran, S. Senthilarasu, R. Sathyamoorthy and J. Janabergenov, "Electronic structure, structural and optical properties of thermally evaporated CdTe thin films," Physica B: Condensed Matter **387**(1–2), 227-238 (2007).

28. B. R. Kumar, B. Hymavathi and T. S. Rao, "Studies on optoelectronic properties of DC reactive magnetron sputtered CdTe thin films," AIP Conference Proceedings **1576**(1), 73-75 (2014).

29. S. Adachi, T. Kimura and N. Suzuki, "Optical properties of CdTe: Experiment and modeling," J. Appl. Phys. **74**(5), 3435-3441 (1993).

30. P. Johansson, S. I. Khartsev and A. M. Grishin, "Comparison of Bi3Fe5O12 film giant Faraday rotators grown on (111) and (001) Gd3Ga5O12 single crystals," Thin Solid Films **515**(2), 477-480 (2006).

31. S. Leitenmeier, T. Korner, J. Griesbauer, M. Herbort, A. Heinrich and B. Stritzker, "Studies on the growth of epitaxial bismuth-substituted iron garneton gadolinium gallium garnet single crystals by pulsed laser deposition," J. Cryst. Growth **310**(24), 5392-5401 (2008).

32. N. Imamura and C. Ota, "Experimental Study on Magneto-Optical Disk Exerciser with the Laser Diode and Amorphous Magnetic Thin Films," Jpn. J. Appl. Phys. **19**(12), L731-L734 (1980).

33. K. Aoshima, K. Machida, D. Kato, T. Mishina, K. Wada, Y.-f. Cai, H. Kinjo, K. Kuga, H. Kikuchi, T. Ishibashi and N. Shimidzu, "A Magneto-Optical Spatial Light Modulator Driven by Spin Transfer Switching for 3D Holography Applications," J. Disp. Technol. **11**(2), 129-135 (2015).

34. S. Mangin, G. Marchal, C. Bellouard, W. Wernsdorfer and B. Barbara, "Magnetic behavior and resistivity of the domain-wall junction GdFe(1000 Å)/TbFe/GdFe(500 Å)…," Phys. Rev. B **58**(5), 2748-2757 (1998).

35. N. Nishimura, T. Hirai, A. Koganei, T. Ikeda, K. Okano, Y. Sekiguchi and Y. Osada, "Magnetic tunnel junction device with perpendicular magnetization films for high-density magnetic random access memory," J. Appl. Phys. **91**(8), 5246 (2002).

36. M. Urner-Wille and K. Witter, "Compensation point switching in homogeneous amorphous GdFe-films," J. Magn. Magn. Mater. **13**(1-2), 77-80 (1979).

37. Z. Shen, J. Li, S. Wang, S. Zhou and L. Chen, "Magneto-optical and optical properties of GdFe films," *in Proceedings of Fifth International Symposium on Optical Storage*, (SPIE, 2000), pp. 76-79.

38. S. Sugano and N. Kojima, Magneto-Optics (Springer, 2011).

39. I. Radu, K. Vahaplar, C. Stamm, T. Kachel, N. Pontius, H. A. Durr, T. A. Ostler, J. Barker, R. F. Evans, R. W. Chantrell, A. Tsukamoto, A. Itoh, A. Kirilyuk, T. Rasing and A. V. Kimel, "Transient ferromagnetic-like state mediating ultrafast reversal of antiferromagnetically coupled spins," Nature **472**(7342), 205-208 (2011).

40. T. A. Ostler, J. Barker, R. F. Evans, R. W. Chantrell, U. Atxitia, O. Chubykalo-Fesenko, S. El Moussaoui, L. Le Guyader, E. Mengotti, L. J. Heyderman, F. Nolting, A. Tsukamoto, A. Itoh, D. Afanasiev, B. A. Ivanov, A. M. Kalashnikova, K. Vahaplar, J. Mentink, A. Kirilyuk, T. Rasing and A. V. Kimel, "Ultrafast heating as a sufficient stimulus for magnetization reversal in a ferrimagnet," Nat. Commun. **3**(666), 1-6 (2012).

41. L. L. Guyader, S. E. Moussaoui, M. Buzzi, R. V. Chopdekar and L. J. Heyderman, "Demonstration of laser induced magnetization reversal in GdFeCo nanostructures," Appl. Phys. Lett. **101**(2), 022410(022414) (2012).

42. K. Vahaplar, A. M. Kalashnikova, A. V. Kimel, D. Hinzke, U. Nowak, R. Chantrell, A. Tsukamoto, A. Itoh, A. Kirilyuk and T. Rasing, "Ultrafast Path for Optical Magnetization Reversal via a Strongly Nonequilibrium State," Phys. Rev. Lett. **103**(11), 117201(117204) (2009).

43. A. R. Khorsand, M. Savoini, A. Kirilyuk, A. V. Kimel, A. Tsukamoto, A. Itoh and T. Rasing, "Role of Magnetic Circular Dichroism in All-Optical Magnetic Recording," Phys. Rev. Lett. **108**(12), 127205(127205) (2012).

44. K. Nishibayashi, K. Kuga and H. Munekata, "Laser-induced precession of magnetization in ferrimagnetic GdFe thin films with low power excitation," AIP Adv. **3**(3), 032107(032107) (2013).

45. A. Tsukamoto, T. Sato, S. Toriumi and A. Itoh, "Precessional switching by ultrashort pulse laser: Beyond room temperature ferromagnetic resonance limit," J. Appl. Phys. **109**(7), 07D302(303) (2011).

46. K. Aoshima, Y. Hashimoto, N. Funabashi, K. Machida, K. Kuga, H. Kikuchi, N. Shimidzu and T. Ishibashi, "Spin transfer switching of current-perpendicular-to-plane giant magnetoresistance with various Gd-Fe free-layer compositions," J. Appl. Phys. **111**(7), 07C911 (2012).

47. L. Boernstein, Magnetic Properties of Metals (Springer-Verlag, 1986).

48. H. Kinjo, K. Machida, K. Matsui, K.-i. Aoshima, D. Kato, K. Kuga, H. Kikuchi and N. Shimidzu, "Low-current-density spin-transfer switching in Gd22Fe78-MgO magnetic tunnel junction," J. Appl. Phys. **115**(20), 203903 (2014).

49. P. Terzieff and K. Lee, "Electron spectroscopy studies on amorphous GdFe and GdCo alloys," J. Appl. Phys. **50**(5), 3565-3569 (1979).

50. G. E. Henein and W. R. Wagner, "Stresses induced in GaAs by TiPt ohmic contacts," J. Appl. Phys. **54**(11), 6395-6400 (1983).

51. J. R. Greer, W. C. Oliver and W. D. Nix, "Size dependence of mechanical properties of gold at the micron scale in the absence of strain gradients," Acta Mater. **53**(6), 1821-1830 (2005).

52. W. D. Nix, "Mechanical Properties of Thin Films," Metall. Tran. A **20A**(11), 2217-2245 (1989).

53. A. Quemerais, B. Loisel, G. Jezequel, J. Thomas and J. C. Lemonnier, "Optical spectra of gadolinium and dysprosium: study of the 5p thresholds," J. Phys. F: Met. Phys. **11**(1), 293-303 (1981).

54. E. D. Palik, Handbook of Optical Constants of Solids (Accademic Press, 1991).

55. P. E. Ferguson and R. J. Romagnoli, "Transverse Kerr Magneto-Optic Effect and Optical Properties of Transition-Rare-Earth Alloys," J. Appl. Phys. **40**(3), 1236-1238 (1969).

56. C. D. Mee, "Recent measurements of the magneto-optical properties of some garnets," Contemporary Physics **8**(4), 385-400 (1967).

57. A. Kirihara, K.-I. Uchida, Y. Kajiwara, M. Ishida, Y. Nakamura, T. Manako, E. Saitoh and S. Yorozu, "Spin-current-driven thermoelectric coating," Nat. Mater. **11**(8), 686-689 (2012).

58. H. Nakayama, M. Althammer, Y.-T. Chen, K. Uchida, Y. Kajiwara, D. Kikuchi, T. Ohtani, S. Geprags, M. Opel, S. Takahashi, R. Gross, G. E. W. Bauer, S. T. B. Goennenwein and E. Saitoh, "Spin Hall Magnetoresistance Induced by a Nonequilibrium Proximity Effect," Phys. Rev. Lett. **110**(20), 206601(206605) (2013).

59. J.-P. Krumme, V. Doormann and P. Willich, "Bismuth iron garnet films prepared by rf magnetron sputtering," J. Appl. Phys. **57**(8), 3885-3887 (1985).

60. T. Okuda, N. Koshizuka, K. Hayashi, T. Takahashi, H. Kobani and H. Yamamoto, "Faraday Rotation In Highly Bi-Substituted Yttrium Iron Garnet Films Prepared By Ion Beam Sputtering," IEEE Trans. Magn. **23**(5), 3491-3493 (1987).

61. M. Okada, S. Katayama and K. Tominaga, "Preparation and magneto‐optic properties of Bi‐substituted yttrium iron garnet thin films by metalorganic chemical vapor deposition," J. Appl. Phys. **69**(6), 3566-3570 (1991).

62. H. Kidoh, A. Morimoto and T. Shimizu, "Synthesis of ferromagnetic Bi‐substituted yttrium iron garnet films by laser ablation," Appl. Phys. Lett. **59**(2), 237-239 (1991).

63. K. Matsumoto, S. Sasaki, Y. Asahara, K. Yamaguchi and T. Fujii, "Highly bismuth substituted yttrium iron garnet single crystal films prepared by sol-gel method," J. Magn. Magn. Mater. **104-107**(1), 451-152 (1992).

64. V. J. Fratello, S. J. Licht, C. D. Brandle, H. M. O'Bryan and F. A. Baiocchi, "Effect of bismuth doping on thermal expansion and misfit dislocations in epitaxial iron garnets," J. Cryst. Growth **142**(1-2), 93-102 (1994).

65. J.-L. Rehspringer, J. Bursik, D. Niznansky and A. Klarikova, "Characterisation of bismuth-doped yttrium iron garnet layers prepared by sol-gel process," J. Magn. Magn. Mater. **211**(1-3), 291-295 (2000).

66. J. L. Deschanvres and D. Cenda, "Deposition of Bi-substituted iron garnet magneto-optic thin films by MOCVD," J. Magn. Magn. Mater. **242-245**(2), 1172-1174 (2002).

67. P. Papakonstantinou, B. Teggart and R. Atkinson, "The effects of substrate temperature and oxygen pressure on pulsed laser deposited Bi-substituted Dy iron garnet films," J. Magn. Magn. Mater. **163**(3), 378-392 (1996).

68. N. Watanabe, N. Takahashi and K. Tsushima, "Non-equilibrium garnet films grown by pulsed laser deposition," Mater. Chem. Phys. **54**(1-3), 173-176 (1998).

69. S. Kahl and A. M. Grishin, "Evolution of properties of epitaxial bismuthiron garnet films with increasing thickness," J. Magn. Magn. Mater. **278**(1-2), 244-255 (2004).

70. A. Hasanpoura, M. Mozaffaria, J. Amighiana, H. Richertd, A. Lorenzd, M. Lindnerd, P. Gornertd and H. Heegn, "Preparation and magneto-optical properties of $BiY_2Fe_5O_{12}$ organic nanocomposite films," J. Magn. Magn. Mater. **317**(1-2), 41-45 (2007).

71. Q.-H. Yang, H.-W. Zhnag, Q.-Y. Wen, Y.-L. Liu, I. M. Syvorotka and I. I. Syvorotka, "Magneto-optical and Microwave Properties of LuBiIG Thin Films Prepared by Liquid Phase Epitaxy Method from Lead-Free Flux," Chin. Phys. Lett. **26**(4), 047401 (047404) (2009).

72. M. V. Indenbom, N. N. Kolesnikov, M. P. Kulakov, I. G. Naumenko, V. I. Nikitenko, A. A. Polyanskii, N. F. Vershinin and V. K. Vlasko-Vlasov, "Direct study of magnetic flux penetration and trapping in HTSC," Physica C: Superconductivity **166**(5), 486-496 (1990).

73. G. Satoshi, K. Naoki, Y. Masashi, M. Masato and T. Shoji, "Direct Observation of Flux Behavior in High- T c Oxide Superconductors Using The Faraday Effect of Iron Garnet Films," Jpn. J. Appl. Phys. **29**(7A), L1083 (1990).

74. P. Hansen and J.-P. Krumme, "Magnetic and magneto-optical properties of garnet films," Thin Solid Films **114**(1-2), 69-107 (1984).

75. T. Ishibashi, T. Kosaka, M. Naganuma and T. Nomura, "Magneto-optical properties of Bi-substituted yttrium iron garnet films by metal-organic decomposition method," *in Proceedings of International Conference on Magnetism (ICM 2009)*, (IOP Publishing, 2009), pp. 112002 (112004).

76. T. Ishibashi, G. Lou, A. Meguro, T. Hashinaka, M. Sasaki and T. Nishi, "Magneto-optical Imaging Plate Using Bismuth-Substituted Iron Garnet Film Prepared by Metal-Organic Decomposition," Sensors and Materials **27**(10), 965-970 (2015).

77. H. Lee, Y. Yoon, S. Kim, H. K. Yoo, H. Melikyan, E. Danielyan, A. Babajanyan, T. Ishibashi, B. Friedman and K. Lee, "Preparation of bismuth substituted yttrium iron garnet powder and thin film by the metal-organic decomposition method," J. Cryst. Growth **329**(1), 27-32 (2011).

78. S. Yao, T. Sato, K. Kaneko, S. Murai, K. Fujita and K. Tanaka, "Faraday effect of bismuth iron garnet thin film prepared by mist CVD method," Jpn. J. Appl. Phys. **54**(6), 063001 (2015).

79. M. Veis, E. Lišková, R. Antoš, Š. Višňovský, N. Kumar, D. S. Misra, N. Venkataramani, S. Prasad and R. Krishnan, "Polar and longitudinal magneto-optical spectroscopy of bismuth substituted yttrium iron garnet films grown by pulsed laser deposition," Thin Solid Films **519**(22), 8041-8046 (2011).

80. M. Deb, E. Popova, A. Fouchet and N. Keller, "Magneto-optical Faraday spectroscopy of completely bismuth-substituted $Bi_3Fe_5O_{12}$ garnet thin films," J. Phys. D: Appl. Phys. **45**(45), 455001 (455009) (2012).

81. E. Popova, N. Keller, F. Gendron, L. Thomas, M.-C. Brianso, M. Guyot, M. Tessier and S. S. P. Parkin, "Perpendicular magnetic anisotropy in ultrathin yttrium iron garnet films prepared by pulsed laser deposition technique," J. Vac. Sci. Technol. **19**(5), 2567-2570 (2001).

82. E. Popova, N. Keller, F. Jomard, L. Thomas, M.-C. Brianso, F. Gendron, M. Guyot and M. Tessier, "Exchange coupling in ultrathin epitaxial yttrium iron garnet films," EPJ B **31**(1), 69-74 (2003).

83. S. Zollner, A. A. Demkov, R. Liu, P. L. Fejes, R. B. Gregory, P. Alluri, J. A. Curless, Z. Yu, J. Ramdani, R. Droopad, T. E. Tiwald, J. N. Hilfiker and J. A. Woollam, "Optical properties of bulk and thin-film SrTiO3 on Si and Pt," Journal of Vacuum Science & Technology B **18**(4), 2242-2254 (2000).

84. V. Berzhansky, T. Mikhailova, A. Shaposhnikov, A. Prokopov, A. Karavainikov, V. Kotov, D. Balabanov and V. Burkov, "Magneto-optics of nanoscale Bi:YIG films," Appl. Opt. **52**(26), 6599-6606 (2013).

85. M. Niyaifar and H. Mohammadpour, "Study on magnetic role of Bi3+ ion by random cation distribution model in Bi–YIG system," J. Magn. Magn. Mater. **396**(65-70 (2015).

86. S. Wittekoek and D. E. Lacklison, "Investigation of the Origin of the Anomalous Faraday Rotation of $Bi_xCa_{3-x}Fe_{3.5+0.5x}V_{1.5-0.5x}O_{12}$ by Means of the Magneto-optical Kerr Effect," Phys. Rev. Lett. **28**(12), 740-743 (1972).

87. E. Jesenska, T. Yoshida, K. Shinozaki, T. Ishibashi, L. Beran, M. Zahradnik, R. Antos, M. Kučera and M. Veis, "Optical and magneto-optical properties of Bi substituted yttrium iron garnets prepared by metal organic decomposition," Opt. Mater. Express **6**(6), 1986-1997 (2016).

88. L. Bi, J. Hu, P. Jiang, D. H. Kim, G. F. Dionne, L. C. Kimerling and C. A. Ross, "On-chip optical isolation in monolithically integrated non-reciprocal optical resonators," Nat Photon **5**(12), 758-762 (2011).

89. M. Inoue, H. Uchida, K. Nishimura and P. B. Lim, "Magnetophotonic crystals-a novel magneto-optic material with artificial periodic structures," Journal of Materials Chemistry **16**(7), 678-684 (2006).

90. K. Iwasaki, H. Mochizuki, H. Umezawa and M. Inoue, "Practical Magneto-Optic Spatial Light Modulator With Single Magnetic Domain Pixels," IEEE Trans. Magn. **44**(11), 3296-3299 (2008).

91. M. Pohl, L. E. Kreilkamp, V. I. Belotelov, I. A. Akimov, A N. Kalish, N. E. Khokhlov, V. J. Yallapragada, A. V. Gopal, M. Nur-E-Alam, M. Vasiliev, D. R. Yakovlev, K. Alameh, A K. Zvezdin and M. Bayer, "Tuning of the transverse magneto-optical Kerr effect in magneto-plasmonic crystals," New Journal of Physics **15**(7), 075024 (2013).

92. A. Tiwari, V. M. Bhosle, S. Ramachandran, N. Sudhakar, J. Narayan, S. Budak and A. Gupta, "Ferromagnetism in Co doped CeO2: Observation of a giant magnetic moment with a high Curie temperature," Appl. Phys. Lett. **88**(14), 142511 (2006).

93. V. Fernandes, J. J. Klein, N. Mattoso, D. H. Mosca, E. Silveira, E. Ribeiro, W. H. Schreiner, J. Varalda and A. J. A. de Oliveira, "Room temperature ferromagnetism in Co-doped CeO2 films on Si(001)," Phys. Rev. B **75**(12), 121304 (2007).

94. B. Vodungbo, Y. Zheng, F. Vidal, D. Demaille, V. H. Etgens and D. H. Mosca, "Room temperature ferromagnetism of Co doped CeO2−δ diluted magnetic oxide: Effect of oxygen and anisotropy," Appl. Phys. Lett. **90**(6), 062510 (2007).

95. D. Barreca, G. Bruno, A. Gasparotto, M. Losurdo and E. Tondello, "Nanostructure and optical properties of CeO2 thin films obtained by plasma-enhanced chemical vapor deposition," Materials Science and Engineering: C **23**(6–8), 1013-1016 (2003).

96. C. Fu-Chien and L. Chih-Ming, "Optical and electrical characterizations of cerium oxide thin films," J. Phys. D: Appl. Phys. **43**(7), 075104 (2010).

97. M. Veis, M. Kucera, M. Zahradnik, R. Antos, J. Mistrik, L. Bi, H.-S. Kim, G. F. Dionne and C. A. Ross, "Optical and magneto-optical properties of Co-doped CeO2−δ films in the 0.5 to 4 eV range," J. Appl. Phys. **115**(17), 17A940 (2014).

98. C. W. M. Castleton, J. Kullgren and K. Hermansson, "Tuning LDA+U for electron localization and structure at oxygen vacancies in ceria," The Journal of Chemical Physics **127**(24), 244704 (2007).

99. F. Marabelli and P. Wachter, "Covalent insulator ${\mathrm{CeO}}_{2}$: Optical reflectivity measurements," Phys. Rev. B **36**(2), 1238-1243 (1987).

100. A. H. Morshed, M. E. Moussa, S. M. Bedair, R. Leonard, S. X. Liu and N. El-Masry, "Violet/blue emission from epitaxial cerium oxide films on silicon substrates," Appl. Phys. Lett. **70**(13), 1647-1649 (1997).

101. L. Bi, H.-S. Kim, G. F. Dionne, S. A. Speakman, D. Bono and C. A. Ross, "Structural, magnetic, and magneto-optical properties of Co-doped CeO2−δ films," J. Appl. Phys. **103**(7), 07D138 (2008).